Leveraging the Properties of Aprotic Solvents Towards Efficient Electrocatalytic Carbon Dioxide Reduction

by

An T. Chu

A.B. Chemistry
Princeton University, 2017

Submitted to the Department of Chemistry
in Partial Fulfillment of the Requirements for the Degree of

DOCTOR OF PHILOSOPHY IN CHEMISTRY

at the

MASSACHUSETTS INSTITUTE OF TECHNOLOGY

February 2024

Authored by: An T. Chu
Department of Chemistry
September 6th, 2023

Certified by: Yogesh Surendranath
Professor of Chemistry
Thesis Supervisor

Accepted by: Adam P. Willard
Professor of Chemistry
Graduate Officer

This doctoral thesis has been examined by a Committee of the Department of Chemistry as follows:

Professor Alison Wendlandt: _____
Chair, Thesis Committee

Professor Daniel L. M. Suess: _____
Member, Thesis Committee

Professor Yogesh Surendranath: _____
Thesis Supervisor

Leveraging the Properties of Aprotic Solvents Towards Efficient Electrocatalytic Carbon Dioxide Reduction

by

An T. Chu

Submitted to the Department of Chemistry on September 6th, 2023 in Partial Fulfillment of the Requirements of the Degree of Philosophy in Chemistry

ABSTRACT

Electrochemical carbon dioxide reduction has been studied as a method to sustainably produce valorized hydrocarbons. However, the reaction faces two challenges: low reaction selectivity towards value-added products, and the deleterious reaction of carbon dioxide with the electrolyte to form soluble carbonate species. While both issues are sensitive to the composition of the electrolyte, the reaction has been exhaustively studied in aqueous electrolytes with limited opportunities for further extensive tunability. This thesis describes approaches for overcoming low reaction selectivity and electrolyte carbonation using aprotic-solvent based electrolytes. We leverage the unique solvation environments and equilibrium acidities accessible in such media to overcome key limitations to reaction performance that are intrinsically linked to the use of aqueous electrolytes. We demonstrate key principles for tuning aprotic solvent-based electrolytes towards improving carbon dioxide electroreduction catalysis, establishing the foundation for the development of advanced electrolyte designs.

Chapter 1 details the development of a dimethyl sulfoxide / acetic acid electrolyte which can engender selective carbon dioxide reduction with minimal electrolyte carbonation on gold cathodes. We demonstrate that the key to engendering these balance of properties entails operating an electrolyte with a low water content, with simultaneous usage of a buffer which is non-nucleophilic and whose pK_a is matched to the carbon dioxide / bicarbonate equilibrium. Under such conditions, the selectivity to carbon monoxide can be driven as high as 90% with only millimolar equilibrium bicarbonate formation: a compromise difficult to achieve in water.

Chapter 2 details the discovery of a new mechanism for ethylene electrosynthesis on copper catalyst using dimethyl sulfoxide / phenol electrolyte. Starting from carbon monoxide—a crucial intermediate in the carbon dioxide reduction pathway—we present kinetic evidence that radically altering the solvent environment and proton donor can enable a mechanism involving quasi-equilibrium proton and electron transfer steps prior to a late rate-determining step. By demonstrating that the pathway in dimethyl sulfoxide / phenol has a potential-rate scaling and acid order distinct from those in aqueous electrolytes, we establish a new tunable platform for enabling selective electrocatalysis of hydrocarbon products.

Thesis supervisor: Yogesh Surendranath

Title: Professor of Chemistry

Table of Contents

Table of Figures

average and standard deviation of triplicate measurements; error bars not visible are smaller than the data points shown.

Figure S2.11. ^{1}H NMR spectra of ^{13}C labeled formate following electrolysis in $^{13}CO_2$ in DMSO/AcOH electrolyte. 52

Figure S2.12. (a) Potential-dependent current trends for CO, H_2, and the faradaic balance in DMSO/AcOH (blue) and DMSO/AcOH with 1 M added water ("wet DMSO/AcOH", orange) electrolyte versus the (a) cobaltocene/cobaltocenium (Cc/Cc^+) internal reference potential and (b) RHE (reversible hydrogen electrode) reference potential. Electrolysis was conducted via galvanostatic polarization from –0.17 to –2.03 mA cm^{-2} on pc-Au catalyst. The faradaic balance was calculated as the remaining partial current after accounting for all gaseous reaction products and ascribed to formate production. All current densities are normalized with respect to the electrochemically active surface area. The data points and error bars correspond to the average and standard deviation of triplicate measurements; error bars not visible are smaller than the data points shown. 53

Figure S2.13. Difference in the measured equilibrium potential of the H^+/H_2 redox couple in 0.1 M KOH (blue), 0.1 M $KHCO_3$ (light blue), DMSO/AcOH (purple) and wet DMSO/AcOH (light purple) electrolytes before and after exposure to 0.5 atm Ar and 0.5 atm CO_2. In both conditions, 0.5 atm H_2 was present to maintain Nernstian equilibrium. The data points and error bars correspond to the average and standard deviation of triplicate measurements. 53

Figure 3.1. (Top) A commonly invoked mechanism for ethylene formation from CO on polycrystalline Cu has been found to be insensitive to variation in pH, cation, or anion. (Bottom) We postulated that an aprotic solvent environment would expose new mechanistic landscapes for C_2 production formation. 58

Figure 3.2. (a) Potential-dependent faradaic efficiency trends for ethylene, hydrogen, and the faradaic balance in the DMSO/$TBAPF_6$ electrolyte collected under various analytical $PhOH/PhO^-$ buffer strengths ($C_{A,0}$) with a 4:1 analytical ratio of PhOH ($C_{HA,0}$) and TBAPhO ($C_{A-,0}$). Experiments were conducted via steady-state galvanostatic polarization from −0.26 to −2.6 mA cm^{-2} applied current on pc-Cu catalyst. The faradaic balance was taken to be the remaining current after accounting for the total balance of all gaseous reaction products. All potentials are referenced to the cobaltocenium ($CoCp_2$) redox couple. All current densities are normalized with respect to the electrochemically active surface area. The data points and error bars correspond to the average and standard deviations of at least two or more independent measurements. (b) Faradaic efficiency of all detected products following bulk electrolysis at −2.1 mA cm^{-2} (−1.02 V vs $CoCp_2$) in 1000 mM $C_{A,0}$ buffer. 61

Figure 3.3. Current density vs potential (Tafel) plots for ethylene formation as a function of the analytical $PhOH/PhO^-$ buffer strength ($C_{A,0}$) in the DMSO/$TBAPF_6$ electrolyte, with a 4:1 analytical ratio of PhOH ($C_{HA,0}$) to TBAPhO ($C_{A-,0}$). Experiments were conducted via steady-state galvanostatic polarization from −0.26 to −2.6 mA cm^{-2} applied current on pc-Cu catalyst. All potentials are referenced to the cobaltocenium ($CoCp_2$) redox couple. All current densities are normalized with respect to the electrochemically active surface area. The Tafel slope for each condition was calculated from a linear fit to the lowest five applied currents. The data points and error bars correspond to the average of at least two independent measurements. 63

Table of Tables

Chapter 1

Introduction

The vast majority of human life and living is sustained by the utilization of fossil fuels, which serves two major roles. The first is its use as a combustible source of thermal energy, while the second is its use as a feedstock for the industrial production of carbon and hydrogen containing chemicals and pharmaceuticals. However, a common byproduct of many of these net oxidative processes is CO_2, whose emission and accumulation in the atmosphere has been credited as an agent of climate change.[1] Hence, mitigating the deleterious effects of anthropogenic CO_2 emissions requires a coordinated effort to both extract CO_2 from the atmosphere and prevent further accumulation.[2] While innovative strategies are necessary to enable efficient capture and sequestration of atmospheric CO_2, releasing humanity's dependence on CO_2-emitting processes is equally challenging. This not only requires new processes for the synthesis of carbon-free or carbon-neutral fuels, but also an alternative source of carbon atoms to sustain the industrial production of commodity hydrocarbons and oxygenates. Hence, new strategies must be developed which can enable the efficient and sustainable interconversion of carbon-containing bonds.

For several decades, the electrochemical reduction of CO_2 (CO_2RR) has been studied as a lynchpin technology towards a societal transition away from fossil fuel-derived processes.[3,4] In this process, CO_2 is electrochemically reduced in the presence of a proton source to a wide array of hydrocarbons in an electrolytic cell. By utilizing CO_2 as a carbon synthon, the production of carbon chemicals and fuels can be met without using fossil fuels. In addition, CO_2RR can be driven by renewable energy sources such as solar and wind, whose issue of intermittent production is addressed by transducing the generated electrical energy into the stable and persistent chemical energy of hydrocarbon products.[5,6] In the limit that CO_2RR products are used as fuels and reoxidized into CO_2, renewably-driven CO_2RR can enable an anthropogenic carbon neutral use cycle. Hence, electrochemical CO_2RR stands as a complimentary method for releasing humanity's dependence on fossil fuels as an energy and carbon atom source.

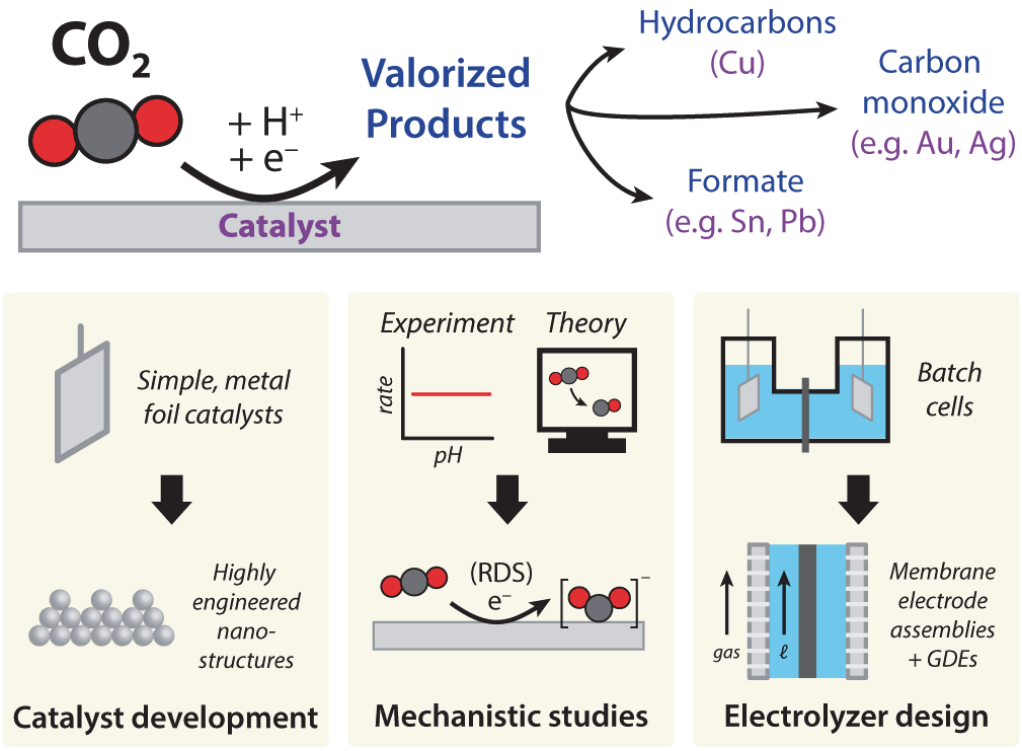

Figure 1.1. Schematic illustrating (top) CO_2 electrolysis to various catalyst-dependent product pathways and (bottom) broad areas of development in the field.

While many catalysts have been studied for this process, heterogeneous metal catalysts stand at the forefront due to their ability to generate value-added products with minimal need for additional catalyst-product separation steps. Starting from Yoshio Hori's seminal discovery of the reaction in the mid-1980's, a wide array of transition metal cathodes have been explored for their ability to reduce CO_2 (**Figure 1.1**).[7,8] Perhaps the most prodigious example (worthy of its own category) is Cu metal, which was discovered to catalyze the reduction of CO_2 and carbon monoxide (CORR) into a wide array of highly reduced products with immediate application in existing industrial processes such as ethylene, methane, and ethanol.[7,9] Another class of catalysts, which includes Au and Ag, was discovered to be highly selective for the production of carbon monoxide. Though less reduced than the aforementioned reaction products, carbon monoxide production is still valuable because it can be further reduced electrochemically with Cu or valorized with H_2 gas into higher order products using existing thermochemical methods (such as the Fischer-Tropsch reaction).[3,7,10] Finally, a third class of catalysts consisting primarily of post-transition metals such as Pb and Sn were found to be highly selective for formate production.[7,11–13]

In all categories of CO_2RR, numerous experimental and theoretical studies have been devoted towards advancing the understanding and optimization of the reaction manifold. For example, one prominent body of literature has focused on engineering the electrode material, varying the catalyst morphology to

understand its impact on reaction performance.[10,14–17] Another a body of literature has investigated the mechanism of CO_2 reduction using a combination of kinetic measurements, spectroscopic measurements and theoretical calculations.[18–24] These studies also encompass efforts to understand how the reaction varies with the electrolyte composition or modification of the interfacial reaction environment.[22,23,25–28] A third, more recent body of literature has developed advanced cell designs and electrode architectures to achieve record-breaking efficiencies, evolving out of divided batch reactors into flow cells and zero-gap electrolyzers.[29–37] Indeed, each broad area of literature has contributed valuable advances and insights to date. For example, mechanistic studies have elucidated that CO_2 (or CO in the case of Cu) reduction pathways on many metal catalysts is rate limited by single electron transfer, in alignment with the observation of the pH-independent $CO_{(2)}$RR rates of reduction.[23,38–41] Catalyst morphology studies have demonstrated that nanostructured, high surface area catalysts with porous structures tend to result in improved CO_2 selectivities and rates. Explanations for this behavior have been ascribed to the presence of a locally high pH during polarization, as well as an increase in favorable active sites and defects.[10,16,42–44] Attempts to design advanced electrode and cell architectures has resulted in the pioneering development of gas-diffusion electrodes, which were found to enable high-current density electrolysis (in the hundreds of mA/cm^2 or higher) by enabling efficient gas transport to the active site.[37,45,46] Other recent areas of development include the expansion of the library of known catalysts and reaction products via alloying strategies,[47–49] or the modification of electrodes with polymer materials to improve reaction selectivity.[50–52] These examples are by no means comprehensive of the entire field. Rather, they are mentioned here to demonstrate how the field has embraced studies elucidating the atomistic details of bond rearrangement, to developing innovative cell designs at larger scales, and everything in between.

Despite these enormous scientific efforts and advances, CO_2RR technologies are still in their primacy and suffer two significant limitations to their scalability. The first issue lies with the selectivity of the reaction. While Cu, for example, is capable of catalyzing CO_2 directly to value-added products, its selectivity for any single product is poor, motivating chemical insight into methods to drive the selective production of one- (C_1) or two-carbon (C_2) containing products.[4,53–55] In addition, the electrochemical reduction of protons to hydrogen gas (i.e. hydrogen evolution reaction, HER) is a competing parasitic side reaction observed under all CO_2RR catalysts, which lowers the electron efficiency of the process. The second issue lies with the chemical capture of CO_2 in commonly used electrolytes for this medium. For example, increasing the alkalinity of aqueous electrolytes has been widely observed to select for CO_2RR over HER by preferentially attenuating the rate of the latter. Alkaline electrolyte conditions have thus been used in some of the most efficient reported systems to date.[29,36] However, the spontaneous reaction of CO_2 with alkaline solutions forms soluble carbonates and bicarbonates, which lowers the electrolyte pH and thus the selectivity of the reaction. It also converts CO_2 near the interface into an inert anion, which migrates

from the cathode to the anode and is re-acidified to CO_2 due to the proton-releasing water oxidation half reaction. This undesirable process complicates electrolyzer design since an additional cost of separation is needed at the anode to purify CO_2 from O_2. Indeed, both what has been dubbed as "the carbonate problem" and the challenge to the reaction selectivity is an existential problem to nearly all CO_2RR electroreduction systems.[56,57] These limitations challenge further opportunities to deploy CO_2RR technologies, particularly those that utilize alkaline aqueous electrolyzer designs.

Fundamentally, the reaction selectivity and the carbonate problem are both inherently linked to the properties of electrolyte; the former is driven by the molecular interactions at the electrode-electrolyte interface, while the latter can be viewed as an electrolyte reaction. For nearly four decades, work in the field has overwhelmingly focused on studying the catalysis in aqueous electrolytes. In such studies, properties such as electrolyte acidity and supporting electrolyte identity have been exhaustively explored, but with limited impact on the aforementioned challenges. In contrast, only a smaller body of work has conducted the reaction in non-aqueous electroytes.[58] This is unusual because, in principle, non-aqueous electrolytes have a wide variety of chemical properties that could be leveraged to positively affect CO_2RR catalysis. For example, in an aprotic electrolyte, one can drive proton transfer selectively from an exogeneously added proton donor, whereas in an aqueous electrolyte, the proton transfer usually occurs from water or hydronium ions. This feature permits direct control of the thermodynamics and kinetics of proton transfer to key intermediates during catalysis, as well as control over the chemical speciation of soluble carbonate species towards CO_2 gas. In addition, aprotic solvent-based electrolytes have radically different solvation and dielectric properties,[59] which could affect solvent reorganization energies and the free energy of reaction intermediates. Finally, aprotic solvents can enable access to supporting electrolytes or additives which are not soluble in water, and in the limiting extreme, allow electrolysis to occur in the absence of water from the reaction system entirely. The potential benefits of operating in a non-aqueous solvent are not intended to mask the real and obvious drawbacks, such as their issues with cost, scalability, and conductivity. Indeed, I speculate that the lack of attention in this medium is because there are few reported discoveries—in any bottom-line metric—that suggested that they could be net advantageous over an already-existing aqueous-based electrolyte design.[58,60–65] However, I believed that there was an opportunity to demonstrate how non-aqueous electrolytes can be designed to target the issue of selectivity and electrolyte carbonation, especially because both issues are intimately related to the usage of water as an electrolyte, and are currently limiting the scale of such technologies in the field.

What follows in this thesis is my—and my colleagues'—efforts to overcome these central challenges in CO_2RR electroreduction catalysis with the rational design of aprotic-based electrolyte designs. A challenge of studying and developing non-aqueous systems lies with the number of potential variables to

tune, such as the proton donor, solvent, and supporting electrolyte. Rather than embarking on an effort to screen all permutations of testable parameters, this thesis describes studies which begin with an experimental hypothesis founded on a chemical hypothesis. The resulting electrolyte designs inspired by these principles will then be shown to expose fundamentally new reaction phenomenology, inspiring new opportunities for next-generation electrolyte design towards efficient CO_2RR platforms.

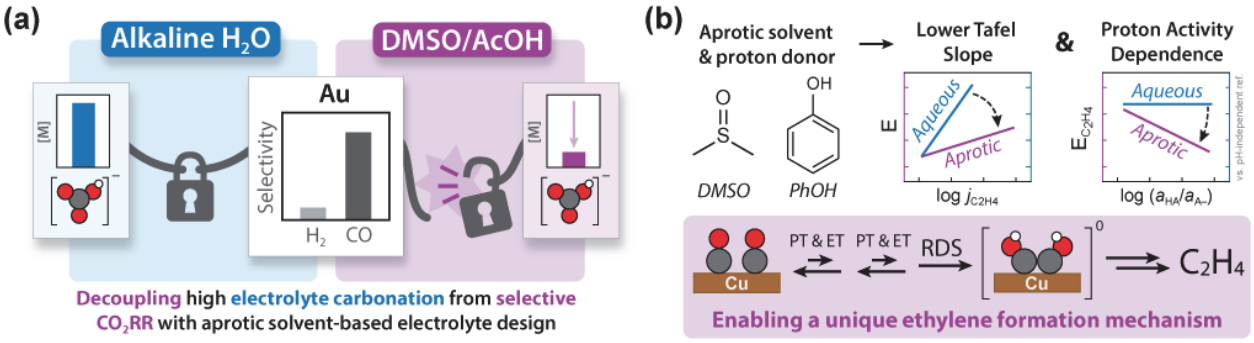

Figure 1.2. Overview of the principal advances presented in (a) chapter 1 and (b) chapter 2 of this thesis.

Chapter 1 details the discovery and development of a DMSO / acetic acid electrolyte to mitigate the carbonate problem, using selective CO_2 reduction to CO on Au based cathodes as a model platform (**Figure 1.2a**). This work was born out of a simple hypothesis that, if the carbonate problem exists because of the reaction with CO_2 with water, then one should not operate in water. While this is true in principle, developing an electrolyte which mitigates carbonation without compromising the reaction selectivity or overpotential is non-trivial, especially in aqueous electrolytes where it has not been demonstrated to date. In this chapter, I detail the polarization and NMR studies which lead to the development of a proof-of-concept electrolyte design that successfully mitigates carbonation while also engendering high reaction selectivity. By probing the proton activity of the medium, I demonstrate that the key to such behavior lies in the judicious choice of acetic acid as the proton donor. Specifically, in dimethyl sulfoxide (DMSO), acetic acid buffer has a non-nucleophilic conjugate base and has a pK_a closely matched to the CO_2/bicarbonate equilibrium: both properties enable low equilibrium electrolyte carbonation, even in solvents with relatively high water content.

Chapter 2 details the discovery of a DMSO / phenol electrolyte which demonstrates a completely new mechanism for the electrosynthesis of ethylene from CO on Cu (**Figure 1.2b**). In aqueous electrolytes, CO_2 or CO reduction on Cu leads to the formation of ethylene, which is one of the most valuable products of the reaction and a rare example of C-C coupling occurring on a room-temperature heterogeneous catalyst. Numerous mechanistic studies, focusing on CO reduction as it is a crucial intermediate in the pathway, have demonstrated that ethylene formation involves an early rate-determining electron transfer step regardless of the catalyst structure or electrolyte conditions. In recognizing that this consensus mechanism

constrains the design space in Cu-catalyzed CO_2RR, I show in this chapter how dramatically altering the proton transfer thermodynamics, kinetics, and interfacial solvation can lead to dramatically distinct reactivity. In addition to completely suppressing C_1 formation pathways, ethylene formation is observed to have a substantially distinct proton order and potential-rate (Tafel) scaling than the reaction in water. The electrokinetic studies evince a new mechanism involving a late rate-determining step preceded by multiple quasi-equilibrated proton and electron transfer steps, widening the known reactivity and tunability space for a decades-old catalyst.

1.1. References

(1) International Energy Agency. *World Energy Outlook 2021*; Paris, 2021.

(2) International Energy Agency. *Putting CO_2 to Use*; France, 2019.

(3) Stephens, I. E. L.; Chan, K.; Bagger, A.; Boettcher, S. W.; Bonin, J.; Boutin, E.; Buckley, A. K.; Buonsanti, R.; Cave, E. R.; Chang, X.; Chee, S. W.; da Silva, A. H. M.; de Luna, P.; Einsle, O.; Endrődi, B.; Escudero-Escribano, M.; Ferreira de Araujo, J. V; Figueiredo, M. C.; Hahn, C.; Hansen, K. U.; Haussener, S.; Hunegnaw, S.; Huo, Z.; Hwang, Y. J.; Janáky, C.; Jayathilake, B. S.; Jiao, F.; Jovanov, Z. P.; Karimi, P.; Koper, M. T. M.; Kuhl, K. P.; Lee, W. H.; Liang, Z.; Liu, X.; Ma, S.; Ma, M.; Oh, H.-S.; Robert, M.; Cuenya, B. R.; Rossmeisl, J.; Roy, C.; Ryan, M. P.; Sargent, E. H.; Sebastián-Pascual, P.; Seger, B.; Steier, L.; Strasser, P.; Varela, A. S.; Vos, R. E.; Wang, X.; Xu, B.; Yadegari, H.; Zhou, Y. 2022 Roadmap on Low Temperature Electrochemical CO_2 Reduction. *Journal of Physics: Energy* **2022**, *4* (4), 042003.

(4) Nitopi, S.; Bertheussen, E.; Scott, S. B.; Liu, X.; Engstfeld, A. K.; Horch, S.; Seger, B.; Stephens, I. E. L.; Chan, K.; Hahn, C.; Nørskov, J. K.; Jaramillo, T. F.; Chorkendorff, I. Progress and Perspectives of Electrochemical CO_2 Reduction on Copper in Aqueous Electrolyte. *Chem Rev* **2019**, *119* (12), 7610–7672.

(5) Cook, T. R.; Dogutan, D. K.; Reece, S. Y.; Surendranath, Y.; Teets, T. S.; Nocera, D. G. Solar Energy Supply and Storage for the Legacy and Nonlegacy Worlds. *Chem Rev* **2010**, *110* (11), 6474–6502.

(6) Segev, G.; Kibsgaard, J.; Hahn, C.; Xu, Z. J.; Cheng, W.-H. (Sophia); Deutsch, T. G.; Xiang, C.; Zhang, J. Z.; Hammarström, L.; Nocera, D. G.; Weber, A. Z.; Agbo, P.; Hisatomi, T.; Osterloh, F. E.; Domen, K.; Abdi, F. F.; Haussener, S.; Miller, D. J.; Ardo, S.; McIntyre, P. C.; Hannappel, T.; Hu, S.; Atwater, H.; Gregoire, J. M.; Ertem, M. Z.; Sharp, I. D.; Choi, K.-S.; Lee, J. S.; Ishitani, O.; Ager, J. W.; Prabhakar, R. R.; Bell, A. T.; Boettcher, S. W.; Vincent, K.; Takanabe, K.; Artero, V.; Napier, R.; Cuenya, B. R.; Koper, M. T. M.; Van De Krol, R.; Houle, F. The 2022 Solar Fuels Roadmap. *J Phys D Appl Phys* **2022**, *55* (32), 323003.

(7) Hori, Y. Electrochemical CO_2 Reduction on Metal Electrodes. In *Modern Aspects of Electrochemistry*; Springer New York: New York, NY; pp 89–189.

(8) White, J. L.; Baruch, M. F.; Pander, J. E.; Hu, Y.; Fortmeyer, I. C.; Park, J. E.; Zhang, T.; Liao, K.; Gu, J.; Yan, Y.; Shaw, T. W.; Abelev, E.; Bocarsly, A. B. Light-Driven Heterogeneous Reduction of Carbon Dioxide: Photocatalysts and Photoelectrodes. *Chem Rev* **2015**, *115* (23), 12888–12935.

(9) De Luna, P.; Hahn, C.; Higgins, D.; Jaffer, S. A.; Jaramillo, T. F.; Sargent, E. H. What Would It Take for Renewably Powered Electrosynthesis to Displace Petrochemical Processes? *Science (1979)* **2019**, *364* (6438), eaav3506.

(10) Yoon, Y.; Hall, A. S.; Surendranath, Y. Tuning of Silver Catalyst Mesostructure Promotes Selective Carbon Dioxide Conversion into Fuels. *Angewandte Chemie International Edition* **2016**, *55* (49), 15282–15286.

(11) Al-Tamreh, S. A.; Ibrahim, M. H.; El-Naas, M. H.; Vaes, J.; Pant, D.; Benamor, A.; Amhamed, A. Electroreduction of Carbon Dioxide into Formate: A Comprehensive Review. *ChemElectroChem* **2021**, *8* (17), 3207–3220.

(12) Lee, C. H.; Kanan, M. W. Controlling H^+ vs CO_2 Reduction Selectivity on Pb Electrodes. *ACS Catal* **2015**, *5* (1), 465–469.

(13) Baruch, M. F.; Pander, J. E.; White, J. L.; Bocarsly, A. B. Mechanistic Insights into the Reduction of CO_2 on Tin Electrodes Using in Situ ATR-IR Spectroscopy. *ACS Catal* **2015**, *5* (5), 3148–3156.

(14) Li, C. W.; Ciston, J.; Kanan, M. W. Electroreduction of Carbon Monoxide to Liquid Fuel on Oxide-Derived Nanocrystalline Copper. *Nature* **2014**, *508* (7497), 504–507.

(15) Birdja, Y. Y.; Pérez-Gallent, E.; Figueiredo, M. C.; Göttle, A. J.; Calle-Vallejo, F.; Koper, M. T. M. Advances and Challenges in Understanding the Electrocatalytic Conversion of Carbon Dioxide to Fuels. *Nat Energy* **2019**, *4* (9), 732–745.

(16) Wang, L.; Nitopi, S.; Wong, A. B.; Snider, J. L.; Nielander, A. C.; Morales-Guio, C. G.; Orazov, M.; Higgins, D. C.; Hahn, C.; Jaramillo, T. F. Electrochemically Converting Carbon Monoxide to Liquid Fuels by Directing Selectivity with Electrode Surface Area. *Nat Catal* **2019**, *2* (8), 702–708.

(17) Wang, H.; Matios, E.; Wang, C.; Luo, J.; Lu, X.; Hu, X.; Li, W. Rapid and Scalable Synthesis of Cuprous Halide-Derived Copper Nano-Architectures for Selective Electrochemical Reduction of Carbon Dioxide. *Nano Lett* **2019**, *19* (6), 3925–3932.

(18) Montoya, J. H.; Shi, C.; Chan, K.; Nørskov, J. K. Theoretical Insights into a CO Dimerization Mechanism in CO_2 Electroreduction. *J Phys Chem Lett* **2015**, *6* (11), 2032–2037.

(19) Liu, X.; Xiao, J.; Peng, H.; Hong, X.; Chan, K.; Nørskov, J. K. Understanding Trends in Electrochemical Carbon Dioxide Reduction Rates. *Nat Commun* **2017**, *8* (1), 15438.

(20) Goodpaster, J. D.; Bell, A. T.; Head-Gordon, M. Identification of Possible Pathways for C–C Bond Formation during Electrochemical Reduction of CO_2 : New Theoretical Insights from an Improved Electrochemical Model. *J Phys Chem Lett* **2016**, *7* (8), 1471–1477.

(21) Zijlstra, B.; Zhang, X.; Liu, J.-X.; Filot, I. A. W.; Zhou, Z.; Sun, S.; Hensen, E. J. M. First-Principles Microkinetics Simulations of Electrochemical Reduction of CO_2 over Cu Catalysts. *Electrochim Acta* **2020**, *335*, 135665.

(22) Wuttig, A.; Yoon, Y.; Ryu, J.; Surendranath, Y. Bicarbonate Is Not a General Acid in Au-Catalyzed CO_2 Electroreduction. *J Am Chem Soc* **2017**, *139* (47), 17109–17113.

(23) Wuttig, A.; Yaguchi, M.; Motobayashi, K.; Osawa, M.; Surendranath, Y. Inhibited Proton Transfer Enhances Au-Catalyzed CO_2-to-Fuels Selectivity. *Proceedings of the National Academy of Sciences* **2016**, *113* (32), E4585–E4593.

(24) Ovalle, V. J.; Waegele, M. M. Influence of pH and Proton Donor/Acceptor Identity on Electrocatalysis in Aqueous Media. *The Journal of Physical Chemistry C* **2021**, *125* (34), 18567–18578.

(25) Gu, J.; Liu, S.; Ni, W.; Ren, W.; Haussener, S.; Hu, X. Modulating Electric Field Distribution by Alkali Cations for CO_2 Electroreduction in Strongly Acidic Medium. *Nat Catal* **2022**, *5* (4), 268–276.

(26) Bagger, A.; Arnarson, L.; Hansen, M. H.; Spohr, E.; Rossmeisl, J. Electrochemical CO Reduction: A Property of the Electrochemical Interface. *J Am Chem Soc* **2019**, *141* (4), 1506–1514.

(27) Monteiro, M. C. O.; Dattila, F.; López, N.; Koper, M. T. M. The Role of Cation Acidity on the Competition between Hydrogen Evolution and CO_2 Reduction on Gold Electrodes. *J Am Chem Soc* **2022**, *144* (4), 1589–1602.

(28) Marcandalli, G.; Goyal, A.; Koper, M. T. M. Electrolyte Effects on the Faradaic Efficiency of CO_2 Reduction to CO on a Gold Electrode. *ACS Catal* **2021**, *11* (9), 4936–4945.

(29) Dinh, C.-T.; García de Arquer, F. P.; Sinton, D.; Sargent, E. H. High Rate, Selective, and Stable Electroreduction of CO_2 to CO in Basic and Neutral Media. *ACS Energy Lett* **2018**, *3* (11), 2835–2840.

(30) Xu, Y.; Miao, R. K.; Edwards, J. P.; Liu, S.; O'Brien, C. P.; Gabardo, C. M.; Fan, M.; Huang, J. E.; Robb, A.; Sargent, E. H.; Sinton, D. A Microchanneled Solid Electrolyte for Carbon-Efficient CO_2 Electrolysis. *Joule* **2022**.

(31) O'Brien, C. P.; Miao, R. K.; Liu, S.; Xu, Y.; Lee, G.; Robb, A.; Huang, J. E.; Xie, K.; Bertens, K.; Gabardo, C. M.; Edwards, J. P.; Dinh, C.-T.; Sargent, E. H.; Sinton, D. Single Pass CO_2 Conversion Exceeding 85% in the Electrosynthesis of Multicarbon Products via Local CO_2 Regeneration. *ACS Energy Lett* **2021**, *6* (8), 2952–2959.

(32) Xie, K.; Miao, R. K.; Ozden, A.; Liu, S.; Chen, Z.; Dinh, C.-T.; Huang, J. E.; Xu, Q.; Gabardo, C. M.; Lee, G.; Edwards, J. P.; O'Brien, C. P.; Boettcher, S. W.; Sinton, D.; Sargent, E. H. Bipolar Membrane Electrolyzers Enable High Single-Pass CO_2 Electroreduction to Multicarbon Products. *Nat Commun* **2022**, *13* (1), 3609.

(33) Huang, J. E.; Li, F.; Ozden, A.; Sedighian Rasouli, A.; García de Arquer, F. P.; Liu, S.; Zhang, S.; Luo, M.; Wang, X.; Lum, Y.; Xu, Y.; Bertens, K.; Miao, R. K.; Dinh, C.-T.; Sinton, D.; Sargent, E. H. CO_2 Electrolysis to Multicarbon Products in Strong Acid. *Science (1979)* **2021**, *372* (6546), 1074–1078.

(34) Ozden, A.; Li, F.; García de Arquer, F. P.; Rosas-Hernández, A.; Thevenon, A.; Wang, Y.; Hung, S.-F.; Wang, X.; Chen, B.; Li, J.; Wicks, J.; Luo, M.; Wang, Z.; Agapie, T.; Peters, J. C.; Sargent, E. H.; Sinton, D. High-Rate and Efficient Ethylene Electrosynthesis Using a Catalyst/Promoter/Transport Layer. *ACS Energy Lett* **2020**, *5* (9), 2811–2818.

(35) Dinh, C.-T.; Burdyny, T.; Kibria, M. G.; Seifitokaldani, A.; Gabardo, C. M.; García de Arquer, F. P.; Kiani, A.; Edwards, J. P.; De Luna, P.; Bushuyev, O. S.; Zou, C.; Quintero-Bermudez, R.; Pang, Y.; Sinton, D.; Sargent, E. H. CO_2 Electroreduction to Ethylene via Hydroxide-Mediated Copper Catalysis at an Abrupt Interface. *Science (1979)* **2018**, *360* (6390), 783–787.

(36) García de Arquer, F. P.; Dinh, C.-T.; Ozden, A.; Wicks, J.; McCallum, C.; Kirmani, A. R.; Nam, D.-H.; Gabardo, C.; Seifitokaldani, A.; Wang, X.; Li, Y. C.; Li, F.; Edwards, J.; Richter, L. J.; Thorpe, S. J.; Sinton, D.; Sargent, E. H. CO_2 Electrolysis to Multicarbon Products at Activities Greater than 1 A Cm^{-2}. *Science (1979)* **2020**, *367* (6478), 661–666.

(37) Wakerley, D.; Lamaison, S.; Wicks, J.; Clemens, A.; Feaster, J.; Corral, D.; Jaffer, S. A.; Sarkar, A.; Fontecave, M.; Duoss, E. B.; Baker, S.; Sargent, E. H.; Jaramillo, T. F.; Hahn, C. Gas Diffusion Electrodes, Reactor Designs and Key Metrics of Low-Temperature CO_2 Electrolysers. *Nat Energy* **2022**, *7* (2), 130–143.

(38) Schreier, M.; Yoon, Y.; Jackson, M. N.; Surendranath, Y. Competition between H and CO for Active Sites Governs Copper-Mediated Electrosynthesis of Hydrocarbon Fuels. *Angewandte Chemie International Edition* **2018**, *57* (32), 10221–10225.

(39) Hori, Y.; Takahashi, R.; Yoshinami, Y.; Murata, A. Electrochemical Reduction of CO at a Copper Electrode. *J Phys Chem B* **1997**, *101* (36), 7075–7081.

(40) Deng, W.; Zhang, P.; Seger, B.; Gong, J. Unraveling the Rate-Limiting Step of Two-Electron Transfer Electrochemical Reduction of Carbon Dioxide. *Nat Commun* **2022**, *13* (1), 803.

(41) Li, J.; Chang, X.; Zhang, H.; Malkani, A. S.; Cheng, M.; Xu, B.; Lu, Q. Electrokinetic and in Situ Spectroscopic Investigations of CO Electrochemical Reduction on Copper. *Nat Commun* **2021**, *12* (1), 3264.

(42) Hall, A. S.; Yoon, Y.; Wuttig, A.; Surendranath, Y. Mesostructure-Induced Selectivity in CO_2 Reduction Catalysis. *J Am Chem Soc* **2015**, *137* (47), 14834–14837.

(43) Bohra, D.; Chaudhry, J. H.; Burdyny, T.; Pidko, E. A.; Smith, W. A. Modeling the Electrical Double Layer to Understand the Reaction Environment in a CO_2 Electrocatalytic System. *Energy Environ Sci* **2019**, *12* (11), 3380–3389.

(44) Mariano, R. G.; Kang, M.; Wahab, O. J.; McPherson, I. J.; Rabinowitz, J. A.; Unwin, P. R.; Kanan, M. W. Microstructural Origin of Locally Enhanced CO_2 Electroreduction Activity on Gold. *Nat Mater* **2021**, *20* (7), 1000–1006.

(45) Higgins, D.; Hahn, C.; Xiang, C.; Jaramillo, T. F.; Weber, A. Z. Gas-Diffusion Electrodes for Carbon Dioxide Reduction: A New Paradigm. *ACS Energy Lett* **2019**, *4* (1), 317–324.

(46) Kong, Y.; Liu, M.; Hu, H.; Hou, Y.; Vesztergom, S.; Gálvez-Vázquez, M. de J.; Zelocualtecatl Montiel, I.; Kolivoška, V.; Broekmann, P. Cracks as Efficient Tools to Mitigate Flooding in Gas Diffusion Electrodes Used for the Electrochemical Reduction of Carbon Dioxide. *Small Methods* **2022**, *6* (9).

(47) Cronin, S. P.; Dulovic, S.; Lawrence, J. A.; Filsinger, K. A.; Hernandez-Gonzalez, A. P.; Evans, R.; Stiles, J. W.; Morris, J.; Pelczer, I.; Bocarsly, A. B. Direct Synthesis of 1-Butanol with High Faradaic Efficiency from CO_2 Utilizing Cascade Catalysis at a Ni-Enhanced $(Cr_2O_3)_3Ga_2O_3$ Electrocatalyst. *J Am Chem Soc* **2023**, *145* (12), 6762–6772.

(48) Wang, Y.; Cao, L.; Libretto, N. J.; Li, X.; Li, C.; Wan, Y.; He, C.; Lee, J.; Gregg, J.; Zong, H.; Su, D.; Miller, J. T.; Mueller, T.; Wang, C. Ensemble Effect in Bimetallic Electrocatalysts for CO_2 Reduction. *J Am Chem Soc* **2019**, *141* (42), 16635–16642.

(49) Wang, X.; Ou, P.; Ozden, A.; Hung, S.-F.; Tam, J.; Gabardo, C. M.; Howe, J. Y.; Sisler, J.; Bertens, K.; García de Arquer, F. P.; Miao, R. K.; O'Brien, C. P.; Wang, Z.; Abed, J.; Rasouli, A. S.; Sun, M.; Ip, A. H.; Sinton, D.; Sargent, E. H. Efficient Electrosynthesis of N-Propanol from Carbon Monoxide Using a Ag–Ru–Cu Catalyst. *Nat Energy* **2022**, *7* (2), 170–176.

(50) Han, Z.; Kortlever, R.; Chen, H.-Y.; Peters, J. C.; Agapie, T. CO_2 Reduction Selective for $C_{\geq 2}$ Products on Polycrystalline Copper with N-Substituted Pyridinium Additives. *ACS Cent Sci* **2017**, *3* (8), 853–859.

(51) Thevenon, A.; Rosas-Hernández, A.; Fontani Herreros, A. M.; Agapie, T.; Peters, J. C. Dramatic HER Suppression on Ag Electrodes via Molecular Films for Highly Selective CO_2 to CO Reduction. *ACS Catal* **2021**, *11* (8), 4530–4537.

(52) Wagner, A.; Sahm, C. D.; Reisner, E. Towards Molecular Understanding of Local Chemical Environment Effects in Electro- and Photocatalytic CO_2 Reduction. *Nat Catal* **2020**, *3* (10), 775–786.

(53) Nie, X.; Esopi, M. R.; Janik, M. J.; Asthagiri, A. Selectivity of CO_2 Reduction on Copper Electrodes: The Role of the Kinetics of Elementary Steps. *Angewandte Chemie International Edition* **2013**, *52* (9), 2459–2462.

(54) Wang, L.; Nitopi, S. A.; Bertheussen, E.; Orazov, M.; Morales-Guio, C. G.; Liu, X.; Higgins, D. C.; Chan, K.; Nørskov, J. K.; Hahn, C.; Jaramillo, T. F. Electrochemical Carbon Monoxide Reduction on Polycrystalline Copper: Effects of Potential, Pressure, and pH on Selectivity toward Multicarbon and Oxygenated Products. *ACS Catal* **2018**, *8* (8), 7445–7454.

(55) Varela, A. S.; Kroschel, M.; Reier, T.; Strasser, P. Controlling the Selectivity of CO_2 Electroreduction on Copper: The Effect of the Electrolyte Concentration and the Importance of the Local pH. *Catal Today* **2016**, *260*, 8–13.

(56) Rabinowitz, J. A.; Kanan, M. W. The Future of Low-Temperature Carbon Dioxide Electrolysis Depends on Solving One Basic Problem. *Nat Commun* **2020**, *11* (1), 5231.

(57) Ma, M.; Clark, E. L.; Therkildsen, K. T.; Dalsgaard, S.; Chorkendorff, I.; Seger, B. Insights into the Carbon Balance for CO_2 Electroreduction on Cu Using Gas Diffusion Electrode Reactor Designs. *Energy Environ Sci* **2020**, *13* (3), 977–985.

(58) König, M.; Vaes, J.; Klemm, E.; Pant, D. Solvents and Supporting Electrolytes in the Electrocatalytic Reduction of CO_2. *iScience* **2019**, *19*, 135–160.

(59) Izutsu, K. *Electrochemistry in Nonaqueous Solutions*; Wiley, 2009.

(60) Joshi, P. B.; Karki, N.; Wilson, A. J. Electrocatalytic CO_2 Reduction in Acetonitrile Enhanced by the Local Environment and Mass Transport of H_2O. *ACS Energy Lett* **2022**, *7* (2), 602–609.

(61) Haynes, L. V; Sawyer, D. T. Electrochemistry of Carbon Dioxide in Dimethyl Sulfoxide at Gold and Mercury Electrodes. *Anal Chem* **1967**, *39* (3), 332–338.

(62) Ito, K.; Ikeda, S.; Yamauchi, N.; Iida, T.; Takagi, T. Electrochemical Reduction Products of Carbon Dioxide at Some Metallic Electrodes in Nonaqueous Electrolytes. *Bull Chem Soc Jpn* **1985**, *58* (10), 3027–3028.

(63) Shi, J.; Shen, F.; Shi, F.; Song, N.; Jia, Y.-J.; Hu, Y.-Q.; Li, Q.-Y.; Liu, J.; Chen, T.-Y.; Dai, Y.-N. Electrochemical Reduction of CO_2 into CO in Tetrabutylammonium Perchlorate/Propylene Carbonate: Water Effects and Mechanism. *Electrochim Acta* **2017**, *240*, 114–121.

(64) Figueiredo, M. C.; Ledezma-Yanez, I.; Koper, M. T. M. In Situ Spectroscopic Study of CO_2 Electroreduction at Copper Electrodes in Acetonitrile. *ACS Catal* **2016**, *6* (4), 2382–2392.

(65) Rashid, N.; Bhat, M. A.; Ingole, P. P. Dendritic Copper Microstructured Electrodeposits for Efficient and Selective Electrochemical Reduction of Carbon Dioxide into C_1 and C_2 Hydrocarbons. *Journal of CO2 Utilization* **2020**, *38*, 385–397.

Chapter 2

Organic Non-Nucleophilic Electrolyte Resists Carbonation during Selective CO_2 Electroreduction

Adapted and reprinted with permission from Chu, A. T.; Jung, O.; Toh, W.L.; Surendranath, Y. Organic Non-Nucleophilic Electrolyte Resists Carbonation During Selective CO_2 Electroreduction. *J. Am. Chem. Soc*. **2023**, *145* (17), 9617-9623.

The work described in this chapter contains contributions from other researchers: Dr. Onyu Jung performed initial experimentation, and Wei Lun Toh contributed electrode materials.

2.1. Introduction

Low-temperature electrochemical reduction of CO_2 (CO_2RR) is a burgeoning approach to producing value-added products from renewable energy inputs.[1,2] However, the selective production of desirable carbon products is challenged by the competing hydrogen evolution reaction (HER). Mechanistic studies of transition metal cathodes such as Cu, Ag, and Au have shown that the CO_2 activation step that initiates CO_2RR is largely insensitive to the proton donor environment, whereas the HER is highly sensitive to the proton donor and pH environment.[3–6] Consequently, it has been universally observed that highly alkaline electrolytes selectively suppress HER, leading to enhanced faradaic efficiency (FE) for CO_2RR. Indeed, the high faradaic efficiency of many reported cathodes, such as nanostructured catalysts or gas-diffusion electrodes,[7,8] has been attributed to their ability to engender a high interfacial pH during polarization.

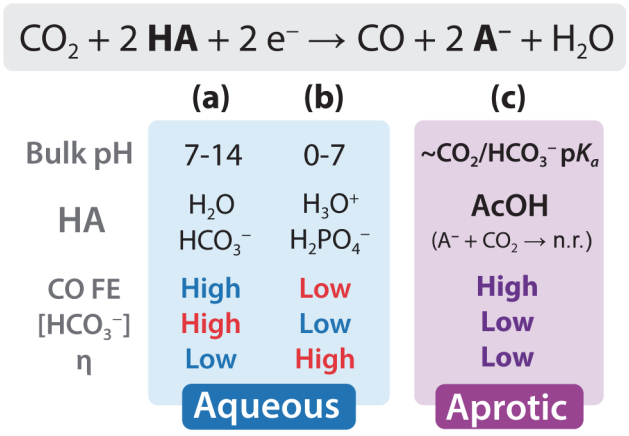

Figure 2.1. Schematic describing the reaction selectivity (CO FE), extent of carbonation ([HCO_3^-]), and overpotential (η) of CO_2RR-to-CO using proton donors (HA) of varying pK_a values and pH environments in (a, b) aqueous and (c) aprotic solvent-based electrolyte conditions.

While alkaline conditions foster high faradaic efficiency for CO_2RR, they compromise the carbon efficiency of CO_2 reduction. This impasse has been identified as "the carbonate problem" [9,10] and can be

understood by examining the role of the proton donor (HA) with reference to a prototypical reaction stoichiometry for CO_2RR to CO (**Figure 2.1**, top). In alkaline aqueous environments, water is the most competent proton donor (**Figure 2.1a**). Its deprotonation leads to the formation of two equivalents of hydroxide, which capture CO_2 by reacting to form (bi)carbonate anions. Since (bi)carbonates are inert to direct electroreduction,[11,12] their transport across the cell leads to their release at the anode, eroding the carbon efficiency of CO_2RR at the cathode. For CO_2 reduction to CO, this process leads to a 50% carbon utilization efficiency[9] and an even lower efficiency for more reduced products such as ethylene. At intermediate pH, bicarbonate itself can serve as the proton donor and form carbonate (**Figure 2.1a**). However, since CO_2 hydration generates carbonic acid, the electrogenerated carbonate dianion undergoes comproportionation to regenerate two equivalents of bicarbonate, reintroducing the carbonate problem. Indeed, the CO_2/HCO_3^- acid-base equilibrium makes electrolyte carbonation an inevitable consequence of operating at any pH above the CO_2/HCO_3^- buffer point (~pH 7).[13]

In contrast, high carbon efficiency can be recovered by operating in an acidic electrolyte with H_3O^+ as the terminal proton donor (**Figure 2.1b**). Since a high concentration of H_3O^+ at the interface would favor HER, various strategies have been explored to mitigate this effect. For example, acidic electrolytes are paired with ionomer coatings or high concentrations of alkali cations to foster a substantially high pH gradient at the interface.[14–17] Additionally, reverse-bias bipolar membrane strategies have been studied as a novel method for controlling the flux of H^+ delivered to the interface, which is proportional to the current applied.[18,19] These approaches share the common strategy of accepting the formation of (bi)carbonate at the interface and instead reprotonating it elsewhere in the cell to liberate CO_2. While these strategies have fostered higher carbon efficiencies, their operation leads to a significant interfacial pH differential relative to the bulk,[14] thus incurring large reduction overpotentials in excess of 0.8 V.[17] Furthermore, the faradaic efficiency of CO_2RR is partially compromised in some designs, relative to fully alkaline electrolytes.[19,20] To reduce these energetic losses while avoiding carbonation, a terminal proton donor with a pK_a close to that of CO_2/HCO_3^- would be ideal, but using phosphate buffers in neutral electrolytes has been shown to promote HER at the expense of CO_2RR FE. (**Figure 2.1b**).[12] As the foregoing discussion highlights, for aqueous CO_2RR, the proton-donating environment can either be optimized for high FE and low overpotential (alkaline) at the expense of high carbon efficiency, or optimized for high carbon efficiency (acidic) at the expense of high FE and low overpotential. While there is still opportunity for development with the aforementioned approaches, simultaneously achieving a high carbon efficiency, faradaic efficiency, and low overpotential faces inherent challenges in aqueous electrolytes, motivating the exploration of a completely orthogonal approach.

We hypothesized that the above impasse could be addressed in an aprotic solvent-based electrolyte, which possesses two key properties. First, the activity of water can be significantly lowered in an aprotic solvent, mitigating its intrinsic bias to react with CO_2 and its ability to kinetically promote PCET steps toward HER. Second, an exogenous proton donor can instead be chosen to support CO_2RR while inhibiting electrolyte carbonation. Indeed, CO_2RR has been demonstrated in aprotic solvent-based electrolytes: electrolysis using cathodes such as Cu or Au has been reported to support high selectivity for C_1 products.[21] However, such designs fail to address electrolyte carbonation because trace (or exogenously added) water is utilized as the proton donor,[22–25] leading to the expected stoichiometric formation of bicarbonate as a reaction product.[26] In contrast, we envisioned that carefully selecting an exogenous donor, with a pK_a closely matched to that of CO_2/HCO_3^- in an aprotic solvent, could mitigate carbonation while maintaining high CO_2RR faradaic efficiencies and modest overpotentials (**Figure 2.1**). In addition, the selected donor must form a conjugate base that is non-nucleophilic to avoid a reaction with CO_2 following PCET, eliminating a potential pathway for electrolyte-mediated CO_2 capture. While the use of aprotic solvents is non-trivial and its implementation into a device is uncertain, we sought to understand if these systems could, as a proof-of-concept, *decouple* selective CO_2RR from high electrolyte carbonation and overpotentials at the cathode: a formidable challenge facing all aqueous systems to date.

Herein, we report selective CO_2RR with minimal bulk carbonate formation in dimethyl sulfoxide (DMSO) electrolytes utilizing an acetic acid/acetate ($AcOH/AcO^-$) buffer as the proton-donating medium. We selected polycrystalline Au (pc-Au) as a model catalyst to characterize the H_2/C_1 selectivity in this previously unexplored electrolyte due to its simple CO_2RR product distribution consisting of H_2, CO, and formate.[13] We demonstrate that the electrolyte medium is capable of catalyzing CO_2RR to C_1 products with over 90% faradaic efficiency with minimal H_2 formation. NMR analysis demonstrates that only millimolar concentrations of bicarbonate are formed reversibly in the electrolyte. We also show that attenuated electrolyte carbonation and high C_1 reaction selectivity are maintained in electrolytes with 1 M of added water. Our results challenge the notion that carbonation is an inevitable outcome of CO_2RR and provide a conceptual framework for enabling low-carbonate CO_2RR electrolysis towards value-added products.

2.2. Au-Catalyzed CO_2 Reduction in DMSO/AcOH Buffer Selects for C_1 Products

To examine the H_2 versus C_1 product selectivity of CO_2RR, we polarized pc-Au electrodes under a CO_2 atmosphere in this previously unexplored electrolyte media. DMSO was selected for its electrochemical stability under highly reducing potentials. AcOH was selected because its carboxylate conjugate base is relatively non-nucleophilic and, as described later, possesses a similar pK_a to the CO_2/HCO_3^- equilibrium in DMSO. Galvanostatic electrolyses were conducted in electrolyte mixtures consisting of an analytical concentration of 0.3 M AcOH/tetrabutylammonium acetate (TBAAcO) in a 1:1 ratio with 0.15 M tetrabutylammonium hexafluorophosphate ($TBAPF_6$) supporting electrolyte, henceforth referred to as DMSO/AcOH. Gaseous products formed during polarization were characterized using in-line gas chromatography (see Section 2.6.2 for experimental details and **Figure S2.8** for representative gas chromatograms). Galvanostatic electrolyses were also conducted in DMSO/AcOH with 1 M of added water, henceforth referred to as "wet DMSO/AcOH". Both the potential-dependent faradaic efficiencies and reaction stability in this medium are discussed later (and in Section 2.7.1 for the latter). However, we stress that DMSO/AcOH was not rigorously dried and estimate an adventitious water concentration of 9 ± 2 mM (see Section 2.6.3 for details). In either condition, the applied potentials for steady-state electrolysis are far removed from the solvent reduction window of the respective electrolytes without AcOH/AcO^- and CO_2, confirming the reductive stability of DMSO (**Figure S2.9**). For the product selectivity studies reported in this section, a pc-Au counter electrode was utilized as the anode to avoid the possible effect of parasitic anode dissolution and contamination on the cathode reaction. However, we separately demonstrate that hydrogen oxidation can be sustained as an anode reaction using a Pt counter electrode to avoid the anodic decomposition of acetate to form carbon dioxide and ethane (i.e. Kolbe electrolysis), which has been previously reported to occur on Pt and Au anodes (see Section 2.7.2 for further discussion).[27]

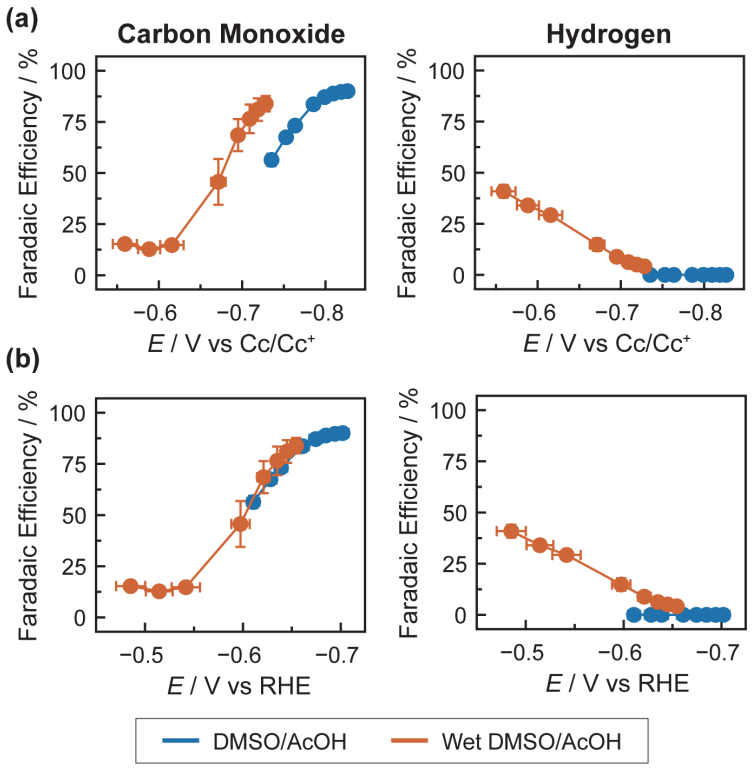

Figure 2.2. Potential-dependent faradaic efficiency trends for CO and H_2 in DMSO/AcOH (blue) and DMSO/AcOH with 1 M added water ("wet DMSO/AcOH", orange) electrolyte versus the (a) cobaltocene/cobaltocenium (Cc/Cc^+) internal reference potential and (b) RHE (reversible hydrogen electrode) reference potential. Electrolysis was conducted via galvanostatic polarization from −0.17 to −2.03 mA cm^{-2} on the pc-Au catalyst. All current densities are normalized with respect to the electrochemically active surface area. The data points and error bars correspond to the average and standard deviation of triplicate measurements; error bars not visible are smaller than the data points shown.

CO_2 electroreduction occurs with a high selectivity for C_1 products and minimal formation of H_2 in DMSO/AcOH. **Figure 2.2a** depicts the potential-dependent faradaic efficiency of H_2 and CO versus the cobaltocene/cobaltocenium (Cc/Cc^+) reference couple, while **Figure S2.10** depicts that of the faradaic balance in DMSO/AcOH (see **Figure S2.12** for partial current density trends per product). The selectivity for CO rises to a maximal value of 90 ± 2% towards −0.83 V vs Cc/Cc^+ applied potential, while H_2 is not observed across all potentials examined. CO production was ascribed to the electroreduction of CO_2 rather than parasitic decomposition of the electrolyte, based on mass spectroscopic analysis of the effluent gas stream during polarization in the presence of $^{13}CO_2$ (see Section 2.7.3 for experimental details). To characterize the chemical identity of the solution-phase product(s) comprising the faradaic balance, the catholyte was sampled via ^1H NMR following constant current electrolysis in the presence of $^{13}CO_2$ (see Section 2.6.6 for details). A doublet centered at 8.54 ppm was observed, characteristic of ^{13}C-formate (**Figure S2.11**), indicating that formate production also originates from the reduction of CO_2. We stress that careful analysis of the potential-dependent formate faradaic efficiencies and rates is challenged by the low molar quantities produced, while the accuracy of the calculated faradaic balance is dependent on the error

associated with measurement of the gaseous products. Owing to these potential sources of error, we refrain from the detailed interpretation of the formate production rates and selectivity. However, no other electrogenerated products were detected via ^{1}H or ^{13}C NMR, suggesting the near complete suppression of HER in favor of C_1 product formation.

To meaningfully compare CO_2RR selectivities in aqueous electrolytes and the DMSO/AcOH system at comparable applied potentials, the proton activity of each system must be determined. In water, the proton activity of the electrolyte is described by the pH, which can be easily calculated from the acid–base dissociation constant of the proton donor. This value can then be used to reference the data to the reversible hydrogen electrode (RHE) scale. In an aprotic solvent, however, the analytical determination of the proton activity is complicated by the presence of multiple solution non-idealities, such as homoconjugation and ion pairing,[28] whose complex equilibria are not conveniently characterized. To circumvent this issue, the proton activity of the system can instead be empirically determined from the equilibrium potential of the H^+/H_2 redox couple on Pt electrodes, which is directly sensitive to the activity ratio of the donor (a_{HA}) to the conjugate base (a_A-).[29,30] The measured equilibrium potential can then be used to reference the applied potentials depicted in **Figure 2.2a** to the RHE scale, permitting a comparison between the aqueous and aprotic systems.

Applying this analysis demonstrates the advantage of operation in DMSO/AcOH compared to water. **Figure 2.2b** shows the faradaic efficiency trends of CO and H_2 referenced to RHE (see Section 2.6.7 for experimental details; see **Figures S2.10–S2.12** for the equivalent plots for formate). The potential-dependent CO selectivity in DMSO/AcOH is comparable to those in fully carbonated electrolytes. For example, the FE for CO was previously reported to be 98% at ca. −0.7 V vs RHE in the fully carbonated pH 6.8 $KHCO_3$ electrolyte.[31] In contrast, the FE for CO is ca. 90% in DMSO/AcOH at the same applied potentials vs RHE. In addition, the overpotentials required to achieve selective CO formation in DMSO/AcOH are less than those in acidic aqueous electrolytes. For example, in pH 1 H_2SO_4 + 0.4 M K_2SO_4 electrolyte on a Au/C catalyst,[17] polarization at −0.7 V vs RHE is completely unselective for CO, in contrast to the ca. 90% selectivity observed for CO production in DMSO/AcOH. Achieving comparable selectivity in such acidic aqueous media is possible but requires an applied potential of −1.0 V vs RHE, where the additional 0.3 V of applied overpotential is required to sustain a high interfacial pH gradient. Together, the data demonstrate that DMSO/AcOH electrolyte is not only capable of supporting selective electroreduction of CO_2 to CO and formate, but that the reaction does so at comparable or less negative potentials versus RHE relative to aqueous neutral or acidic electrolytes.

2.3. Selective Electrolysis to C_1 Products Is Tolerated in DMSO/AcOH with up to 1 M of Added Water

Water is an inevitable reaction product of the cathodic deoxygenation of CO_2. However, it is unclear whether having a high water content in the electrolyte would erode CO_2 reduction selectivity in favor of HER. To examine the influence of added water on the product distribution, galvanostatic electrolyses were conducted in CO_2 saturated DMSO/AcOH electrolytes with 1 M added water ("wet DMSO/ACOH"). The orange data in **Figure 2.2a** evinces that a high CO selectivity (84 ± 4%) can still be achieved at sufficiently negative potentials (ca. −0.73 V vs Cc/Cc^+). Indeed, the faradaic efficiency for CO is comparable to that in native DMSO/AcOH on the RHE scale (**Figure 2.2b**). However, **Figure S2.12** demonstrates that the rate of CO formation is enhanced with the addition of water, demonstrating that the invariance in FE is not due to a corresponding invariance in CO formation rates. We speculate that the enhancement in CO formation rate with added water can be ascribed to hydrogen bond stabilization of the anionic surface-adsorbed $*CO_2^{\bullet-}$ intermediate, which lowers the free energy barrier for the rate-determining step for CO_2RR to CO on Au.[4]

Unlike in DMSO/AcOH, H_2 is observed under the tested galvanostatic range. To understand if the promotion of H_2 evolution originates from a change in the proton activity of the medium, **Figure 2.2b** depicts H_2 formation faradaic efficiencies versus the RHE reference scale. The increase in the H_2 faradaic efficiency at common potentials versus RHE in DMSO/AcOH versus wet DMSO/AcOH implies that the addition of water promotes H_2 formation. Despite this, low faradaic efficiencies for H_2 (∼5%) can still be achieved with sufficiently negative applied potentials. The low faradaic efficiency for H_2 is also stably maintained during prolonged electrolysis over the course of 4 hours (**Figure S2.4**). While the faradaic efficiency for CO steadily decreases from 97% to ca. 80% over a shorter time span of 100 min, the faradaic efficiency recovers upon transfer of the working electrode to a fresh electrolyte solution, suggesting that this variation over time is not due to electrode degradation but rather changes in solution composition in this un-optimized cell (see Section 2.7.1 for full details and discussion). Given the hygroscopic nature of DMSO, we acknowledge that sustaining the operation of this system would ideally require the continuous removal of water as its produced from CO_2 deoxygenation. This could be accomplished within the cell upon the development of efficient and selective catalysts for water oxidation in this medium or can be carried out externally to the cell by, for example, membrane-based pervaporative dehydration of the electrolyte;[32,33] either approach requires substantial development in future studies (see Section 2.7.1 for the discussion of additional considerations). Nevertheless, the data indicate that a high selectivity for C_1 products can still be maintained at sufficiently negative applied potentials in electrolytes containing substantial amounts of added water.

2.4. (Wet) DMSO/AcOH Electrolyte Resists Electrolyte Carbonation

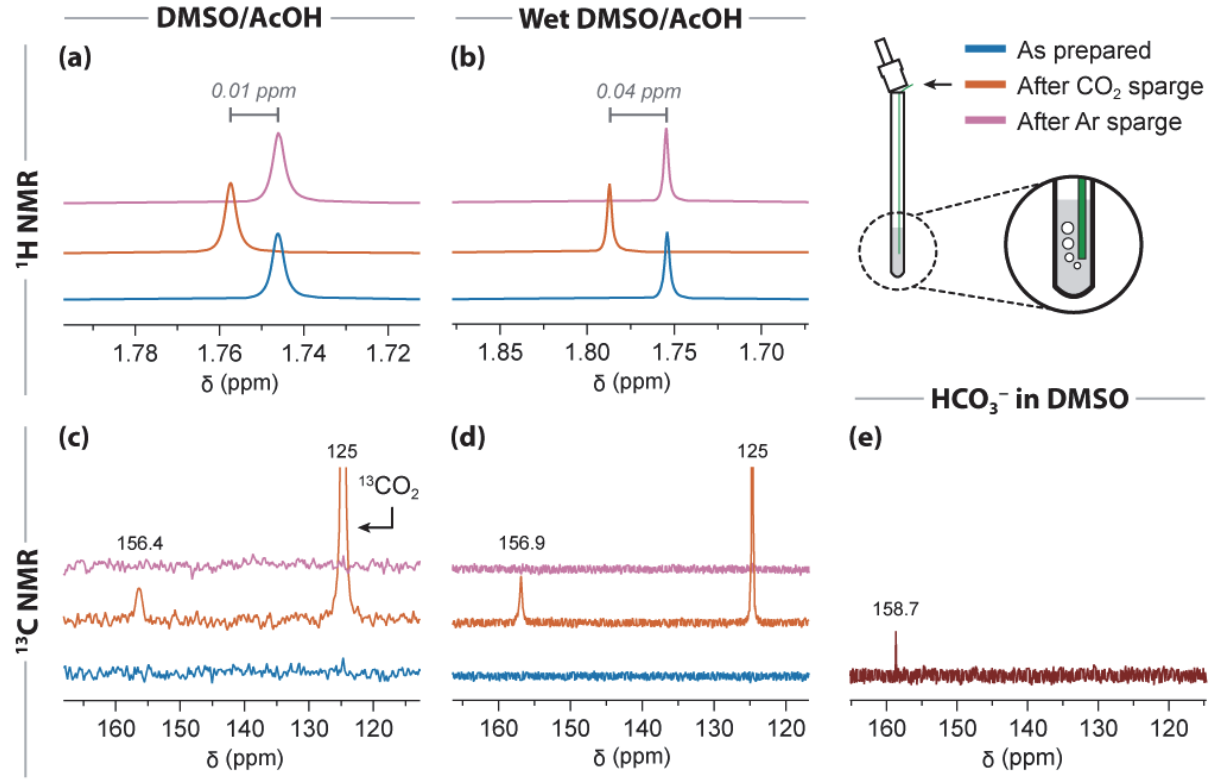

Figure 2.3. (a,b) ^{1}H NMR spectra depicting the acetate methyl shift in (a) DMSO/AcOH and (b) wet DMSO/AcOH electrolytes, and (c,d) ^{13}C NMR of (c) DMSO/AcOH and (d) wet DMSO/AcOH electrolyte under the following conditions: as prepared (blue), after sparging with $^{13}CO_2$ (orange), and after sparging with Ar (pink). (e) ^{13}C NMR reference spectra of tetraethylammonium bicarbonate ($TEAHCO_3$) in DMSO. For visual clarity, data in panel (c) are modified with a 20 Hz exponential apodization function.

After observing high CO_2RR selectivity, we sought to understand if the usage of AcOH/AcO^- buffer as the proton-donating medium also results in substantially reduced electrolyte carbonation. First, we sought to understand if acetate anion irreversibly forms an adduct with CO_2 via nucleophilic attack, which is one pathway for electrolyte carbonation with an exogenous donor. In order to probe a potential irreversible reaction between acetate and CO_2, ^{1}H NMR spectra were recorded on gas-tight samples of DMSO/AcOH and wet DMSO/AcOH prior to and after sparging with $^{13}CO_2$ (see Section 2.6.5 for experimental details). Introduction of CO_2 to the electrolyte causes a nominal change in the chemical shift of the acetate methyl resonance in both DMSO/AcOH (**Figure 2.3a**) and wet DMSO/AcOH (**Figure 2.3b**) of <0.05 ppm, evincing a weak interaction between CO_2 and AcOH/AcO^- buffer. The small change in chemical shift could be attributed to the weak interaction between CO_2 and acetate, or a change in speciation of AcOH/AcO^- buffer, or both. Regardless, subsequent sparging of the electrolyte with Ar causes the acetate methyl

resonance to return to its native chemical shift, suggesting that the interaction between AcOH/AcO^- buffer and CO_2 is indeed reversible.

Next, we sought to understand if significant equilibrium concentrations of (bi)carbonate are formed from the hydration of CO_2 with water in the presence of the AcOH/AcO^-. Upon saturation with $^{13}CO_2$, the ^{13}C NMR spectra of DMSO/AcOH (**Figure 2.3c**) and wet DMSO/AcOH (**Figure 2.3d**) electrolyte both display a carbon signal centered at 156–157 ppm. The chemical shift of this signal is very similar to that of bicarbonate in DMSO, whose shift was independently measured to be 158.7 ppm (**Figure 2.3e**). Hence, we ascribe the signal primarily to the presence of equilibrium bicarbonate species. However, the saturation of both electrolytes with Ar thereafter eliminates the bicarbonate resonance, implying that, unlike aqueous alkaline electrolytes, CO_2 capture is reversible in this reaction medium. Quantitative ^{13}C NMR analysis of the $^{13}CO_2$ saturated electrolyte samples reveals an equilibrium bicarbonate concentration of ca. 6 mM in DMSO/AcOH and ca. 41 mM in wet DMSO/AcOH (see Section 2.6.5 for experimental details). Both these concentrations are far below the estimated concentration of soluble CO_2 of ca. 0.157 M in DMSO/AcOH and ca. 0.152 M in wet DMSO/AcOH. Importantly, the low equilibrium bicarbonate concentration comprises a small fraction of the total anionic charge in the medium. The analytical concentration of acetate added to the electrolyte is 0.150 M, and the total anion concentration must be preserved regardless of the equilibrium speciation; thus, bicarbonate constitutes only 4 and 27% of base-derived anionic charge. These fractions and concentrations are significantly lower than the hundreds-of-millimolar quantities of (bi)carbonate expected from quantitative irreversible carbonation in alkaline aqueous electrolytes.

The low equilibrium concentration of bicarbonate in DMSO/AcOH reflects the similarity in the acidity of the AcOH/AcO^- and the CO_2/HCO_3^- acid–base equilibria in DMSO. To further understand this, the pK_a of the CO_2/HCO_3^- equilibrium was estimated by calculating the proton activity differences of two independent solutions of each buffer via the equilibrium H^+/H_2 reaction on Pt (see Section 2.7.4 for experimental and mathematical details). We stress that this calculation is an estimate and that a fully accurate determination of the pK_a requires explicit knowledge of all solution equilibria and any non-idealities in species' activities. Nevertheless, in acknowledging that the errors are expected to be small on a logarithmic scale, we calculate a pK_a value of 13.0 for the CO_2/HCO_3^- equilibrium. This value is similar to the pKa of 12.6 for AcOH/AcO^- in DMSO[28] implying that some carbonation is expected in the presence of trace water, formed via equilibrium H_2CO_3 deprotonation. Despite this, our analysis demonstrates that by suppressing the water content in the electrolyte and by using a buffer with a pK_a closely matched to the CO_2/HCO_3^- acid–base equilibrium, carbonation can be reduced to millimolar equilibrium concentrations in an aprotic solvent. Importantly, the similarity of the CO_2/HCO_3^- pK_a to that of AcOH/AcO^- is consistent

with previous CO_2RR studies reporting a high CO_2-to-C_1 formation selectivity in aprotic solvents, where CO_2/HCO_3^- is the sole proton-donating medium.[23]

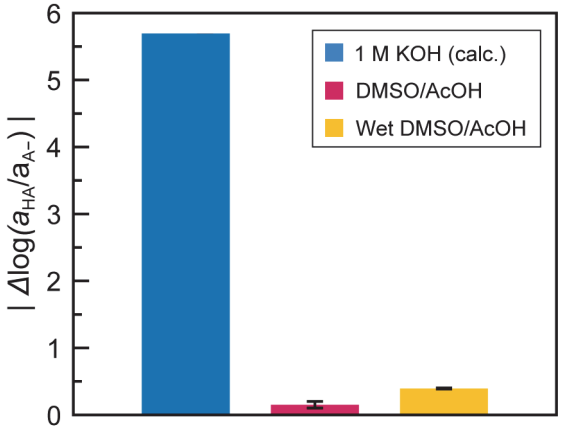

Figure 2.4. Difference in proton activity of 0.1 M KOH (blue), 0.1 M $KHCO_3$ (light blue), DMSO/AcOH (purple), and wet DMSO/AcOH (light purple) electrolytes before and after exposure to 0.5 atm Ar and 0.5 atm CO_2. The proton activity was sampled via the equilibrium potential of H^+/H_2 redox couple on the Pt electrode. In both conditions, 0.5 atm H_2 was present to maintain Nernstian equilibrium. The data points and error bars correspond to the average and standard deviation of triplicate measurements.

The results discussed above imply that exposure of the electrolyte to CO_2 should not cause a significant change in the proton activity of the medium. To assess this, the equilibrium potential of the H^+/H_2 redox couple was measured under 0.5 atm partial pressure of Ar, followed by exposure to 0.5 atm partial pressure of CO_2. In both atmospheres, the H_2 partial pressure is held constant at 0.5 atm to maintain the H^+/H_2 reaction equilibrium. The difference in the measured equilibrium potentials was then converted to a proton activity difference via the Nernst equation. **Figure 2.4** demonstrates that the proton activity changes by 0.15 ± 0.05 units in DMSO/AcOH and 0.39 ± 0.01 units in wet DMSO/AcOH upon exposure to CO_2 (see **Figure S2.13** for the difference in equilibrium potential in these electrolyte media). For comparison, both changes are far less than the 5.76 ± 0.01 unit change in pH observed in 0.1 M KOH electrolyte upon exposure to CO_2. It is also lower than the 1.49 ± 0.01 pH change observed in 0.1 M $KHCO_3$ (**Figure S2.4**), although we note that this electrolyte is fully carbonated. Hence, unlike in neutral-to-alkaline aqueous electrolytes, this result confirms that selective CO_2RR in DMSO/AcOH can occur after the electrolyte has reached chemical equilibrium with CO_2.

We note that while (bi)carbonate species could be electrochemically generated at the interface, our results suggest that such species are transient. For example, previous literature has suggested that carbonate can be formed from an electroreductive disproportionation pathway involving two equivalents of CO_2.[34] Recent literature has contested this observation, suggesting instead that bicarbonate formation appears because of nucleophilic attack of hydroxide on CO_2 following the direct reduction of water.[26] The data

presented above demonstrate that AcOH/AcO$^-$ sets the thermochemistry of proton transfer in the electrolyte. Hence, regardless of the pathway of its formation, electrogenerated (bi)carbonates are expected to rapidly equilibrate with AcOH/AcO$^-$ to establish a low bulk equilibrium bicarbonate concentration.

In summary, the data demonstrate that CO_2 is largely inert to DMSO/AcOH electrolytes and results in a negligible change in the proton activity of the medium upon its introduction, even with 1 M of added water. Furthermore, electrolyte carbonation can be significantly inhibited to millimolar levels by driving the thermodynamics of proton transfer and PCET with AcOH/AcO$^-$ buffer, in addition to attenuating the bulk water content of the electrolyte. These results contrast with CO_2RR in aqueous electrolytes, where proton donation in any pH regime comes at the cost of either low electrolyte carbonation or high CO_2RR faradaic efficiency at low overpotentials.

2.5. Conclusions

In this study, we sought to understand if selective CO_2 electroreduction catalysis could be balanced with minimal electrolyte carbonation in an aprotic electrolyte medium containing a non-nucleophilic buffer. We find that CO_2 electroreduction catalysis on pc-Au cathodes in DMSO/AcOH electrolyte affords high selectivity for C_1 products without concomitant HER at comparable potentials versus RHE relative to those previously reported in neutral aqueous electrolytes and less negative than those in acidic aqueous electrolytes. With AcOH/AcO$^-$ buffer and an attenuated water content, we find that DMSO inhibits electrolyte carbonation to millimolar equilibrium bicarbonate concentrations. Furthermore, the proton activity of DMSO/AcOH media is largely unchanged upon CO_2 addition, demonstrating that the pK_a of CO_2/HCO_3^- is closely matched to that of AcOH/AcO$^-$. Together, our findings suggest that attenuating the water content in an organic media alongside usage of a non-nucleophilic buffer with a matched pK_a is an effective strategy for simultaneously mitigating carbonation and HER. We acknowledge that the practical device implementation of aprotic solvent-based CO_2RR systems is far from mature, requiring simultaneous advances in anode reactivity, electrolyte conductivity, water management, and cell and membrane design. In particular, the development of solvophobic gas-diffusion electrodes that are compatible with aprotic solvents would be highly desirable. However, the approach described here addresses a fundamental knowledge gap in how the activity of water, the pK_a of the proton donor, and the nucleophilicity of conjugate base can be tailored to *decouple* selective CO_2 reduction and electrolyte carbonation. By addressing this core fundamental challenge in CO_2RR, this work establishes electrolyte design principles for fostering selective fuel synthesis with minimal energy and carbon losses.

2.6. Experimental Methods

The experimental procedures described in the following sections are modified versions of those described in Chapter 3, and are described again in full detail here for convenience.

2.6.1. Chemicals and materials

Unless stated otherwise, all chemical and cell components were handled using non-metallic instruments (spatula, vials, containers, etc.) to minimize trace metal contamination.

Used as received. The following chemicals were used as received; any chemicals or materials requiring additional preparation are described in their own subsection below. MilliQ water (Millipore Type 1, 18.2 MΩ cm) was used as the source of ultrapure water for all applications described below; dimethyl sulfoxide (DMSO, MilliporeSigma, 99.9999% purity by trace inorganic analysis); acetic acid (AcOH, MilliporeSigma, glacial, ≥99.99% trace metals basis); tetrabutylammonium acetate (TBAAcO, MilliporeSigma, >99.9% for electrochemical analysis), stored under N_2 atmosphere; tetrabutylammonium hexafluorophosphate ($TBAPF_6$, MilliporeSigma, >99.99% for electrochemical analysis); tetrabutylammonium bromide (MilliporeSigma, ≥98.0%); bis(cyclopentadienyl)cobalt(III) hexafluorophosphate ($CoCp_2$, MilliporeSigma, 98%); tetraethylammonium bicarbonate ($TEAHCO_3$, MilliporeSigma, ≥95.0%), stored under N_2 atmosphere; d^6-dimethylsulfoxide (d^6-DMSO, MilliporeSigma, 99.9 atom % D, or 99.5 atom % D); sulfuric acid (EMD Millipore, 95 − 98%); hydrogen peroxide (VWR, 30% w/w, stabilized); hydrochloric acid (MilliporeSigma, ACS grade); nitric acid (VWR Chemicals, 68-70%, ACS grade); potassium hydroxide (Alfa Aesar, 99.98% trace metals basis); potassium bicarbonate (MilliporeSigma, >99.95% trace metals basis, 99.7-100.5% dry basis); hydrogen gas (Airgas, Ultra High Purity); argon gas (Airgas, Ultra High Purity); ^{13}C carbon dioxide (MilliporeSigma, <3 atom % ^{18}O, 99.0 atom % ^{13}C).

Preparation of piranha acid. Piranha acid was prepared from a 4:1 v/v ratio of sulfuric acid to hydrogen peroxide.

Safety precaution: *Piranha acid is a highly reactive and corrosive liquid, and forms gases at the start of and for hours after its preparation; great care must be taken to safely use and dispose of it. Piranha acid was prepared and handled within a secondary container in an acid hood. Once used, piranha solutions were treated via addition of small amounts of an aqueous solution of 1 M solution of $FeCl_3$ and heated to 50 °C to accelerate peroxide decomposition. Once bubble formation was visibly complete, the solution was poured into a plastic-coated glass waste bottle, left to stand for one week to further cure the solution, sealed with a vented cap, and then disposed of as chemical waste.*

Preparation of aqua regia. Aqua regia was prepared from a 3:1 v/v ratio of hydrochloric acid to nitric acid.

Preparation of pc-Au working electrode. A polycrystalline Au metal flag was prepared and assembled in the following manner. First, a pc-Au foil (Thermo Scientific, ≥99.999% metals basis, foil, Premion, 0.25 mm thickness) was cut from a sheet and cleaned by abrasion with sandpaper (Grainger, ultra-fine 1500 Grit Silicon Carbide), followed by immersion in piranha acid for 5 minutes. A polycrystalline Au metal wire (BeanTown Chemical, ≥99.999% trace metals basis, 0.762 mm diameter) was then hammered onto the foil via a paper spacer to avoid direct contact of the hammerhead and gold; this wire served as a lead for the potentiostat clip. This assembly was then rinsed in aqua regia for ca. 10 seconds, and then polished with a polycrystalline diamond suspension (Buheler, 3 μm, MetaDi Supreme) on a polishing pad. Thereafter and prior to every experiment, the flag was cleaned by immersion in piranha acid for at least 10 minutes. The flag was then rinsed with copious amounts of MilliQ water and dried under a stream of air or in a 120 °C oven. Following electrolysis, the electrode was rinsed with acetone, then water, and stored under ambient conditions.

Preparation of Ag/AgCl reference electrode. A Ag/AgCl leakless reference electrode (EDAQ) was utilized as a pseudo reference electrode. Prior to electrolysis, the electrode was rinsed with water and dried under a stream of air. Following electrolysis, the electrode was rinsed with acetone, then water, and stored in water.

Preparation of Au mesh counter electrode. The Au mesh counter electrode (BeanTown Chemical, ≥99.99% trace metals basis, 52 mesh gauze woven from 0.102 mm wire) was physically affixed to a Au wire (BeanTown Chemical, ≥99.999% trace metals basis, 0.5 mm diameter) to form the counter electrode assembly. Prior to use, the counter electrode was cleaned with piranha acid and stored in the same manner as the Au flag working electrode.

Preparation of the Pt gas diffusion working electrode (GDE). Pt GDEs were prepared similarly to previously reported methods.[35,36] A Pt layer was sputter-deposited onto polytetrafluoroethylene (PTFE) membrane (Sterlitech Corp., QL217: polypropylene backer, thickness 6 – 10 mil, pore size 0.1 – 0.2 micron) from a Pt target (99.99%) using an AJA sputtering system. The sputtering rate was 1 Å s^{-1} and the deposition was carried out for 50 min to reach a nominal thickness of 300 nm. Strips of Pt GDE (2 x 1 cm) were then cut from a larger sheet using a CNC cutting machine (Cricut Maker). The strips were then affixed to a Pt wire (Thermo Scientific, ≥99.95% trace metals basis, annealed, 1.0 mm diameter) and threaded through a septum to interface with the cell. Note that Pt GDEs were utilized as a source of high surface area platinum, and whether they form a solvophobic gas layer was not rigorously determined from our studies.

Preparation of Nafion membrane. Nafion 117 (Fuel Cell Store) was used as the separator and prepared in the following manner to eliminate acidic impurities. First, Nafion was cut into ca. 1.5 x 1.5 cm^2 squares with ceramic scissors. Ten films were soaked at a time in 40 mL of a 1 M solution of tetrabutylammonium bromide in DMSO for at least an hour. The containing solution turned yellow, presumably due to the formation of hydrogen bromide, indicating successful exchange. The films were then rinsed twice with pure DMSO, soaked for an hour, and then rinsed once again before use. All remaining films were stored in neat DMSO.

Preparation of (wet) DMSO/AcOH electrolyte. DMSO and $TBAPF_6$ were stored and handled under ambient atmospheric conditions. Electrolyte solutions were prepared by mixing DMSO and the corresponding amount of AcOH and TBAAcO in conical centrifuge tubes (Corning). $TBAPF_6$ was added to form solutions of a constant ionic concentration of 0.3 M of TBA^+ cation. Wet DMSO/AcOH electrolyte was prepared by adding 1 M water to the solution.

2.6.2. General procedure for galvanostatic polarization experiments

Preparation of divided H-cell

Cleaning of H-cells. All Au polarization measurements were conducted in a custom-made glass body H-cell (James Glass Inc.). Prior to assembly, all glass components were soaked in piranha acid for at least an hour to remove trace organic and metallic residues. The cells were then further cleaned by extensive rinsing in Milli-Q water and dried in an oven at 120 °C for at least an hour where they were stored. Plastic components of the cell, including screw caps (Chemglass) and O-rings (Chemglass, Viton), were washed with ethanol, dried, and stored in a 60 °C oven for at least 24 hours.

Assembly of H-cells. The cathode compartment, the working, and the reference electrode were rinsed with neat DMSO prior to assembly. All components not connected via a septum were sealed to the cell using a #7 screw cap and Viton O-ring assembly (Chemglass). Unless otherwise specified, the Au mesh electrode was utilized as the counter electrode. CO_2 or Ar gas was aerated in the working compartment through a porous glass frit, while the out flow of the cell was connected directly to a gas chromatograph for gaseous product detection (SRI Instruments, Multi-Gas Analyzer #3). Gas flow was controlled using mass flow controllers (Alicat or Brooks) typically set to 30 mL min^{-1} of CO_2 or Ar flow. The working compartment, filled with ca. 17 mL of solution, was continuously stirred at 1500 RPM (IKA) with a magnetic PTFE stir bar (VWR). After assembly and prior to electrolysis, the cell was left to equilibrate for at least 15 minutes.

Measurement sequence

All electrochemical experiments described herein were conducted with a Gamry Reference 600 potentiostat.

Pre-polarization. The Ohmic drop was measured via potentiostatic electrochemical impedance spectroscopy (PEIS) prior to measurement between 1 MHz and 50 Hz with an AC voltage amplitude of 5 mV rms. The resistance value was taken at the minimum measured phase angle at the high frequency limit: this value was used for post-electrolysis iR correction during data workup. Then, linear sweep voltammetry was conducted from the measured open circuit potential to ca. −6 mA under CO_2 atmosphere. The cathode was then preconditioned under galvanostatic polarization at −2 mA for 450 seconds, corresponding to 0.3 C passed per cm^2 of electrochemically active surface area of the electrode to reduce any possible surface oxides formed prior to insertion of the working electrode into the cell.

Polarization. To collect steady-state polarization data, chronopotentiometry experiments were conducted sequentially and in tandem with gas chromatographic sampling of the effluent gas stream (see "Gaseous product analysis" below for details). Because each gas chromatographic measurement took 20 minutes to complete, galvanostatic polarization was conducted sequentially for 7.5 minutes, followed by 12.5 minutes of delay at OCP. Polarization was stepped from lowest to highest applied current in the order of −0.5 mA, −0.75 mA, −1 mA, and then 1 mA interval steps thereafter up to −6 mA. The potential of product formation was sampled by averaging the potential values of the latter half of the chronopotentiogram, during which the reaction was taken to be at steady state.

In an aprotic non-aqueous electrolyte, polarization can induce changes to the bulk concentration of donor / conjugate base over time and convolute kinetic measurements for products which have a rate dependence on the donor. Using galvanostatic control of the reaction, and assuming that electrons and protons are transferred as equimolar equivalents (for either hydrogen evolution or CO_2 reduction), this procedure ensures that the initial donor concentration does not deviate by more than 5% for any set of polarization experiments conducted in a single cell.

Post-polarization. Following polarization, a small amount (~1 mg) of $CoCp_2$ was added to the cell and the half-wave potential was measured via cyclic voltammetry at 100 mV s^{-1} using a glassy carbon disk working electrode (BASi) without stirring and without agitation from the gas input. All potentials reported are converted to the cobaltocene/cobaltocenium (Cc/Cc^+) reversible couple.

Gaseous product analysis. All gaseous products were identified and quantified via gas chromatography following a literature protocol.[37] The product stream was sampled 1 minute prior to the end of the electrolysis by injection of the effluent stream into the chromatograph. Effluent separation was

accomplished with a MolSieve 13X and Hayesep D column connected in series (SRI Instruments), while detection was accomplished with a thermal conductivity detector (TCD) and flame ionization detector (FID) (SRI Instruments). The peak position and quantity of gaseous products were calibrated to a custom-order gas standard (Airgas). The partial current density for each product was calculated using the following equation, where c_i is the GC detected product in ppm, n_i is the electron stoichiometry for product i, F is Faraday's constant (96485 C mol^{-1}), V_{gas} is the substrate gas flow rate, P is the pressure in the cell (1 atm) and A is the electrochemically active surface area (ESCA, see SI section 1.4).

$$j_i = c_i * n_i * F * V_{gas} * \frac{P}{RT} * \frac{1}{A}$$

The faradaic efficiency is calculated by dividing the partial current of a product by the applied current for a given electrolysis experiment. Faradaic efficiency that could not be accounted for from gaseous product quantification was further investigated by analyzing for solution-phase products, as described in the main text.

Data workup and analysis

The foregoing procedure produces the data gathered in **Figures 2.2**, **S2.10**, and **S2.12**. The data points and error bars correspond to the average and standard deviation of triplicate measurements, while all reported current densities were calculated using the ECSA (see section 0). Every instance of a replicate employed a freshly cleaned cell assembly, reference electrode, Nafion separator, Au counter electrode, electrolyte solution, and cleaned Au foil cathode.

2.6.3. Estimation of the adventitious water concentration in DMSO solvent

The water content in the DMSO solvent was estimated via ^{1}H NMR quantification of the water signal in DMSO electrolyte containing 0.3 M $TBAPF_6$, using the latter as an internal standard, with a relaxation delay of 2 s. The value of the water content measured in this manner was 9 ± 3 mM (n = 2).

2.6.4. Measurement of the electrochemically active surface area (ECSA) of the working electrode

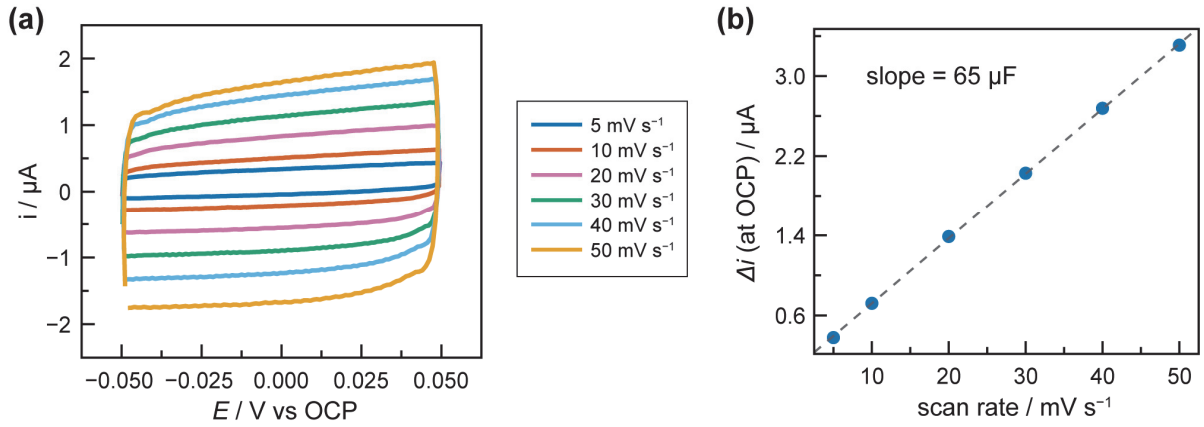

Figure S2.1. (a) Cyclic voltammograms (CV) collected on pc-Au foil in DMSO/AcOH buffer at various scan rates for determination of surface capacitance, following galvanostatic steady-state electrolysis. Scans are centered around the OCP, which was measured prior to the start of each scan and defined by the last measured potential after 10 s passed. (b) Plot of the difference between cathodic and anodic currents at the OCP for each CV as a function of scan rate. The slope value is obtained from a linear fit to the data.

The electrochemically active surface area (ECSA) of the Au foil was measured using a previously reported double-layer capacitance method.[38] The surface capacitance of the electrode was measured following electrolysis in DMSO/AcOH buffer. After equilibration of the cell to the open-circuit potential (OCP) for 10 s, the potential was swept within a 100 mV window centered on the OCP at 5, 10, 20, 30, 40, and 50 mV s^{-1} (**Figure S2.1a**). The capacitance was determined from a slope of a plot of the difference between cathodic and anodic current at the OCP versus the scan rate (**Figure S2.1b**). This capacitance value was then divided by the reported calibration value of 11 uF cm^{-2} to obtain the ECSA of the foil of 2.957 cm^2. All reported current densities utilizing the foil are normalized to this ECSA value.

2.6.5. ^{1}H and ^{13}C NMR analysis of electrolyte solutions

NMR analysis of electrolyte samples exposed to either CO_2 or Ar gas were prepared in airtight J Young NMR tubes with either a 9:1 or 4:1 v/v ratio of h^6-DMSO:d^6-DMSO. Gas was delivered into the sample using PEEK tubing at 5 mL min^{-1}. To determine the point of saturation, the flow rate of the gas exiting the tube was measured using a mass flow meter (Alicat) until stability was reached. Determination of the chemical shift of the acetate methyl group under various gaseous atmospheres was conducted on a 400 MHz spectrometer (Bruker Avance-III HD Nanobay). All other experiments were conducted on a 500 MHz spectrometer (Bruker Avance Neo). ^{13}C quantitation experiments were conducted using a custom quantitative carbon-13 NMR protocol with inverse gated ^{1}H decoupling ('zgig30'). Using this protocol, each sample was measured with 120 scans and a relaxation delay of 60 s. Estimation of the concentration

of soluble carbon species was conducted using the concentration of TBA^+ cation as an internal standard. The foregoing procedure produces the data shown in **Figure 2.3**.

2.6.6. Characterization of ^{13}C enriched carbon monoxide and ^{13}C enriched formate production

Detection of ^{13}CO was accomplished via galvanostatic polarization with $^{13}CO_2$ in the cell setup described previously. The outflow of the cell was fed into a custom-built differential electrochemical mass spectrometer (Pfeiffer Vacuum), where the flow of 1 atm gas was reduced to ca. 5-6 × 10^{-5} mbar pressure via a porous PTFE membrane layered and pressed with PTFE tape. Gases were ionized with a cathode potential of −20.9 V, an emission current of 0.5 mA and a dwell time of 1 s and their intensities were monitored with a Faraday detector. To validate the integrity of the setup, polarization was initially conducted at −7 mA for 780 s under 1 atm of $^{13}CO_2$. Then, to produce **Figure S2.7**, the effluent stream was sampled without and with galvanostatic polarization at −7 mA for ca. 20 min under 0.9 atm $^{13}CO_2$ and 0.1 atm Ar, using the latter gas as a tracer.

Following analysis of ^{13}CO, additional polarization was conducted to accumulate formate; in total, −7 mA was applied for 6430 s, resulting in ca. 50 C of charged passed over the course of the entire experiment. Detection of ^{13}C enriched formate was conducted using ^1H NMR, producing the data in **Figure S2.11**.

2.6.7. Measurement of the H^+/H_2 equilibration potential on Pt working electrodes

Preparation of single-compartment cell

Electrochemical measurements were conducted in a 20 mL 3-neck round bottom flask (Chemglass). The cell was washed with acetone, water, and then dried and stored in a 120 °C oven prior to use. The Ag/AgCl reference electrode was prepared in the same manner as previously described and fitted through a septa to create an airtight connection to the cell. The Pt GDE, leakless Ag/AgCl reference electrode, and Pt mesh counter electrode were washed with pure DMSO prior to insertion into the cell. Approximately 10 mL of DMSO buffer solution was added to each cell to sufficiently submerge each electrode component. Gas was sparged through the cell using a metal needle sheathed in PEEK tubing, and gas was vented out the cell using a metal needle.

Measurements conducted in aqueous solutions were setup in the same manner, with the exception that a fritted Ag/AgCl reference electrode (CH Instruments) was utilized, and the cell components were cleaned with MilliQ water prior to insertion.

Measurement sequence

The flow rate of hydrogen, argon, or carbon dioxide gas was controlled using mass flow controllers (Alicat or Brooks), and their partial pressures were adjusted by adjusting the relative flow rates of each gas.

The open circuit potential was measured at each condition under gas flow until the potential approached equilibrium, defined by $\Delta E < |1\ mV|$ over a 100 s time window.

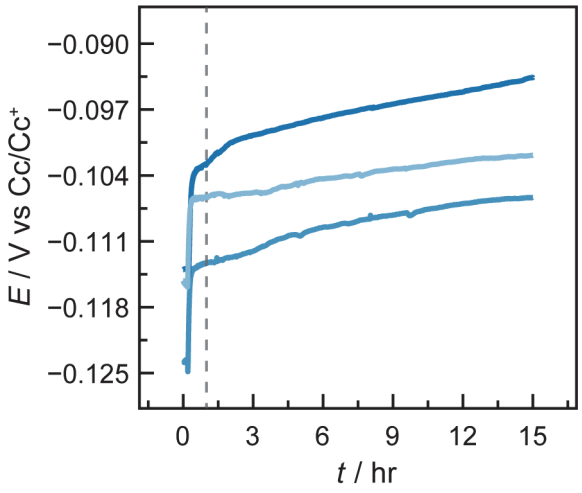

Figure S2.2. Open circuit chronopotentiograms of the H^+/H_2 redox couple in DMSO/AcOH electrolyte with 0.5 atm CO_2 and 0.5 atm H_2. Shades of blue are replicates of identical experiments. The dotted line indicates the time (t = 1 hr) where the equilibrium potential was chosen for each triplicate. All potentials are referenced to the cobaltocene/cobaltocenium (Cc/Cc^+) redox couple.

The only exception was in the determination in the equilibrium potential of DMSO/AcOH electrolyte in 0.5 atm partial pressure CO_2 (**Figure S2.2**). An initial change in the OCP upon exposure to CO_2 was observed over the course of minutes, which we ascribed to the minor formation of bicarbonates. However, a slow drift in the potential was continually observed over several hours. Though the measured change in potential due to this drift is small (ca. <10 mV) and does not impact the principal claims of the study, we opted to sample the equilibrium OCP value after 1 hour of measurement. This instability was not observed in wet DMSO/AcOH. The Cc/Cc^+ reference couple was measured at the end of each set of measurements conducted in a single cell for experiments conducted in DMSO. Each replicate in a DMSO-based electrolyte utilized a new cell assembly, including a new working electrode, cleaned reference electrode, and cleaned counter electrode.

Each replicate in an aqueous electrolyte was conducted with the same cell assembly, but utilized with a new working electrode and electrolyte solution, and the assembly rinsed with MilliQ water prior to measurement. For equilibrium measurements conducted in 1 M $KHCO_3$ under H_2/Ar gas flow, the measured OCP was found to drift towards more cathodic potentials over time, presumably due to the loss of CO_2 from the electrolyte from the equilibrium carbonation reaction from flow under inert atmosphere. In order to minimize this effect, the electrolyte was sparged through with H_2/Ar for 3 min prior to sampling the OCP, after which the gas flow was stopped to maintain a static atmosphere. The equilibrium potential was then sampled as the average potential across the first ca. 100 s of measurement.

Data workup and analysis

The foregoing procedure produces the data gathered in **Figures 2.4** and **S2.13**. Unless otherwise stated, the data and errors are the average and standard deviation of triplicate measurements. The measured equilibrium potential of DMSO/AcOH and wet DMSO/AcOH under 1 atm of H_2 is −0.125 ± 0.006 vs Cc/Cc^+ and −0.074 ± 0.003 vs Cc/Cc^+, and used to convert the relevant Cc/Cc^+ potentials to RHE in **Figures 2.2**, **S2.10**, and **S2.12**.

2.6.8. Linear sweep voltammetry of DMSO with and without added water under inert atmosphere

Linear sweep voltammograms to investigate the solvent reduction window were conducted in the same H-cell setup described previously under 1500 rpm stirring conditions at 50 mV s^{-1}. Voltammograms were collected in DMSO containing 0.3 M $TBAPF_6$ supporting electrolyte with and without added water. The data were iR corrected following the same procedure outlined in section 2.6.2, producing the data gathered in **Figure S2.9**.

2.7. Supplementary Discussion

2.7.1. Characterization of the reaction stability under extended polarization in wet DMSO/AcOH

While high CO_2RR faradaic efficiencies can be obtained in both DMSO/AcOH and wet DMSO/AcOH during polarization across several minutes, we sought to characterize the persistence of the reaction selectivity over the course of hours. High reaction selectivity is not expected to be maintained based on our current cell design for several reasons. First, as discussed later in section 2.7.2, Kolbe electrolysis at the anode could result in the irreversible consumption of the conjugate base at the anode, leading to an imbalance in the proton activity during polarization. Second, our current cell design does not include a method to clear out electrogenerated water in the catholyte originating from CO_2RR to CO. Third, while the Nafion membrane employed functions as a separator, it may not be an effective proton conductor in DMSO, leading to another possible source of proton activity imbalance in the catholyte during polarization.

Nevertheless, we sought to characterize the reaction selectivity over time to understand the extent of the aforementioned electrolyte effects on the reaction stability. To study this, the stability of the reaction in wet DMSO/AcOH was tested using the cell setup described in section 1.2. Then, following the described pre-polarization procedure, galvanostatic electrolysis was conducted at −5 mA, towards the upper limit of the galvanostatic range tested in **Figure 2.2**, for ca. 4 hours (14650 seconds). The effluent gas stream was continuously sampled via gas chromatography in 20-minute intervals, starting 7.5 minutes after the start of polarization. From this data, the faradaic efficiency of hydrogen and carbon monoxide production over time was determined. In addition, we sought to understand whether the reaction stability is a function of changes

in the bulk electrolyte, or due to degradation of the electrode itself. Hence, following polarization in the first cell (cell #1), the Au flag electrode was removed, rinsed in neat DMSO, and then transferred into another identically prepared cell (cell #2) where the aforementioned polarization procedure was conducted again under the same reaction conditions.

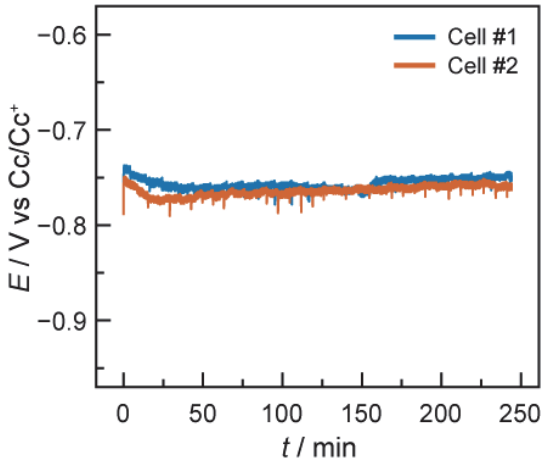

Figure S2.3. Chronopotentiograms of wet DMSO/ACOH at −5 mA applied current (−1.69 mA cm^{-2}) across ca. 4 hr (16450 s) using the same pc-Au working electrode sequentially in two otherwise identical cell setups (cell #1 and cell #2). All potentials are referenced to the cobaltocene/cobaltocenium (Cc/Cc^{+}) redox couple.

Both the applied potential and faradaic efficiencies are largely unchanged over time. **Figure S2.3** shows that the applied cathode potential for cell #1 is constant over time, spanning a range no greater than ca. 30 mV. This stability is maintained in cell #2, suggesting that the working electrode does not degrade substantially as a function of polarization.

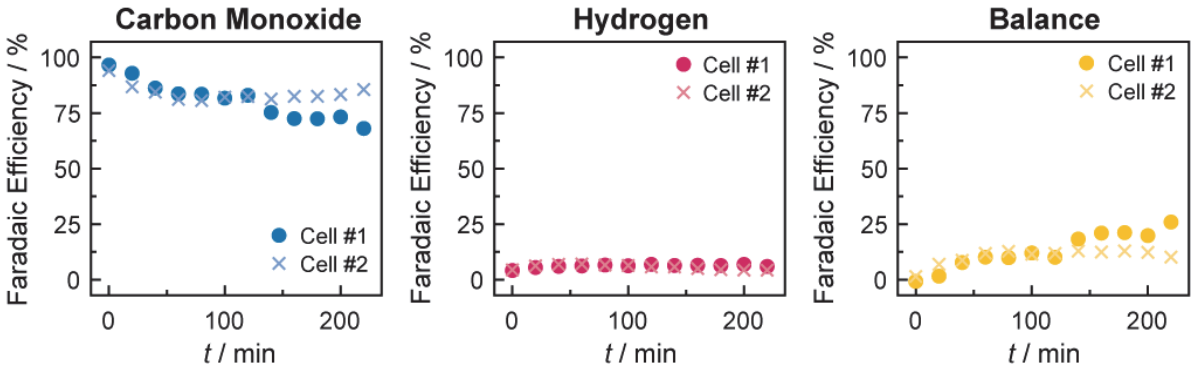

Figure S2.4. Time-dependent faradaic efficiency trends for CO (left), H_2 (middle), and the faradaic balance (right) in wet DMSO/AcOH during galvanostatic polarization at −5 mA applied current (−1.69 mA cm^{-2}) across 4 hr. The time is referenced to the first injected sample via gas chromatography, which occurred 7.5 minutes following the start of polarization.

These observations are largely consistent with the relatively stable faradaic efficiencies observed for carbon monoxide and hydrogen. **Figure S2.4** shows that while the selectivity for carbon monoxide in both

cells decreases from 97% to 81% across 100 min of polarization, a low selectivity for hydrogen is maintained at around 4-6% faradaic efficiency, showing that hydrogen can be effectively suppressed over long-time durations. Since the decay trend in CO FE is similar in both cells, we ascribe the origin of the decay to the change in the electrolyte composition during polarization. This change can be sampled by measuring the proton activity in both cells before and after polarization via the equilibrium H^+/H_2 potential measurement on Pt electrodes (as described in the main text). In doing so, the proton activity was found to increase by 0.67 ± 0.09 units (n = 2), suggesting that the selectivity is sensitive to the proton activity. Therefore, we expect that a high reaction stability can be maintained if the composition of the electrolyte can be properly managed, the comprehensive exploration of which is outside the scope of this proof-of-concept study.

2.7.2. Anodic decomposition of AcO^- can be avoided via the hydrogen oxidation reaction (HOR)

Kolbe electrolysis, which consists of the anodic decomposition of acetate anions to form carbon dioxide and ethane, has been well documented on a variety of anode materials such as Pt, Ir, and Au in aqueous and non-aqueous electrolyte media.[27] Since oxidative decomposition of acetate consumes the conjugate base of the buffer, and does not generate protons, this anode reaction irreversibly alters the proton activity of the electrolyte. As described in SI section 2.6.2, galvanostatic electrolyses were conducted to minimize significant consumption of the proton donor and their subsequent impact on the study of the reaction selectivity and kinetics. However, the presence of the Kolbe reaction at the anode ostensibly complicates the use of acetate as a proton carrier.

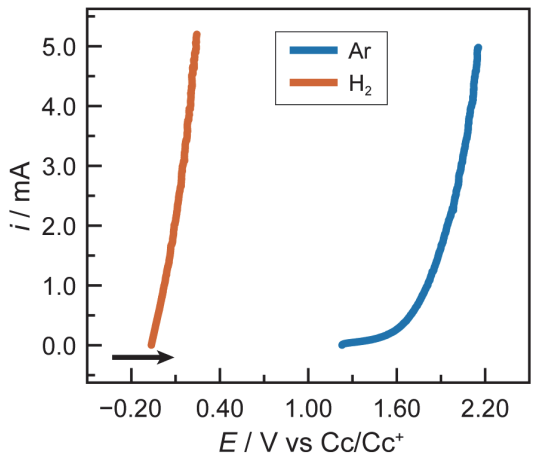

Figure S2.5. Linear sweep voltammograms of wet DMSO/AcOH electrolyte under Ar and H_2 atmosphere on a Pt gas diffusion electrode (Pt GDE). Scans were measured in the positive potential direction at 50 mV s^{-1} under stirring conditions as indicated by the black directional arrow. All potentials are referenced to the cobaltocene/cobaltocenium (Cc/Cc^+) redox couple.

To address these issues, we examined the hydrogen oxidation reaction (HOR) as a possible anodic reaction that could outcompete Kolbe electrolysis. **Figure S2.5** depicts linear sweep voltammograms of wet DMSO/AcOH in the presence of Ar and under H_2 up to 5 mA total current on a Pt GDE working anode. At the highest sampled current densities, oxidation under H_2 occurs at ca. 1.8 V positive of the electrolyte oxidation window, suggesting that HOR is the dominant process.

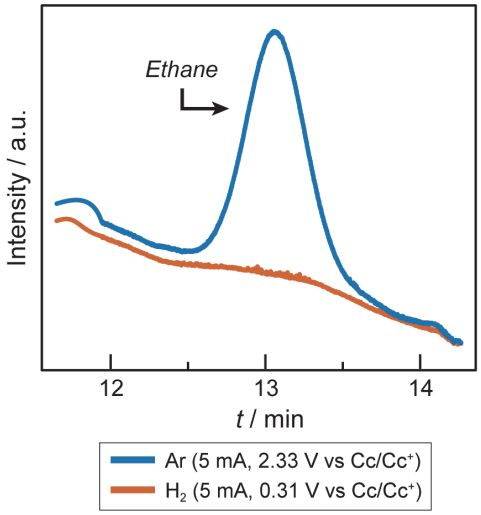

Figure S2.6. Gas chromatograph showing the retention time of ethane, sampled from the effluent gas from the anode compartment, following electrolysis under Ar (blue), and under H_2 (orange) using Pt GDE working anode. The time is labeled with respect to the start of the measurement, while the current and potential are labeled with respect to the Pt GDE anode as the working electrode.

To characterize the reaction products, galvanostatic electrolysis was conducted at −5 mA total current under Ar (ca. 2.33 V vs Cc/Cc^+). At this potential, gas chromatographic analysis of the effluent gas stream revealed a signal for ethane, suggesting that Kolbe electrolysis is the operative reaction (**Figure S2.6**). In contrast, upon polarizing at the same total current under H_2, the potential of the reaction shifted ca. 2 V positive (to 0.31 V vs Cc/Cc^+) and ethane was not observed in the chromatograph. Altogether, the voltametric and gas chromatographic data suggest that HOR can be employed to avoid the Kolbe electrolysis under the tested conditions and can be employed as a viable counter reaction in an aprotic electrolyte.

2.7.3. Mass spectrometric characterization of enriched carbon monoxide

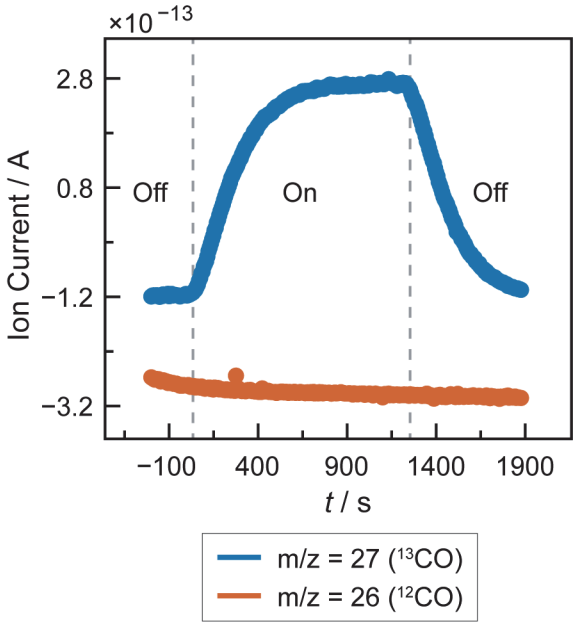

Figure S2.7. Ion current over time for ^{13}CO (blue, m/z = 27) and ^{12}CO (orange, m/z = 26) with and without applied galvanostatic polarization at −7 mA (as indicated by the dashed lines). The time is labeled with reference to the start of polarization.

To determine whether CO production originates from the electroreduction of CO_2, galvanostatic polarization in $^{13}CO_2$ was conducted in the cell setup described previously to generate detectable quantities of product. **Figure S2.7** depicts the ion current for the mass fragment corresponding to ^{13}CO (m/z = 27) and ^{12}CO (m/z = 26) during and in the absence of polarization. The rise in the ^{13}CO signal, and relative lack of change in the ^{12}CO signal, suggests that $^{13}CO_2$ is the substrate for CO_2RR to CO.

2.7.4. Estimation of the pK_a of the CO_2/HCO_3^- acid-base equilibrium in DMSO electrolyte

To understand the thermochemistry of PCET and of the equilibrium formation of bicarbonate in the electrolyte, the pK_a of both the CO_2/HCO_3^- equilibrium and AcOH/AcO^- must be determined. Since the pK_a of AcOH has been previously reported in DMSO (12.6),[28] the pK_a of the CO_2/HCO_3^- acid-base couple in DMSO can be estimated using the equilibrium potential difference of the H^+/H_2 redox couple on Pt working electrodes in solutions containing each acid-base pair. The solution containing AcOH/AcO^- buffer was prepared using the same formulation as previously described for DMSO/AcOH (0.150 M AcOH, 0.150 M TBAAcO, and 0.150 M $TBAPF_6$). The solution containing the CO_2/HCO_3^- buffer was prepared containing 0.224 M $TBAPF_6$, 1 M added water, and 0.076 M $TEAHCO_3^-$. The equilibrium OCP was measured using the procedure described in section 2.6.7, under 0.5 atm P_{H2} in each solution, balanced with 0.5 atm P_{Ar} in AcOH/AcO^- and 0.5 atm P_{CO2} in CO_2/HCO_3^-.

The equilibrium OCP of the AcOH/AcO$^-$ solution (E_1) was measured to be −0.070 vs Cc/Cc$^+$, while that of the CO_2/HCO_3^- solution (E_2) was −0.096 vs Cc/Cc$^+$. Using these values, the pK_a of CO_2/HCO_3^- can be estimated. First, the Nernst equation describing the equilibrium potential of the H^+/H_2 redox couple for a given acid (HA) and its conjugate base (A^-) is the following:[29]

$$HA + e^- \rightleftharpoons \frac{1}{2}H_2 + A^-$$

$$E_{HA} = E^o_{HA} - (0.059\ V)\log\left(\frac{a_{A-}a^{0.5}_{H2}}{a_{HA}}\right)$$

The standard state redox potential for HA (E^o_{HA}) is related to that of the free proton (E^o_{H+}) by its pK_a:

$$E^o_{HA} = E^o_{H+} - (0.059\ V)pK_a$$

Thus, the Nernst equation describing the AcOH/AcO$^-$ equilibrium (E_1) potential is described by the pK_a of the AcOH/AcO$^-$ acid-base pair (p$K_{a,1}$) and the Nernstian reaction quotient.

$$E_1 = E^o_{H+} - (0.059\ V)\left(pK_{a,1} + \log\left(\frac{a_{AcO^-}a^{0.5}_{H_2}}{a_{AcOH}}\right)\right)$$

However, the Nernst equation describing the CO_2/HCO_3^- equilibrium (E_2) is a composite of the CO_2 hydration equilibrium to form H_2CO_3, followed by its deprotonation to HCO_3^-.

$$CO_2 + H_2O \rightleftharpoons H_2CO_3 \rightleftharpoons H^+ + HCO_3^-$$

To determine E_2, the Nernst equation describing the H_2CO_3/HCO_3^- equilibrium must be modified by the CO_2 hydration equilibrium (K_{hy}), where p$K_{a,2}$ is the equilibrium acid-base dissociation constant for the H_2CO_3/HCO_3^- couple.

$$K_{hy} = \frac{a_{H_2CO_3}}{a_{CO_2}a_{H_2O}}$$

$$E_2 = E^o_{H+} - (0.059\ V)\left(pK_{a,2} + \log\left(\frac{a_{HCO_3^-}a^{0.5}_{H_2}}{a_{H_2CO_3}}\right)\right)$$

$$E_2 = E^o_{H+} - (0.059\ V)\left(pK_{a,2} + pK_{hy} + \log\left(\frac{a_{HCO_3^-}a^{0.5}_{H_2}}{a_{CO_2}a_{H_2O}}\right)\right)$$

In defining the pK_a of the CO_2/HCO_3^- equilibrium (p$K^*_{a,2}$) to be the sum of the acid-base dissociation constant of H_2CO_3/HCO_3^- and the CO_2 hydration equilibrium constant, we obtain an expression for the

Nernst equation for the net CO_2/HCO_3^- equilibrium. We note that this representation of the pK_a of the CO_2/HCO_3^- couple is consistent with the representation commonly employed in aqueous solvents.

$$\mathrm{p}K^*_{a,2} = \mathrm{p}K_{a,2} + \mathrm{p}K_{hy}$$

$$\mathrm{E}_2 = \mathrm{E}^{\mathrm{o}}_{\mathrm{H}+} - (0.059\ \mathrm{V})\left(\mathrm{p}K^*_{a,2} + \log\left(\frac{\mathrm{a}_{\mathrm{HCO_3^-}}\mathrm{a}^{0.5}_{\mathrm{H_2}}}{\mathrm{a}_{\mathrm{CO_2}}\mathrm{a}_{\mathrm{H_2O}}}\right)\right)$$

From here, p$K^*_{a,2}$ can be calculated from the measured difference in the OCP values of the two electrolyte systems. (Note that because the same partial pressure of H_2 was used in each experiment, those terms cancel out in the final expression):

$$\mathrm{E}_1 - \mathrm{E}_2 = (0.059\ \mathrm{V})\left(\mathrm{pK}^*_{\mathrm{a},2} + \log\left(\frac{\mathrm{a}_{\mathrm{HCO_3^-}}\mathrm{a}^{0.5}_{\mathrm{H_2}}}{\mathrm{a}_{\mathrm{CO_2}}\mathrm{a}_{\mathrm{H_2O}}}\right)\right) - (0.059\ \mathrm{V})\left(\mathrm{pK}_{\mathrm{a},1} + \log\left(\frac{\mathrm{a}_{\mathrm{AcO^-}}\mathrm{a}^{0.5}_{\mathrm{H_2}}}{\mathrm{a}_{\mathrm{AcOH}}}\right)\right)$$

$$\mathrm{pK}^*_{\mathrm{a},2} = \frac{\mathrm{E}_1 - \mathrm{E}_2}{0.059\ \mathrm{V}} + \mathrm{pK}_{\mathrm{a},1} + \log\left(\frac{\mathrm{a}_{\mathrm{AcO^-}}\mathrm{a}_{\mathrm{CO_2}}\mathrm{a}_{\mathrm{H_2O}}}{\mathrm{a}_{\mathrm{AcOH}}\mathrm{a}_{\mathrm{HCO_3^-}}}\right)$$

For this calculation, we assume that the analytical concentrations of species are equal to their activities and that the analytical concentration of H_2O is the sum of the adventitious concentration and the 1 M added water. The concentration of CO_2 was estimated via quantitative ^{13}C NMR spectroscopy at 1 atm, and the value is divided by two because the equilibrium measurements were conducted under 0.5 atm P_{CO2}. Thus, using the derived expression, we calculate the pK_a of the CO_2/HCO_3^- equilibrium in DMSO to be 13.0.

$$\mathrm{p}K^*_{a,2} = \frac{-0.070\ \mathrm{V} + 0.096\ \mathrm{V}}{0.059\ \mathrm{V}} + 12.6 + \log\left(\frac{(0.150\ \mathrm{M})(0.076\ \mathrm{M})(1.009\ \mathrm{M})}{(0.150\ \mathrm{M})(0.076\ \mathrm{M})}\right)$$

$$\boldsymbol{\mathrm{p}K^*_{a,2} = 13.0}$$

We stress that this pK_a value is calculated from the concentration of CO_2 in the electrolyte rather than the partial pressure (via the Henry's law constant). We also stress that the calculated value is *only a rough estimate*: in addition to assuming that concentrations are equal to activities, it assumes that there are no other operative equilibrium processes (such as ion pairing or higher order homoconjugation) that would significantly affect the real pK_a value.

2.8. Supplementary Data

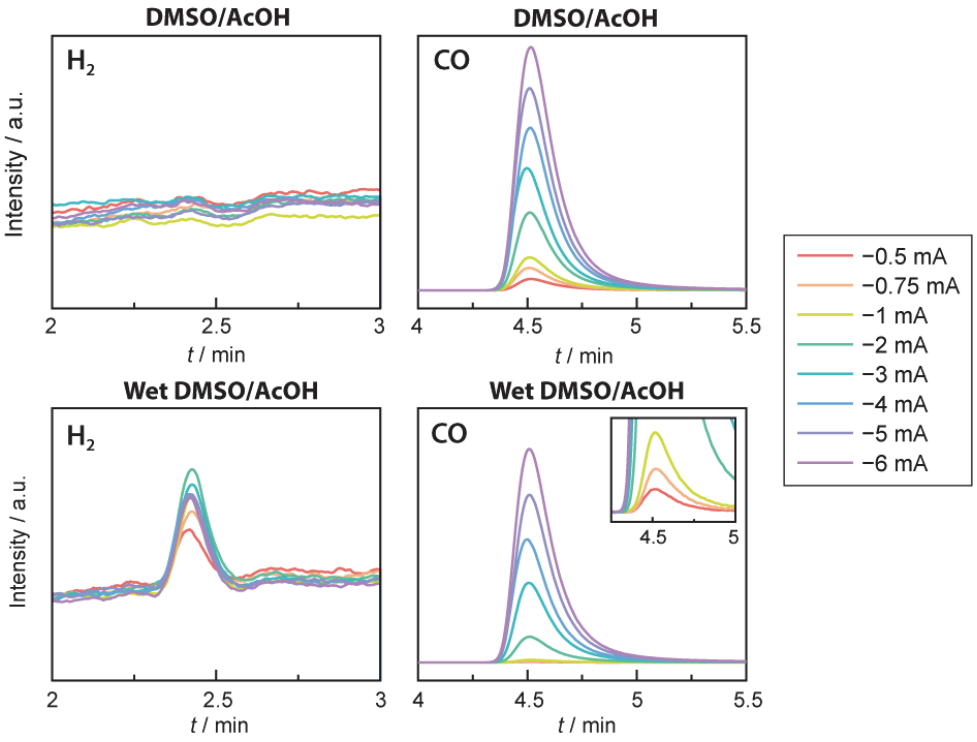

Figure S2.8. Gas chromatograms of signal intensity versus retention time for H_2 elution and CO elution recorded during in-line analysis of electrolysis in DMSO/AcOH and wet DMSO/AcOH at various applied currents. Each plot shown is representative of one of three triplicate data sets.

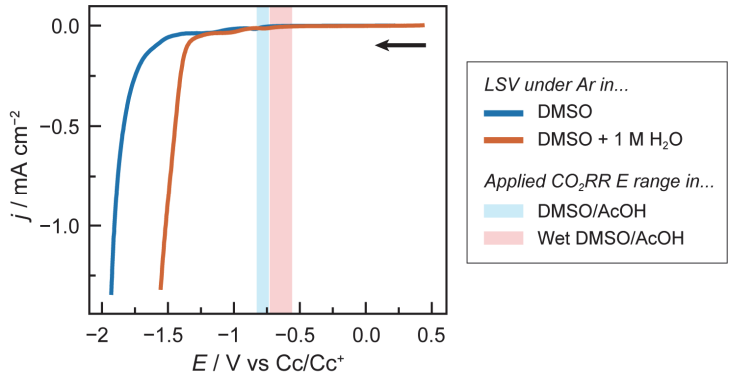

Figure S2.9. Linear sweep voltammograms of DMSO-based electrolyte solutions on pc-Au electrode under Ar atmosphere. Solutions consist of (blue) DMSO and 0.3 M $TBAPF_6$ and (orange) DMSO and 0.3 M $TBAPF_6$ with 1 M added water. The range of applied steady-state potentials for CO_2RR in (light blue stripe) DMSO/AcOH and (light red stripe) wet DMSO/AcOH are shown for comparison, based on the data in Figure 2. Scans were measured in the negative potential direction at 50 mV s^{-1} under stirring conditions as indicated by the black directional arrow. All potentials are referenced to the cobaltocene/cobaltocenium (Cc/Cc^+) redox couple, while current densities are normalized with respect to the electrochemically active surface area.

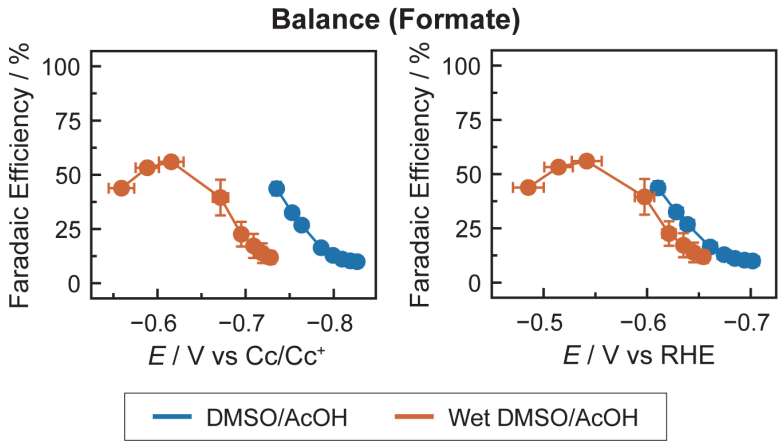

Figure S2.10. (a) Potential-dependent faradaic efficiency trends for the faradaic balance in DMSO/AcOH (blue) and DMSO/AcOH with 1 M added water ("wet DMSO/AcOH", orange) electrolyte versus the cobaltocene/cobaltocenium (Cc/Cc^+) internal reference potential (left) and RHE (reversible hydrogen electrode) reference potential (right). Electrolysis was conducted via galvanostatic polarization from –0.17 to –2.03 mA cm^{-2} on pc-Au catalyst. The faradaic balance was calculated from the remaining partial current after accounting for all gaseous reaction products and ascribed to formate production. All current densities are normalized with respect to the electrochemically active surface area. The data points and error bars correspond to the average and standard deviation of triplicate measurements; error bars not visible are smaller than the data points shown.

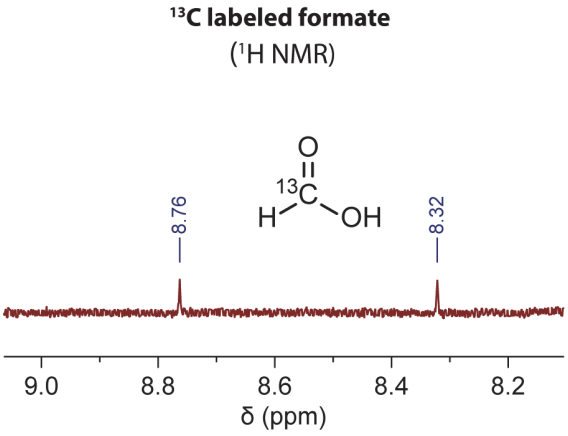

Figure S2.11. ^1H NMR spectra of ^{13}C labeled formate following electrolysis in $^{13}CO_2$ in DMSO/AcOH electrolyte.

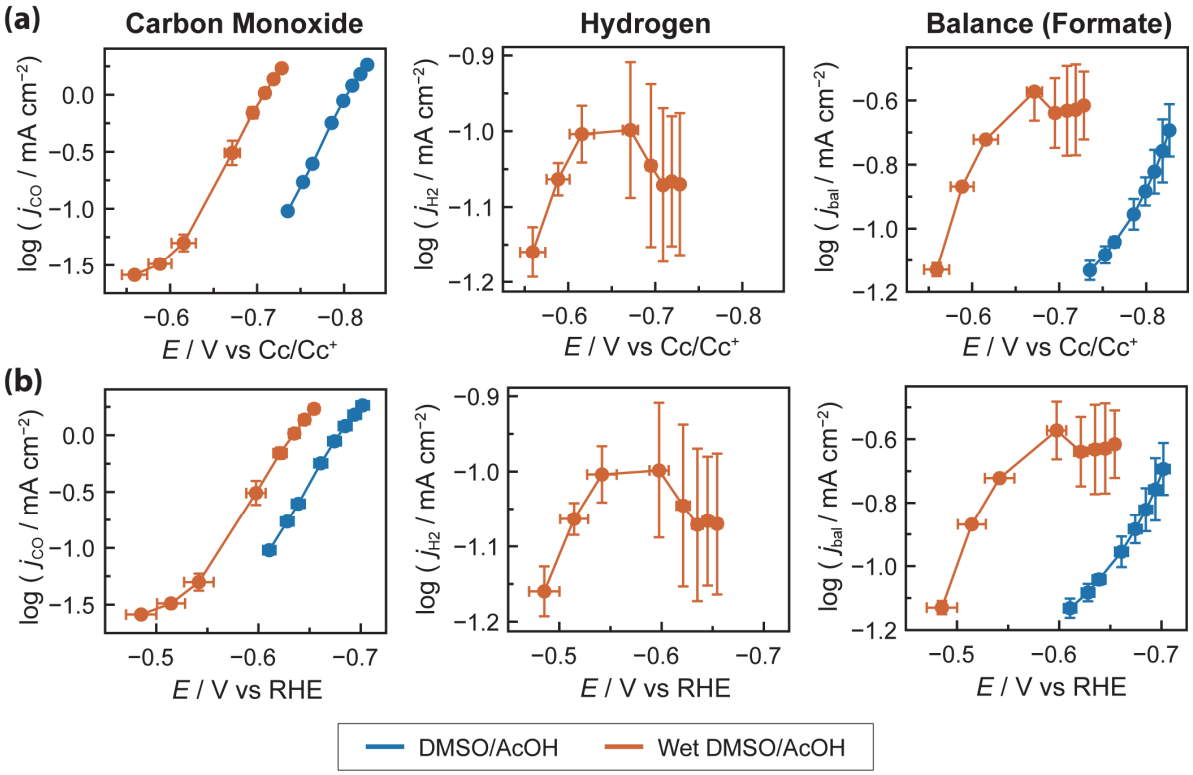

Figure S2.12. (a) Potential-dependent current trends for CO, H_2, and the faradaic balance in DMSO/AcOH (blue) and DMSO/AcOH with 1 M added water ("wet DMSO/AcOH", orange) electrolyte versus the (a) cobaltocene/cobaltocenium (Cc/Cc^+) internal reference potential and (b) RHE (reversible hydrogen electrode) reference potential. Electrolysis was conducted via galvanostatic polarization from –0.17 to –2.03 mA cm^{-2} on pc-Au catalyst. The faradaic balance was calculated as the remaining partial current after accounting for all gaseous reaction products and ascribed to formate production. All current densities are normalized with respect to the electrochemically active surface area. The data points and error bars correspond to the average and standard deviation of triplicate measurements; error bars not visible are smaller than the data points shown.

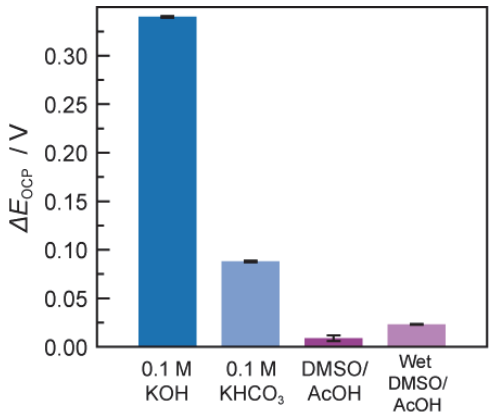

Figure S2.13. Difference in the measured equilibrium potential of the H^+/H_2 redox couple in 0.1 M KOH (blue), 0.1 M $KHCO_3$ (light blue), DMSO/AcOH (purple) and wet DMSO/AcOH (light purple) electrolytes before and after exposure to 0.5 atm Ar and 0.5 atm CO_2. In both conditions, 0.5 atm H_2 was present to maintain Nernstian equilibrium. The data points and error bars correspond to the average and standard deviation of triplicate measurements.

2.9. References

(1) Overa, S.; Ko, B. H.; Zhao, Y.; Jiao, F. Electrochemical Approaches for CO_2 Conversion to Chemicals: A Journey toward Practical Applications. *Acc Chem Res* **2022**, *55* (5), 638–648.

(2) Shih, C. F.; Zhang, T.; Li, J.; Bai, C. Powering the Future with Liquid Sunshine. *Joule* **2018**, *2* (10), 1925–1949.

(3) Nitopi, S.; Bertheussen, E.; Scott, S. B.; Liu, X.; Engstfeld, A. K.; Horch, S.; Seger, B.; Stephens, I. E. L.; Chan, K.; Hahn, C.; Nørskov, J. K.; Jaramillo, T. F.; Chorkendorff, I. Progress and Perspectives of Electrochemical CO_2 Reduction on Copper in Aqueous Electrolyte. *Chem Rev* **2019**, *119* (12), 7610–7672.

(4) Wuttig, A.; Yaguchi, M.; Motobayashi, K.; Osawa, M.; Surendranath, Y. Inhibited Proton Transfer Enhances Au-Catalyzed CO_2-to-Fuels Selectivity. *Proceedings of the National Academy of Sciences* **2016**, *113* (32), E4585–E4593.

(5) Yoon, Y.; Hall, A. S.; Surendranath, Y. Tuning of Silver Catalyst Mesostructure Promotes Selective Carbon Dioxide Conversion into Fuels. *Angewandte Chemie International Edition* **2016**, *55* (49), 15282–15286.

(6) Hall, A. S.; Yoon, Y.; Wuttig, A.; Surendranath, Y. Mesostructure-Induced Selectivity in CO_2 Reduction Catalysis. *J Am Chem Soc* **2015**, *137* (47), 14834–14837.

(7) Raciti, D.; Mao, M.; Park, J. H.; Wang, C. Local pH Effect in the CO_2 Reduction Reaction on High-Surface-Area Copper Electrocatalysts. *J Electrochem Soc* **2018**, *165* (10), F799–F804.

(8) Lu, X.; Zhu, C.; Wu, Z.; Xuan, J.; Francisco, J. S.; Wang, H. In Situ Observation of the pH Gradient near the Gas Diffusion Electrode of CO_2 Reduction in Alkaline Electrolyte. *J Am Chem Soc* **2020**, *142* (36), 15438–15444.

(9) Rabinowitz, J. A.; Kanan, M. W. The Future of Low-Temperature Carbon Dioxide Electrolysis Depends on Solving One Basic Problem. *Nat Commun* **2020**, *11* (1), 5231.

(10) Ma, M.; Clark, E. L.; Therkildsen, K. T.; Dalsgaard, S.; Chorkendorff, I.; Seger, B. Insights into the Carbon Balance for CO_2 Electroreduction on Cu Using Gas Diffusion Electrode Reactor Designs. *Energy Environ Sci* **2020**, *13* (3), 977–985.

(11) Dunwell, M.; Lu, Q.; Heyes, J. M.; Rosen, J.; Chen, J. G.; Yan, Y.; Jiao, F.; Xu, B. The Central Role of Bicarbonate in the Electrochemical Reduction of Carbon Dioxide on Gold. *J Am Chem Soc* **2017**, *139* (10), 3774–3783.

(12) Wuttig, A.; Yoon, Y.; Ryu, J.; Surendranath, Y. Bicarbonate Is Not a General Acid in Au-Catalyzed CO_2 Electroreduction. *J Am Chem Soc* **2017**, *139* (47), 17109–17113.

(13) Hori, Y. Electrochemical CO_2 Reduction on Metal Electrodes. In *Modern Aspects of Electrochemistry*; Springer New York: New York, NY; pp 89–189.

(14) Huang, J. E.; Li, F.; Ozden, A.; Sedighian Rasouli, A.; García de Arquer, F. P.; Liu, S.; Zhang, S.; Luo, M.; Wang, X.; Lum, Y.; Xu, Y.; Bertens, K.; Miao, R. K.; Dinh, C.-T.; Sinton, D.; Sargent, E. H. CO_2 Electrolysis to Multicarbon Products in Strong Acid. *Science (1979)* **2021**, *372* (6546), 1074–1078.

(15) O'Brien, C. P.; Miao, R. K.; Liu, S.; Xu, Y.; Lee, G.; Robb, A.; Huang, J. E.; Xie, K.; Bertens, K.; Gabardo, C. M.; Edwards, J. P.; Dinh, C.-T.; Sargent, E. H.; Sinton, D. Single Pass CO_2 Conversion Exceeding 85% in the Electrosynthesis of Multicarbon Products via Local CO_2 Regeneration. *ACS Energy Lett* **2021**, *6* (8), 2952–2959.

(16) Pan, B.; Fan, J.; Zhang, J.; Luo, Y.; Shen, C.; Wang, C.; Wang, Y.; Li, Y. Close to 90% Single-Pass Conversion Efficiency for CO_2 Electroreduction in an Acid-Fed Membrane Electrode Assembly. *ACS Energy Lett* **2022**, *7* (12), 4224–4231.

(17) Gu, J.; Liu, S.; Ni, W.; Ren, W.; Haussener, S.; Hu, X. Modulating Electric Field Distribution by Alkali Cations for CO_2 Electroreduction in Strongly Acidic Medium. *Nat Catal* **2022**, *5* (4), 268–276.

(18) Xie, K.; Miao, R. K.; Ozden, A.; Liu, S.; Chen, Z.; Dinh, C.-T.; Huang, J. E.; Xu, Q.; Gabardo, C. M.; Lee, G.; Edwards, J. P.; O'Brien, C. P.; Boettcher, S. W.; Sinton, D.; Sargent, E. H. Bipolar Membrane Electrolyzers Enable High Single-Pass CO_2 Electroreduction to Multicarbon Products. *Nat Commun* **2022**, *13* (1), 3609.

(19) Yang, K.; Li, M.; Subramanian, S.; Blommaert, M. A.; Smith, W. A.; Burdyny, T. Cation-Driven Increases of CO_2 Utilization in a Bipolar Membrane Electrode Assembly for CO_2 Electrolysis. *ACS Energy Lett* **2021**, *6* (12), 4291–4298.

(20) García de Arquer, F. P.; Dinh, C.-T.; Ozden, A.; Wicks, J.; McCallum, C.; Kirmani, A. R.; Nam, D.-H.; Gabardo, C.; Seifitokaldani, A.; Wang, X.; Li, Y. C.; Li, F.; Edwards, J.; Richter, L. J.;

Thorpe, S. J.; Sinton, D.; Sargent, E. H. CO_2 Electrolysis to Multicarbon Products at Activities Greater than 1 A cm^{-2}. *Science (1979)* **2020**, *367* (6478), 661–666.

(21) König, M.; Vaes, J.; Klemm, E.; Pant, D. Solvents and Supporting Electrolytes in the Electrocatalytic Reduction of CO_2. *iScience* **2019**, *19*, 135–160.

(22) Joshi, P. B.; Karki, N.; Wilson, A. J. Electrocatalytic CO_2 Reduction in Acetonitrile Enhanced by the Local Environment and Mass Transport of H_2O. *ACS Energy Lett* **2022**, *7* (2), 602–609.

(23) Haynes, L. V; Sawyer, D. T. Electrochemistry of Carbon Dioxide in Dimethyl Sulfoxide at Gold and Mercury Electrodes. *Anal Chem* **1967**, *39* (3), 332–338.

(24) Ito, K.; Ikeda, S.; Yamauchi, N.; Iida, T.; Takagi, T. Electrochemical Reduction Products of Carbon Dioxide at Some Metallic Electrodes in Nonaqueous Electrolytes. *Bull Chem Soc Jpn* **1985**, *58* (10), 3027–3028.

(25) Shi, J.; Shen, F.; Shi, F.; Song, N.; Jia, Y.-J.; Hu, Y.-Q.; Li, Q.-Y.; Liu, J.; Chen, T.-Y.; Dai, Y.-N. Electrochemical Reduction of CO_2 into CO in Tetrabutylammonium Perchlorate/Propylene Carbonate: Water Effects and Mechanism. *Electrochim Acta* **2017**, *240*, 114–121.

(26) Figueiredo, M. C.; Ledezma-Yanez, I.; Koper, M. T. M. In Situ Spectroscopic Study of CO_2 Electroreduction at Copper Electrodes in Acetonitrile. *ACS Catal* **2016**, *6* (4), 2382–2392.

(27) Vijh, A. K.; Conway, B. E. Electrode Kinetic Aspects of the Kolbe Reaction. *Chem Rev* **1967**, *67* (6), 623–664.

(28) Izutsu, K. *Electrochemistry in Nonaqueous Solutions*; Wiley, 2009.

(29) Roberts, J. A. S.; Bullock, R. M. Direct Determination of Equilibrium Potentials for Hydrogen Oxidation/Production by Open Circuit Potential Measurements in Acetonitrile. *Inorg Chem* **2013**, *52* (7), 3823–3835.

(30) Chu, A. T.; Surendranath, Y. Aprotic Solvent Exposes an Altered Mechanism for Copper-Catalyzed Ethylene Electrosynthesis. *J Am Chem Soc* **2022**, *144* (12), 5359–5365.

(31) Ringe, S.; Morales-Guio, C. G.; Chen, L. D.; Fields, M.; Jaramillo, T. F.; Hahn, C.; Chan, K. Double Layer Charging Driven Carbon Dioxide Adsorption Limits the Rate of Electrochemical Carbon Dioxide Reduction on Gold. *Nat Commun* **2020**, *11* (1), 33.

(32) Zhang, Y.; Chong, J. Y.; Xu, R.; Wang, R. Effective Separation of Water-DMSO through Solvent Resistant Membrane Distillation (SR-MD). *Water Res* **2021**, *197*, 117103.

(33) Hasegawa, Y.; Abe, C.; Ikeda, A. Pervaporative Dehydration of Organic Solvents Using High-Silica CHA-Type Zeolite Membrane. *Membranes (Basel)* **2021**, *11* (3), 229.

(34) Amatore, C.; Saveant, J. M. Mechanism and Kinetic Characteristics of the Electrochemical Reduction of Carbon Dioxide in Media of Low Proton Availability. *J Am Chem Soc* **1981**, *103* (17), 5021–5023.

(35) Dinh, C.-T.; Burdyny, T.; Kibria, M. G.; Seifitokaldani, A.; Gabardo, C. M.; García de Arquer, F. P.; Kiani, A.; Edwards, J. P.; De Luna, P.; Bushuyev, O. S.; Zou, C.; Quintero-Bermudez, R.; Pang, Y.; Sinton, D.; Sargent, E. H. CO_2 Electroreduction to Ethylene via Hydroxide-Mediated Copper Catalysis at an Abrupt Interface. *Science (1979)* **2018**, *360* (6390), 783–787.

(36) Dinh, C.-T.; García de Arquer, F. P.; Sinton, D.; Sargent, E. H. High Rate, Selective, and Stable Electroreduction of CO_2 to CO in Basic and Neutral Media. *ACS Energy Lett* **2018**, *3* (11), 2835–2840.

(37) Schreier, M.; Yoon, Y.; Jackson, M. N.; Surendranath, Y. Competition between H and CO for Active Sites Governs Copper-Mediated Electrosynthesis of Hydrocarbon Fuels. *Angewandte Chemie International Edition* **2018**, *57* (32), 10221–10225.

(38) Yoon, Y.; Yan, B.; Surendranath, Y. Suppressing Ion Transfer Enables Versatile Measurements of Electrochemical Surface Area for Intrinsic Activity Comparisons. *J Am Chem Soc* **2018**, *140* (7), 2397–2400.

Chapter 3

Aprotic Solvent Exposes an Altered Mechanism for Copper-Catalyzed Ethylene Electrosynthesis

Adapted and reprinted with permission from Chu, A. T.; Surendranath, Y. Aprotic Solvent Exposes an Altered Mechanism for Copper-Catalyzed Ethylene Electrosynthesis. *J. Am. Chem. Soc.* **2022**, *144* (12), 5359–5365.

3.1. Introduction

The electrochemical reductions of CO_2 (CO_2RR) and CO (CORR) to hydrocarbons are both attractive routes for the production of renewable fuels and materials from electrical energy input.[1,2] This electrochemical transformation is known to occur on copper-based catalysts, which generate a wide array of C_{2+} hydrocarbons and oxygenates.[3–6] Changes to the Cu morphology[3,7] and electrode structure to enhance gas delivery[8,9] have been extensively employed to augment reaction selectivity. However, despite these advances, most electrodes still give rise to wide product distributions. A molecular-level mechanistic understanding of how to engender the efficient and selective formation of desirable C_2 products in either process remains elusive.

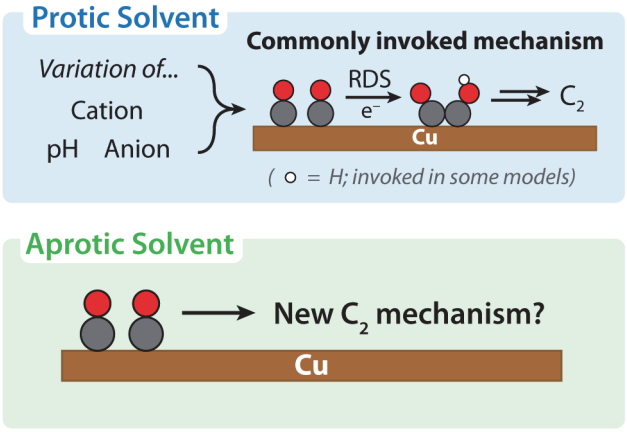

Figure 3.1. (Top) A commonly invoked mechanism for ethylene formation from CO on polycrystalline Cu has been found to be insensitive to variation in pH, cation, or anion. (Bottom) We postulated that an aprotic solvent environment would expose new mechanistic landscapes for C_2 production formation.

Reaction selectivity in Cu-catalyzed CO_2RR and CORR is highly sensitive to the composition of aqueous electrolytes. In particular, increased alkalinity at the interface[10–14] and the introduction of heavier alkali cations[15,16] have been found to result in increased C_2 selectivity. While the role of the cation remains a topic of recent debate, the alkalinity effect has been shown to enhance C_2 selectivity by suppressing the

rate of competing C_1 and hydrogen evolution reaction (HER) pathways. However, despite exhaustive studies of both effects, these strategies have not been found to fundamentally alter the electrokinetic profile of C_2 formation itself. Indeed, across all electrolyte conditions examined, C_2 product formation displays high Tafel slopes ($\geq$119 mV dec^{-1}) and its rate has been found to be insensitive to the pH or buffer composition.[14,17] Both CO_2 and CO reductions have also been found to proceed via a common adsorbed carbon monoxide (*CO) intermediate.[3] These observations have led to a consensus mechanistic model for C_2 product formation that invokes rate-determining C–C bond formation via coupling of *CO with concomitant electron transfer (ET) and, possibly, proton transfer (PT) from water (**Figure 3.1**, top).[4,14,18–20] This mechanistic mode is invoked even in a protic nonaqueous medium such as ethanol, which displays a nominally similar product distribution.[21] Despite enormous efforts devoted to the design of aqueous electrolytes, this dominant mechanistic paradigm remains largely unchanged, limiting the parameter space available to tune aqueous reaction selectivity and efficiency.

Notably, all prior reports of Cu-catalyzed CO_2RR or CORR to higher-order products that share this mechanistic model employ protic electrolytes. The putative *CO dimer formed at the transition state carries partial oxoanion character, and thus hydrogen-bonding interactions with a protic solvent would be expected to lower the transition-state energy. By removing these interactions in an aprotic solvent, we hypothesized that we could access alternative mechanistic pathways for C–C bond formation involving direct proton-coupled electron transfer (PCET) to otherwise inaccessible surface intermediates (**Figure 3.1**, bottom). Additionally, in an aprotic medium, the thermochemistry and kinetics of PCET can be unambiguously controlled from an exogenous donor rather than from the solvent itself.

Despite the potential promise of this approach, Cu-catalyzed higher-order hydrocarbon formation in aprotic solvent-based electrolytes has not been systematically developed.[22–24] Designing an aprotic system suited to Cu-catalyzed hydrocarbon electrosynthesis requires a careful balance of electrolyte properties. The electrolyte must possess high ionic conductivity, chemical stability under highly negative electrode potentials, and compatibility with the strong bases and nucleophiles generated from PCET steps. In addition to all of these criteria, the proton donor environment must be chosen carefully. A donor environment that is too acidic is expected to drive exclusive hydrogen production, whereas a donor environment that is too basic may disfavor the PCET pathways needed for hydrocarbon formation in favor of pathways independent of proton transfer. Indeed, a previous study of Cu-catalyzed CO_2RR in acetonitrile employed water, a particularly poor proton donor in polar aprotic solvent-based electrolytes (e.g., pK_a = 31.4 in dimethyl sulfoxide, DMSO)[25] and, consequently, only observed carbon monoxide, carbonate, and oxalate as principal products, all of which do not contain hydrogens.[23] Hence, we envisioned that the careful selection of a

proton donor with an intermediate pK_a could expose alternative pathways for hydrocarbon formation in aprotic solvents.

Herein, we investigate hydrocarbon electrosynthesis in an aprotic solvent for CORR on a model polycrystalline Cu (pc-Cu) catalyst. We use CO as the input to isolate and contrast the mechanistic steps leading to C–C-coupled products with that of reported CORR kinetics in water. Specifically, we find that in DMSO solvent with a phenol/phenoxide ($PhOH/PhO^-$) proton donor environment, pc-Cu mediates the exclusive reduction of CO to C_2 products with modest competing H_2 formation. We observe a low Tafel slope (27 ± 1 mV dec^{-1}) and Nernstian dependence on proton activity for ethylene formation. This electrokinetic profile contrasts with ethylene formation catalysis in water, which displays high Tafel slopes and is independent of proton activity on the standard hydrogen electrode (SHE) scale. These findings highlight the opportunity afforded by proton donor control in aprotic media to steer C_2 reaction pathways into new mechanistic regimes.

3.2. Cu-Catalyzed CO Reduction in DMSO/PhOH Selects for C_2 Products

To probe the product landscape of CO reduction catalysis in aprotic solvent-based electrolytes, we polarized pc-Cu in DMSO in the presence of phenol/phenoxide buffer as the proton donor environment and with tetrabutylammonium hexafluorophosphate ($TBAPF_6$) as the supporting electrolyte. Even though highly nano/mesostructured materials are commonly employed in contemporary aqueous CORR, we deliberately selected simple planar pc-Cu for this study to allow for meaningful comparison to the rich body of mechanistic work on pc-Cu in water.[17,18,26] In addition, the nominally planar structure of this catalyst minimizes convolution from transport artifacts, allowing us to extract activation-controlled kinetics. To minimize convolution from proton donor consumption over the course of the electrolysis, we conducted electrolyses to a maximal proton donor consumption of 10%. Product gases were quantified using in-line gas chromatography (GC) (see section 3.6.3 for full details). Reactions were conducted using varying analytical phenol/phenoxide buffer strengths ($C_{A,0}$) ranging from 330 to 1330 mM, with an analytical ratio of phenol ($C_{HA,0}$) to phenoxide ($C_{A-,0}$) of 4:1. In every condition, the total ionic strength was held constant by the addition of $TBAPF_6$. The anodic half-reaction was assigned to be the oxidation of phenoxide to phenoxy radical; this product is isolated to the anode compartment, as confirmed by the UV–vis analysis of the catholyte after electrolysis (**Figure S3.2**; see section 3.7.1 for a detailed discussion). Phenol was identified as the thermochemically operative donor, as opposed to trace water, as determined from linear sweep voltammetry under an inert atmosphere (**Figure S3.3**; see section 3.7.2 for a detailed discussion). Using this protocol, we are able to observe sustained CO reduction catalysis with minimal convolution from depletion of the phenol proton donor.

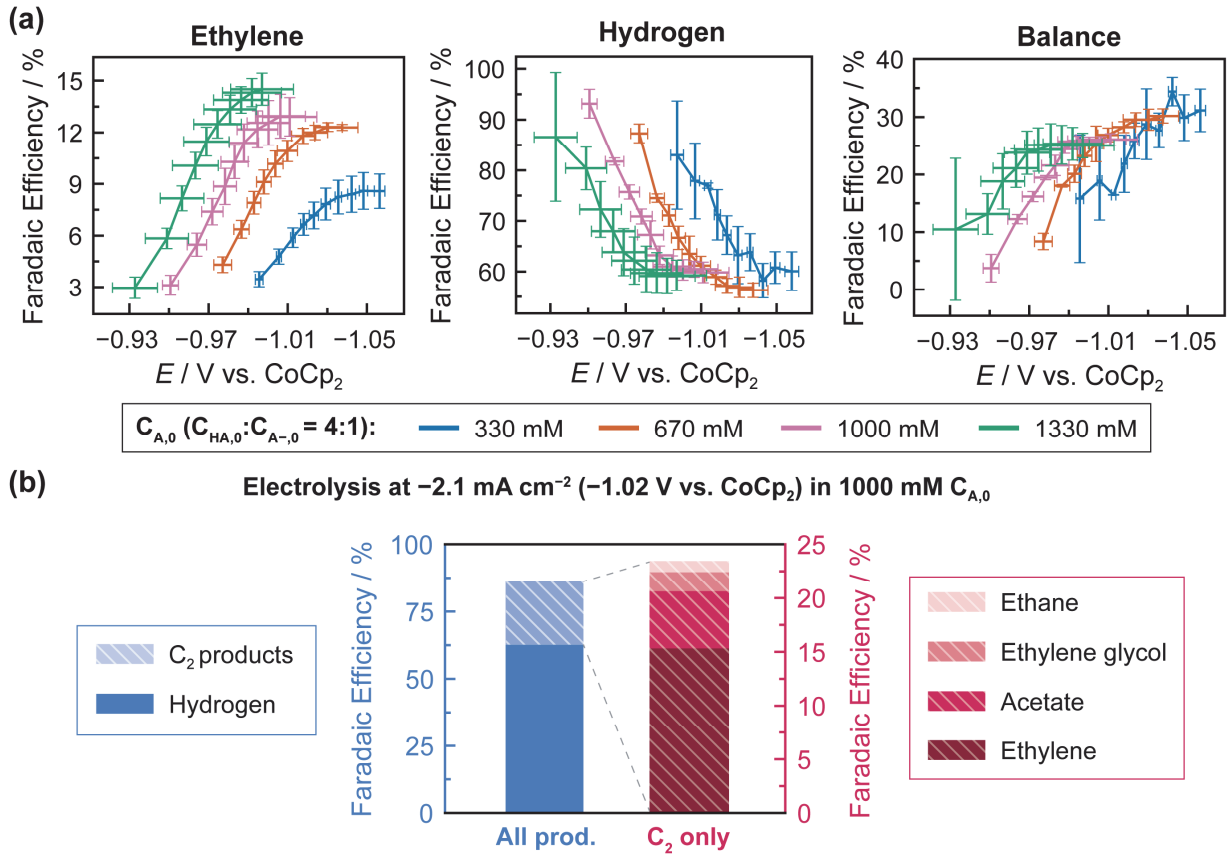

Figure 3.2. (a) Potential-dependent faradaic efficiency trends for ethylene, hydrogen, and the faradaic balance in the DMSO/TBAPF$_6$ electrolyte collected under various analytical PhOH/PhO$^-$ buffer strengths ($C_{A,0}$) with a 4:1 analytical ratio of PhOH ($C_{HA,0}$) and TBAPhO ($C_{A-,0}$). Experiments were conducted via steady-state galvanostatic polarization from −0.26 to −2.6 mA cm^{-2} applied current on pc-Cu catalyst. The faradaic balance was taken to be the remaining current after accounting for the total balance of all gaseous reaction products. All potentials are referenced to the cobaltocenium (CoCp$_2$) redox couple. All current densities are normalized with respect to the electrochemically active surface area. The data points and error bars correspond to the average and standard deviations of at least two or more independent measurements. (b) Faradaic efficiency of all detected products following bulk electrolysis at −2.1 mA cm^{-2} (−1.02 V vs CoCp$_2$) in 1000 mM $C_{A,0}$ buffer.

Ethylene and hydrogen were observed as the most abundant gaseous reaction products (**Figure 3.2a**, left and middle), with identical trends across all buffer strengths. Ethane and methane were detected in trace amounts (**Figure S3.5**); thus, they were not analyzed mechanistically. The product distribution shifts from hydrogen gas to carbon products with increasingly negative potentials, with faradaic efficiencies (FE) for ethylene increasing to 15% FE in the presence of 1330 mM buffer. The remaining faradaic balance (**Figure 2a**, right) was further investigated by analyzing the electrolyte for liquid-phase products. To produce them in bulk, galvanostatic electrolysis was conducted at −2.1 mA cm^{-2} (−1.02 V vs CoCp$_2$) using ^{13}CO with 1000 mM buffer, followed by estimation of the faradaic balance via ^{13}C NMR quantification (see section 3.6.7 for details). Ethylene glycol was detected with a faradaic efficiency of 1.8%, while acetate was detected with a faradic efficiency of 5.3% (**Figure 3.2b**). While there remain a minority fraction of products

that are unaccounted for, we stress that the observed hydrogen and carbon products account for the majority of the charge passed (gaseous FE = 79%, total FE = 86%). Strikingly, given the trace level of methane in this system (FE = 0.23%), the DMSO/PhOH electrolyte appears to foster an exceptionally high C_2-to-C_1 product ratio of over ∼9000, substantially higher than that documented in water (∼1–3) for CORR on pc-Cu catalysts.[17]

Importantly, the NMR spectral signals all originate from the ^{13}C label, demonstrating that the carbons of ethylene glycol and acetate are sourced from CO rather than from the adventitious decomposition of the electrolyte (**Figure S3.6**). To confirm that ethylene is also sourced from the introduced CO, the effluent gas stream exiting the electrochemical cell was cryogenically frozen into a gas-tight NMR tube under liquid Ar (ca. −186 °C; see section 3.6.7 for full methodological details). The ^{1}H NMR spectrum of the resultant sample shows a doublet centered at 5.4 ppm, characteristic of ^{13}C-ethylene with an enriched carbon dyad (**Figure S3.7**). Together, the data demonstrate that pc-Cu is capable of catalyzing CO reduction to C_2 products, with only the trace formation of C_1 products in the DMSO/PhOH electrolyte.

3.3. Ethylene Formation Displays Quasi-Equilibrium Electron-Transfer Kinetics

Kinetic measurements under varying buffer strengths reveal a unique electrokinetic profile for ethylene formation. **Figure 3.3** plots the logarithm of the partial current density for ethylene formation vs potential for four different buffer strengths. The data show linearity in the low-current-density regime (**Figure 3.3**, dashed lines), followed by curvature at higher current densities. Rotating cylinder experiments establish that transport artifacts negligibly convolute the data in the low-current-density regime. Even for the lowest buffer strength (330 mM), which would be expected to display the highest level of transport convolution, ethylene current densities remain nominally unchanged within error between a stationary electrode and one rotated at 1600 rpm (**Figure S3.4**). An important mechanistic diagnostic parameter that can be extracted from these data is the Tafel slope. This value, defined as the partial derivative of the potential with respect to the logarithm of the current density, is obtained by taking the reciprocal of the raw slope values of the dashed lines in **Figure 3.3**. To minimize convolution from transport limitations, the Tafel slope for each condition was determined using only the lowest five applied currents. Additionally, across the range of conditions sampled in this study, ethylene formation occurs at overpotentials in excess of 0.9 V (see section 3.7.4 for a detailed discussion), excluding convolution to the current density from the reverse reaction.

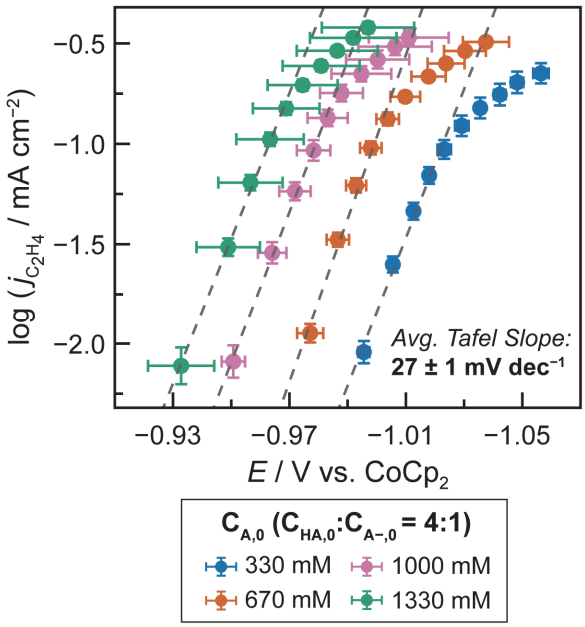

Figure 3.3. Current density vs potential (Tafel) plots for ethylene formation as a function of the analytical PhOH/PhO$^-$ buffer strength ($C_{A,0}$) in the DMSO/TBAPF$_6$ electrolyte, with a 4:1 analytical ratio of PhOH ($C_{HA,0}$) to TBAPhO ($C_{A-,0}$). Experiments were conducted via steady-state galvanostatic polarization from −0.26 to −2.6 mA cm^{-2} applied current on pc-Cu catalyst. All potentials are referenced to the cobaltocenium ($CoCp_2$) redox couple. All current densities are normalized with respect to the electrochemically active surface area. The Tafel slope for each condition was calculated from a linear fit to the lowest five applied currents. The data points and error bars correspond to the average of at least two independent measurements.

The Tafel data for ethylene formation suggest a distinct C_2 reaction manifold compared to aqueous electrolytes. The Tafel slope for ethylene formation was measured to be 27 ± 1 mV dec^{-1} (**Figure 3.3**), while that of hydrogen evolution was 53 ± 8 mV dec^{-1} (**Figure S3.5**). Importantly, the Tafel slopes are independent of the buffer strength, suggesting that the reaction mechanism is conserved across all conditions. Unlike in water, where the ethylene formation Tafel slope is reported to be similar or larger than that of hydrogen evolution,[14,20] we observed the opposite here. The consequence of this is shown in **Figure 3.2a**, where selectivity for ethylene increases and hydrogen decreases with more negative applied potentials in the regime sampled for Tafel analysis. Furthermore, the low Tafel slope in DMSO/PhOH implies an altered mechanism. In water, a ca. 119 mV dec^{-1} Tafel slope commonly observed for ethylene formation has been attributed to a mechanistic pathway involving a single irreversible electron transfer at the rate-determining step.[3,14] In this DMSO/PhOH system, the dramatically lower 27 ± 1 mV dec^{-1} slope implies the involvement of quasi-equilibrium ET events prior to the rate-limiting step. We stress that the exact mechanistic interpretation of this low Tafel slope requires knowledge of the isotherm of surface intermediates and is highly sensitive to small deviations in the slope value. Nonetheless, in the limit of Langmuirian adsorption, a mechanism involving at least two reversible ET events would be consistent with

the observed Tafel data. The foregoing discussion highlights that the kinetic profiles of electron exchange toward ethylene formation in the DMSO/PhOH are vastly distinct from that in aqueous environments.

3.4. Ethylene Formation Displays Quasi-Equilibrium Proton-Transfer Kinetics

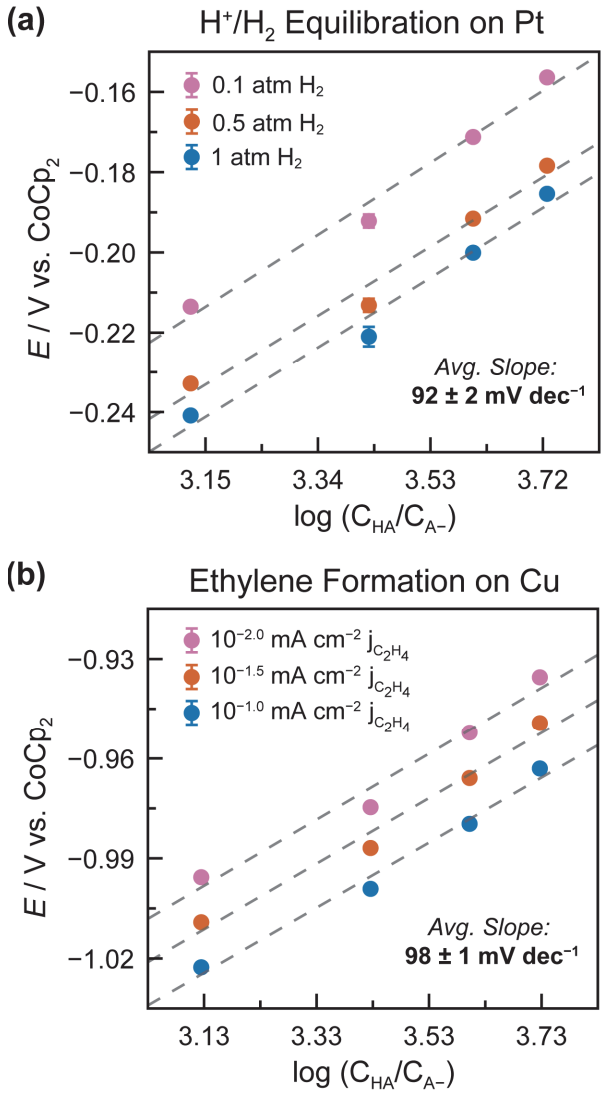

Figure 3.4. (a) Equilibrium potential of a Pt electrode equilibrated to the H^+/H_2 reaction as a function of the C_{HA}/C_{A^-} ratio as calculated from the PhOH/PhO^- homoconjugation constant in DMSO. The colors denote varying partial pressures of H_2 (P_{H2}). (b) Steady-state reaction potential for ethylene formation on pc-Cu as a function of C_{HA}/C_{A^-} ratios calculated from the PhOH/PhO^- homoconjugation constant in DMSO. The colors denote varying partial current densities for ethylene formation. All potentials are referenced to the cobaltocenium ($CoCp_2$) redox couple. The data points and error bars correspond to the average of triplicate independent measurements; error bars not visible are smaller than the data points shown.

Kinetic measurements under varying buffer strengths suggest that the reaction also displays a distinct dependence on the proton donor environment. In water, CO reduction to ethylene in aqueous media has been found to be insensitive to the proton donor environment or pH.[17,18] In contrast, we found that ethylene

formation shifts to more positive potentials with increasing analytical buffer strength (**Figure 3.3**), suggesting that the reaction has an explicit dependence on the proton donor environment.

The buffer dependence on the proton donor environment can be a consequence of proton-transfer thermodynamics, kinetics, or both. To discriminate these possibilities, we first need an understanding of how the proton activity changes over the range of buffer conditions examined in **Figure 3.3**. In water, the proton activity scales with the logarithm of the ratio of initial acid ($C_{HA,0}$) and conjugate base ($C_{A^-,0}$) concentrations, as described by the Henderson–Hasselbalch equation. In an aprotic media, many acids and conjugate bases form H-bonded homoconjugate dimers that serve to alter the free acid and conjugate base concentrations from their initial values.[27] For DMSO and phenol/phenoxide, the known homoconjugation constants were used to calculate the ratio of free phenol (C_{HA}) and free phenoxide (C_{A^-}) concentrations across the conditions examined (see section 3.7.5 for a detailed discussion).[28]

To determine how this acid–base ratio affects proton activity, we measured the equilibrium potential of the H^+/H_2 redox couple on Pt electrodes (see section 3.6.9 for methodological details)[29] across the range of buffer concentrations used for catalysis. Since the equilibrium potentials of PCET reactions depend on HA/A^- activities, not concentrations, the equilibrated potential of the H^+/H_2 redox couple provides an *in situ* measurement of proton activity. To first establish that H^+/H_2 is in rapid reversible equilibrium in the DMSO/PhOH electrolyte, the open-circuit potential (OCP) was measured as a function of hydrogen partial pressure (P_{H2}) on Pt electrodes under the four buffer conditions used in this study (**Figure S3.9**). The observation of a 29 ± 1 mV dec^{-1} scaling in P_{H2} is consistent with the expected pressure dependence of the two electrons per one H_2 molecule stoichiometry of the H_2/H^+ reaction, indicating that this approach is effective for measuring the equilibrium potential in this particular medium. A plot of E_{OCP} vs the logarithm of the ratio of C_{HA} and C_{A^-} across multiple values of P_{H2} displays a slope of 92 ± 2 mV dec^{-1} (**Figure 3.4a**). This value is greater than 59 mV dec^{-1} slope expected for the proton activity scaling of the H_2/H^+ equilibrium reaction. This implies that proton activity is not simply set by the calculated ratio of C_{HA} and C_{A^-} but also includes contributions from additional nonidealities such as ion pairing or higher-order aggregation.[27]

While the solution nonidealities that contribute to the above scaling are not fully known, the foregoing method nonetheless provides a quantitative calibration curve with which to analyze the buffer dependence of ethylene formation. A plot of the ethylene reaction potential vs the logarithm of the ratio of C_{HA} and C_{A^-} reveals a linear trend with a slope of 98 ± 1 mV dec^{-1} (**Figure 3.4b**; see **Figure S3.10** for the analysis of hydrogen evolution); this linearity is preserved across a range of applied currents with a common slope value. Indeed, this value is in close agreement with the 92 ± 2 mV dec^{-1} scaling observed for H_2/H^+

equilibration (**Figure 3.4a**), implying that ethylene formation also proceeds via a mechanism involving quasi-equilibrated PT steps.

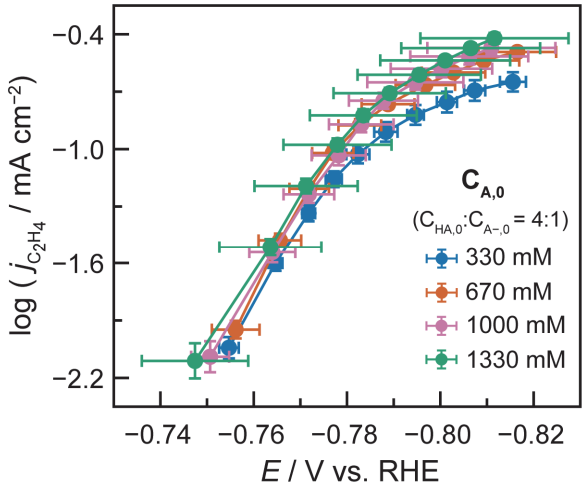

Figure 3.5. Ethylene partial current density vs potential (Tafel) plots on the reversible hydrogen electrode (RHE) scale. Ethylene Tafel plots are sampled as a function of the analytical PhOH/PhO$^-$ buffer strength ($C_{A,0}$) in the DMSO/TBAPF$_6$ electrolyte, with a 4:1 analytical ratio of PhOH ($C_{HA,0}$) to TBAPhO ($C_{A^-,0}$). All current densities are normalized with respect to the electrochemically active surface area. The data points and error bars in this plot were calculated using the equilibrium potential of H^+/H_2 from Figure 3.4a and applied potential from the polarization curves from Figure 3.3.

This donor dependence can be further understood by recalculating the potential of ethylene formation relative to the equilibrium potential for hydrogen evolution under each condition. This is analogous to replotting polarization data from the SHE to the reversible hydrogen electrode (RHE) reference scale in an aqueous system. **Figure 3.5** demonstrates that the polarization curves for ethylene formation collapse onto each other when represented in this manner, further demonstrating reversible dependence on the proton donor/acceptor activity of the medium (see **Figure S3.11** for the equivalent plot for hydrogen and **Figure S3.12** for ethylene and hydrogen faradaic efficiency trends plotted against RHE). This behavior is categorically distinct from the behavior observed in water, where ethylene formation is proton activity-independent on the SHE scale.[17] Furthermore, this result demonstrates that the potentials needed to achieve the highest rates of ethylene formation are −800 mV from RHE. At the same potential vs RHE in water, the rate of ethylene formation is comparable for CORR on pc-Cu but with a markedly higher selectivity for the competing hydrogen evolution reaction (ca. 90% in water, ca. 60% in DMSO/PhOH).[26]

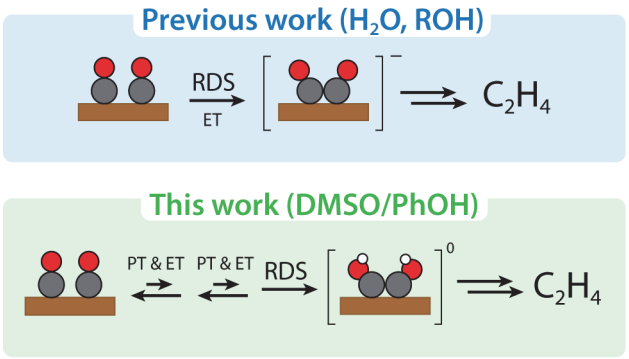

Figure 3.6. (Top) Consensus mechanistic model in protic electrolyte for electrochemical ethylene formation from CO on Cu catalysts. (Bottom) Proposed mechanistic model for PCET-mediated ethylene formation in DMSO/PhOH on Cu catalysts.

The foregoing analysis, taken together with the Tafel data, allows us to propose a mechanistic model for ethylene formation in DMSO/PhOH. The low Tafel slope is consistent with a mechanism for ethylene formation involving two quasi-equilibrated electron-transfer steps followed by a chemical rate-limiting step. The proton activity studies imply that both equilibrated ET steps are coupled to PT and that the chemical rate-limiting step is proton-independent. While many transition state structures could be consistent with these mechanistic features, we propose one possible structure, a neutral *HOCCOH species, that could result from the aggregate PCET and chemical steps (**Figure 3.6**). The lack of H-bonding in this solvent may favor neutral species of this type, relative to the oxyanionic *OCCO dimer invoked in water.[4,14,18,19]

3.5. Conclusions

In this study, we examine how an aprotic medium alters the mechanistic manifold of ethylene electrosynthesis. We find that pc-Cu catalyzes the reduction of CO to higher-order products in the DMSO/PhOH electrolyte. We observed ethylene, ethylene glycol, and acetate with negligible formation of C_1 products, thus demonstrating a high C_2/C_1 selectivity ratio for the reaction. Studies of the electrokinetic profile and its dependence on the proton donor environment suggest a mechanism for ethylene production that proceeds via multiple quasi-reversible proton- and electron-transfer events prior to a chemical rate-determining step. This new mechanism for ethylene production contrasts with the behavior in aqueous media, wherein ethylene formation is gated by a putative single irreversible electron transfer at the rate-determining step.[3] By engendering C_2 product formation with radical alterations to the reaction microenvironment, this work provides new insights into the role of interfacial solvation in directing proton- and electron-transfer steps in challenging bond activation reactions. These results are valuable benchmarks towards efforts to validate computational solvation models and their subsequent application in the calculation of reaction free-energy landscapes. Additionally, this work enables precise control of proton transfer to surface intermediates by varying the structure of the exogeneous proton donor. Altogether, these

findings provide new opportunities to rationally design interfacial environments for selective multi-electron, multi-proton catalysis.

3.6. Experimental Methods

3.6.1. Chemicals and materials

Unless stated otherwise, all chemical and cell components were handled using non-metallic instruments (spatula, vials, containers, etc.) to minimize trace metal contamination.

Used as received. The following chemicals were used as received; any chemicals or materials requiring additional preparation are described in their own subsection below. MilliQ water (Millipore Type 1, 18.2 MΩ cm) was used as the source of ultrapure water for all applications described below; dimethyl sulfoxide (DMSO, MilliporeSigma, 99.9999% purity by trace inorganic analysis); phenol (MilliporeSigma, ≥99%, unstabilized); diethyl ether (MilliporeSigma, for HPLC, >99.9%, inhibitor-free); tetrabutylammonium hydroxide (TBAOH) in methanol solution (Acros Organics, 40 wt.% in MeOH); tetrabutylammonium hexafluorophosphate ($TBAPF_6$, MilliporeSigma, >99.99% for electrochemical analysis); tetrabutylammonium bromide (MilliporeSigma, ≥99.0%); sulfuric acid (EMD Millipore, 95 − 98%); hydrogen peroxide (VWR, 30% w/w, stabilized); titanium wire (Alfa Aesar, 99.99%, 1 mm diameter); orthophosphoric acid (MilliporeSigma, 85% wt.%); cobaltocenium hexafluorophosphate ($CoCp_2$, MilliporeSigma, 98%); d^6-dimethylsulfoxide (d^6-DMSO, MilliporeSigma, 99.9 atom % D); 1,4-dioxane (MilliporeSigma, >=99.0%); d^1-chloroform ($CDCl_3$, Cambridge Isotope Laboratories, D, 99.8%); hydrogen gas (Airgas, Ultra High Purity); argon gas (Airgas, Ultra High Purity).

Preparation of carbon monoxide**.** Prior to usage, carbon monoxide (Airgas, Research Grade 4.0) or carbon-13 carbon monoxide (MilliporeSigma, ≤6 atom % 18O, ≥99 atom % 13C) was purified by passage through a moisture/oxygen filter (MilliporeSigma) followed by a custom-made CO filter to remove metal carbonyl impurities. The filter was constructed from a Cu tube filled with Cu turnings and wire heated to 275 °C with heating tape.

Safety precauation: *Carbon monoxide is a toxic and flammable gas. Storage, handling, and usage of carbon monoxide was conducted inside a well-ventilated hood to minimize inadvertent exposure. As an additional precaution, carbon monoxide alarms were installed inside the hood in the event of a failure, and all connections made to and from the gas cylinder were checked for leaks with a portable sensor.*

Preparation of pc-Cu working electrode. A polycrystalline copper metal flag (Alfa Aesar, Puratronic ≥99.9999%, 0.25 mm thickness) was cut and affixed to Ti wire at the flag handle to establish contact to the potentiostat clip. The Ti contact wire was then threaded through a septum (Chemglass, Suba-Seal) to form

a working electrode assembly. Prior to insertion into the cell, the flag was cleaned by oxidative stripping in a two-electrode setup with a copper flag counter electrode at +2 V in orthophosphoric acid for 450 s. The flag was then rinsed with copious amounts of MilliQ water and dried under a stream of air. Following electrolysis, the electrode was rinsed with acetone, then water, and stored in atmospheric conditions.

Preparation of pc-Cu cylinder working electrode. Cu cylinder working electrodes were cut from a larger Cu rod (McMaster-Carr, 99.99%) and affixed to a PEEK electrode holder assembled onto a rotator shaft (Metrohm). The rotator shaft was affixed to the cell utilizing a ground glass adapter and sealed using a combination of Teflon tape and silicone grease. Before first use, the electrodes were first polished using sandpaper (Grainger, ultra-fine 1500 Grit Silicon Carbide) and then electropolished five times consecutively at 400 RPM using the previously described procedure. Cylinders used thereafter were then electropolished as described above.

Preparation of Ag/AgCl reference electrode. Ag/AgCl leakless reference electrode (EDAQ) was utilized as a pseudo reference. Prior to electrolysis, the electrode was rinsed with water and dried under a stream of air. Following electrolysis, the electrode was cleaned in the same manner as the Cu flag working electrode and stored in water.

Preparation of Pt mesh counter electrode. The Pt mesh counter electrode (BeanTown Chemical, ≥99.9% trace metals basis, 52 mesh gauze woven from 0.1 mm wire) was cleaned with piranha acid (see section 3.6.3 below for preparation), rinsed with water, dried and stored in a 140 °C oven. Prior to electrolysis, the electrode was heated with a butane torch for a few minutes to a red-white glow prior to threading through a septum and insertion into the cell.

Preparation of the Pt gas diffusion working electrode (GDE). Pt GDEs were used as received (Fuel Cell Store, 0.5 mg/cm^2 PtC 60%). Strips of the electrode were cut using ceramic scissors, affixed to a Ti wire, and threaded through a Suba-Seal septum to interface with the cell. Note that Pt GDE were utilized as a source of high surface area platinum electrodes, and whether they form a solvophobic gas layer, as they do in aqueous electrolytes, was not determined from our studies.

Preparation of Nafion membrane. Nafion 117 (Fuel Cell Store) was used as the separator. When used as received Nafion was found to introduce adventitious strongly acidic impurities in the electrolyte, as determined by voltammetry. This is consistent with its structure, since it natively contains protonated sulfonate groups. To mitigate these impurities, the mobile protons were exchanged with TBA^+ cation in the following manner. First, Nafion was cut into ca. 1.5 x 1.5 cm^2 squares with ceramic scissors. Ten films were soaked at a time in 40 mL of a 1 M solution of tetrabutylammonium bromide in DMSO for at least an hour. The containing solution turned yellow, presumably due to the formation of hydrogen bromide,

indicating successful exchange. The films were then rinsed twice with pure DMSO, soaked for an hour, and then rinsed once again before use. All remaining films were stored in neat DMSO.

3.6.2. Synthesis and preparation of phenol / tetrabutylammonium phenoxide buffer electrolytes

Synthesis of phenol / tetrabutylammonium phenoxide buffer salts. Tetrabutylammonium phenoxide (TBAPhO) salts were synthesized as a buffer (PhOH/TBAPhO) via a salt metathesis of a 3:1 molar ratio of phenol to tetrabutylammonium hydroxide. All reagents used and chemicals prepared in this subsection were handled and stored under nitrogen atmosphere in a glovebox. Phenol was dissolved in a small amount of diethyl ether, and TBAOH in methanol solution was added dropwise. The solution was stirred for 1 hour, and the solvent was removed *in vacuo* to isolate the resultant buffer crystals. Diethyl ether was periodically added as the product congealed to liberate residual methanol from the crystals. The identity and expected relative molar ratios of the donor to the conjugate base of the product were quantified via peak integration with ^{1}H NMR with long relaxation delay (ca. d1 of >15 s). The molar ratios of phenol to phenoxide determined from NMR did not correlate with the predicted ratios from the analytically added amounts of reagent, presumably due to sublimation of free phenol during drying *in vacuo*. Thus, the ratios determined from NMR analysis were used to calculate the composition of buffer for electrolyte solutions.

Preparation of electrolyte. DMSO and $TBAPF_6$ were stored and handled under ambient atmospheric conditions. Electrolyte solutions were prepared by mixing DMSO and the corresponding amount of PhOH/TBAPhO buffer in conical centrifuge tubes (Corning) under atmospheric conditions. For each buffer condition, $TBAPF_6$ was added to form solutions of a constant ionic strength of 0.3 M of TBA^+ cation.

3.6.3. General procedure for galvanostatic polarization experiments

(The following procedure produces the data gathered in **Figures 3.2, 3.3, 3.4b, 3.5** and **Figures S3.3-3.5, S3.8-3.9, S3.11-3.12**)

Preparation of divided H-cell

Cleaning of H-cells. All Cu polarization measurements were conducted in a custom-made glass body H-cell (James Glass Inc.). Prior to assembly, all glass components were soaked in piranha acid for at least an hour, which was prepared from a 4:1 v/v ratio of sulfuric acid to hydrogen peroxide, to remove trace organic and metallic residues. The cells were then further cleaned by extensive rinsing in Milli-Q water and drying in an oven at 140 °C for at least an hour where they were stored. Plastic components of the cell, including screw caps (Chemglass) and O-rings (Chemglass, Viton), were washed with ethanol, dried, and stored in a 60 °C oven for at least 24 hours.

Safety precaution: *Piranha acid is a highly reactive and corrosive liquid, and forms gases at the start of and for hours after its preparation; great care must be taken to safely use and dispose of it. Piranha acid was prepared and handled within a secondary container in an acid hood. Once used, piranha solutions were treated via addition of small amounts of an aqueous solution of 1 M solution of $FeCl_3$ and heated to 50 °C to accelerate peroxide decomposition. Once bubble formation was visibly complete, the solution was poured into a plastic-coated glass waste bottle, left to stand for one week to further cure the solution, sealed with a vented cap, and then disposed of as chemical waste.*

Assembly of H-cells. The cathode compartment, the working, and the reference electrode were rinsed with neat DMSO prior to assembly. All components not connected via a septum were sealed to the cell using a #7 screw cap and Viton O-ring assembly (Chemglass). CO or Ar gas was aeriated in the working compartment through a porous glass frit, while the out flow of the cell was connected directly to a gas chromatograph for gaseous product detection (SRI Instruments, Multi-Gas Analyzer #3). Gas flow was controlled using mass flow controllers (Aalborg DFC, 0 − 50 mL/min) typically set to 30 mL/min of CO or Ar flow. The working compartment, filled with ca. 17 mL of solution, was continuously stirred at 1150 RPM (IKA) with a magnetic PTFE stir bar (VWR). After assembly and prior to electrolysis, the cell was left to equilibrate for at least 15 minutes as determined by approach of the measured open circuit potential (OCP) value to equilibrium.

Measurement sequence

All electrochemical experiments described herein were conducted with a Gamry Reference 600 potentiostat.

Pre-polarization. The Ohmic drop was measured via potentiostatic electrochemical impedance spectroscopy (PEIS) prior to measurement between 1 MHz and 50 Hz with an AC voltage amplitude of 5 mV rms. The resistance value was taken at the minimum measured phase angle at the high frequency limit: this value was used for post-electrolysis iR correction during data workup. Then, linear sweep voltammetry was conducted from the measured open circuit potential to ca. −10 mA. The cathode was then preconditioned under galvanostatic polarization at −4 mA until ca. 0.66 C of charge per cm^2 of geometric surface area of Cu was passed to reduce surface oxides and induce restructuring, which was conducted to obtain reproducible results.

Polarization. To collect polarization data, chronopotentiometry experiments were conducted sequentially and in tandem with gas chromatographic sampling of the effluent gas stream (see “Gaseous product analysis” below for details). Because each gas chromatographic measurement took 20 minutes to complete, galvanostatic polarization was conducted sequentially for 7 minutes, followed by 13 minutes of

delay at OCP. Polarization was stepped from lowest to highest applied current in the order of −0.5 mA, −1 mA, and then 1 mA interval steps thereafter up to −10 mA. The potential of product formation was sampled from the latter half of the chronopotentiogram, during which the reaction was taken to be at steady state.

In an aprotic non-aqueous electrolyte, polarization can induce changes to the bulk concentration of donor / conjugate base over time and convolute kinetic measurements for products which have a rate dependence on the donor. Using galvanostatic control of the reaction, and assuming that electrons and protons are transferred as equimolar equivalents (for either hydrogen evolution or CO reduction), this procedure ensures that the initial donor concentration does not deviate by more than 10% for any set of polarization experiments conducted in a single cell.

Post-polarization. Following polarization, a small amount (~1 mg) of $CoCp_2$ was added to the cell and the half-wave potential was measured via cyclic voltammetry at 100 mV/s using a glassy carbon disk working electrode (BASi) without stirring and without agitation from the gas input. All potentials reported are converted to the reversible couple, which typically fell within the range of −0.880 to −0.890 V vs. Ag/AgCl pseudo-reference electrode. Some variation in the potential was observed between specific lots of reference electrodes, but the potential for a single reference electrode was consistent between experiments.

Gaseous product analysis. All gaseous products were identified and quantified via gas chromatography following a literature protocol.[21] The product stream was sampled 1 minute prior to the end of the electrolysis by injection of the effluent stream into the chromatograph. Effluent separation was accomplished with two MolSieve 13X and Hayesep D columns connected in series (SRI Instruments), while detection was accomplished with a thermal conductivity detector (TCD) and flame ionization detector (FID) (SRI Instruments). The peak position and quantity of gaseous products were calibrated to a custom-order gas standard (Airgas). The partial current density for each product was calculated using the following equation, where c_i is the GC detected product in ppm, n_i is the electron stoichiometry for product i, F is Faraday's constant (96485 C mol^{-1}), V_{gas} is the substrate gas flow rate, P is the pressure in the cell (1 atm) and A is the sample surface area.

$$j_i = c_i * n_i * F * V_{gas} * \frac{P}{RT} * \frac{1}{A}$$

The faradaic efficiency is calculated by dividing the partial current of a product by the applied current for a given electrolysis experiment. Faradaic efficiency that could not be accounted for from gaseous product quantification was further investigated by analyzing for solution-phase products, as described in the main text.

Data workup and analysis

Most current-potential data were collected in triplicate, except for select data points which are in duplicate, and the 1330 mM $C_{A,0}$ condition which was collected in quintuplicate. All errors reported are with respect to the standard deviation, and the current density was calculated using the electrochemically active surface area of the electrode unless otherwise stated (described below). The lowest applied galvanostatic current (−0.5 mA) within an experiment was discarded due to high measurement uncertainty. All slopes were obtained by least-squares fitting to the averaged data of all replicates. For Tafel slope determination, the five most anodic data points were sampled. The value and error of all slope values shown in a given figure were sampled from the number of conditions varied shown in a particular plot (i.e. n = 4 for C_{HA}/C_{A-} variation experiments, n = 3 for $j_{C2H4/H2}$ variation experiments). For experiments utilizing the Cu foil, every instance of a replicate employed a freshly cleaned cell assembly, reference electrode, Nafion separator, platinum counter electrode, electrolyte solution, and electropolished Cu foil electrode.

3.6.4. Measurement of the geometric and electrochemically active surface area (ECSA) of the working electrode

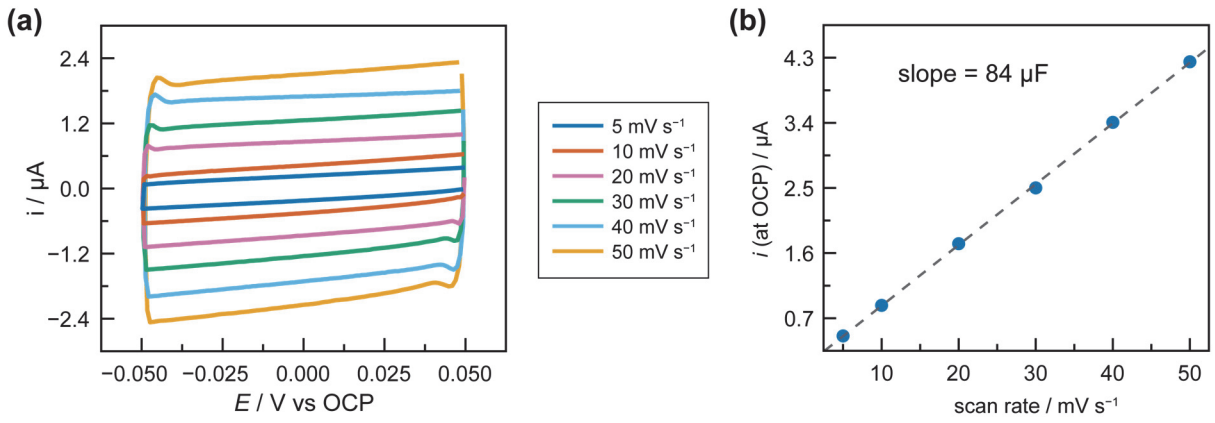

Figure S3.1. (a) Cyclic voltammograms (CV) collected on pc-Cu foil following electrolysis in 330 mM $C_{A,0}$ buffer at various scan rates for determination of surface capacitance. Scans are centered around the OCP as defined by the potential after 100 s of equilibration (b) Plot of the cathodic and anodic current difference, centered around OCP, of each CV measured as a function of their scan rates. The slope value is obtained from the linear fit to the data.

The electrochemically active surface area (ECSA) of the Cu foil was measured using a previously reported double-layer capacitance method.[30] The surface capacitance of the electrode was measured following electrolysis in 330 mM $C_{A,0}$ buffer using cyclic voltammetry. After equilibration of the cell to the open-circuit potential (OCP) for 100 s, the potential was swept within a 100 mV window centered on the OCP at 5, 10, 20, 30, 40, and 50 mV s^{-1} (**Figure S3.1a**). The capacitance was calculated from a slope of a plot of the cathodic and anodic current difference at the OCP versus the scan rate (**Figure S3.1b**) and

divided by the reported calibration value of 11 uF cm^{-2} to obtain the ECSA of the foil of 3.820 cm^2. All reported current densities utilizing the foil are normalized to this value.

For the analysis of transport effects determined via rotation experiments (as detailed later), the surface area of the flag was normalized by the geometric surface area. This was determined by integrating the area of a photo of the electrode, using a ruler as a scale bar, with ImageJ software; the geometric area of the flag for this work was 2.852 cm^2. The geometric surface area of the cylinder was determined from the exposed surface area of the assembly, which was calculated from the radius and height of the cylinder as measured using calipers. The geometric area of the cylinder for this work was 3.205 cm^2.

3.6.5. UV-visible spectroscopic analysis of anolyte product crossover

(The following procedure produces the data gathered in **Figure S3.2**.) To determine the extent of crossover of the anodic reaction product to the catholyte, UV-visible spectroscopy of the electrolyte prior to and after electrolysis was conducted in the following manner. A sample of the freshly prepared electrolyte was transferred to an airtight quartz cuvette (Spectrosil Far UV Quartz, Starna Cells) using a pipette. To prevent exposure of the electrolyzed solution to air, additional quartz cuvettes were cleared of air via flowthrough of nitrogen gas. Then, a syringe equipped with a metal needle was used to transfer 3 mL of the catholyte and 0.3 mL of anolyte to the cuvettes following electrolysis in 330 mM $C_{A,0}$ buffer. The anolyte was subsequently diluted ten-fold with neat DMSO, and scans of the solution were taken from 800 to 200 nm wavelengths using a UV-visible spectrometer (Cary 500) against a background cuvette containing pure DMSO.

3.6.6. Voltammetry of phenol and water under inert atmosphere

(The following procedure produces the data gathered in **Figure S3.3**.) Identification of the solvent window in DMSO with 0.3 M $TBAPF_6$ electrolyte, and subsequent voltametric analysis of water and phenol under inert Ar atmosphere, was conducted in the same H-cell setup described previously.

3.6.7. Identification of solution products and enriched ethylene via carbon-13 labeling

Identification of solution products. (The following procedure produces the data gathered in **Figure 3.2b** and **Figure S3.6**.) Detecting liquid products entails an analysis method compatible with high ionic strength, low boiling point non-aqueous electrolyte samples. Although the electrolyte can be sampled with ^1H NMR, the analysis of solution products is complicated by proton signals arising from 1) DMSO 2) tetrabutylammonium cation and 3) phenol / phenoxide. Instead, ^{13}C NMR was utilized to analyze the solution using a custom quantitative carbon-13 NMR protocol with inverse gated ^1H-decoupling on an electrolyte sample prepared following electrolysis with ^{13}C-enriched carbon monoxide as the substrate gas.

The cell setup and experimental details are identical to the preparation described above, with the following modifications. ^{13}CO was flowed into the cell at 5 mL min^{-1}, and galvanostatic polarization was conducted at −8 mA for 2.8 hours. Electrolyte solutions before and after electrolysis were prepared for NMR by addition of 70 μL d^6-DMSO to 630 μL of electrolyte, followed by 20 μL of 1,4-dioxane as an internal standard. Quantitation was then conducted by integrating the observed signal relative to 1,4-dioxane, assuming a natural abundance of carbon-13 of 1.1%. The faradaic efficiency for gaseous products was simultaneously sampled during electrolysis via the procedure described above, while the faradaic efficiency for solution products was calculated via the molar ratio of the electrons passed to form each product divided by the total charge passed over the course of the electrolysis.

Determination of enriched ethylene formation. (The following procedure produces the data gathered in **Figure S3.7**.) To extract ethylene from the reaction for qualitative determination of enrichment via NMR, the effluent gas stream was fed into a J-Young tube bathed in liquid Ar at a rate of 5 mL min^{-1} during polarization. Liquid Ar (b.p. = −186 °C) is ideal given that it is cold enough to freeze ethylene (m.p. = −169.2 °C) but is not cold enough to condense CO (b.p. = 191.5 °C). In contrast, liquid N_2 will do both and is not advised for this experiment. Prior to immersion in liquid Ar, $CDCl_3$ was added to the tube. For the reported data, polarization was conducted at −8 mA for 6000 s with a phenol buffer concentration of $C_{A,0}$ = 160 mM (4:1 ratio of $C_{HA,0}$:$C_{A-,0}$). Halfway through polarization, an additional equimolar amount of phenol was added to the catholyte to refresh the bulk concentration of donor. Following polarization, the gas feedthrough tube leading to into the J-Young tube was removed, and the NMR tube quickly sealed and warmed up to room temperature. Note that ethylene was not quantified from this technique, since it is not assumed that the collection efficiency of this method is 100%.

3.6.8. Determining the influence of transport limitations via polarization with a rotating cylinder electrode

(The following procedure produces the data gathered in **Figure S3.4**.) Rotation experiments were conducted to probe the effects of mass transfer using the protocols as described above in an airtight cell, with the following procedural modifications. All pre-polarization experiments were conducted at 1600 rpm. Galvanostatic polarization experiments were conducted between −0.5 mA to −6 mA to encompass the lower bounds of the galvanostatic range utilized for Tafel slope measurements using the pc-Cu flag. Tafel data was collected at 0 rpm and 1600 rpm within a single cell in duplicate; one duplicate was first polarized at 0 rpm and then 1600 rpm, while the other was collected in reverse rotation order.

3.6.9. Calibrating for solution non-idealities via the H^+/H_2 equilibration potential on Pt GDEs

The following procedure produces the data gathered in Figure 3.4a and Figure S3.9.

Preparation of single-compartment cell

Electrochemical measurements were conducted in a 20 mL 3-neck round bottom flask (Chemglass). The cell was washed with acetone and copious amounts of water and then dried and stored in a 140 °C oven prior to use. The Ag/AgCl reference electrode was prepared in the same manner as previously described and fitted through a septa to create an airtight connection to the cell. The Pt GDE, Ag/AgCl reference electrode, and Pt mesh counter electrode were washed with pure DMSO prior to insertion into the cell. Approximately 12 mL of buffer solution was added to each cell to sufficiently submerge each electrode component. The gas flow was varied using two mass flow controllers (Aalborg DFC or Alicat) connected to hydrogen and argon. Gas was aerated through the cell using a metal needle and a PTFE stir bar.

Measurement sequence

The open circuit potential was measured at each condition until the potential approached equilibrium, defined by $\Delta E < |1\ mV|$ over a 100 s time window. On average, each measurement took ca. 500 s to approach equilibrium. The partial pressure of hydrogen for each experiment was varied by controlling the relative volumetric flow of hydrogen and argon using mass flow controllers set to a total volumetric flow of 30 mL min^{-1}. The $CoCp_2$ reference couple was measured at the end of each set of measurements conducted in a single cell and assumed to be identical for each measurement conducted therein. Each replicate for a set of measurements utilized the same cell, reference, and counter electrode, but fresh Pt GDE working electrodes and solutions prepared from the same batch. Experiments where the buffer concentration was varied utilized a fresh cell setup prepared in the manner described above to avoid contamination with the previous electrolyte condition.

Data workup and analysis

Data points and errors are reported from these measurements are the average and standard deviation of triplicate measurements. All slopes were obtained by least-squares fitting to the averaged data of all replicates. The average value and error for all reported slope values were sampled from the number of conditions varied shown in their respective figures.

3.7. Supplementary Discussion

3.7.1. The anodic phenoxide oxidation product does not crossover to the catholyte compartment

In this system, hydrogen / water oxidation does not occur at the anode, and hence the electrochemically consumed donor is not reprotonated in a closed loop. Instead, we observe coloration of the anolyte from

clear to, yellow to, by the end of electrolysis, deep blue. We ascribe the anodic product to the oxidation of phenoxide to phenoxy radicals, whose coloration has been previously reported.[31] To determine whether the Nafion separator was effective at preventing crossover of this product to the cathode, 330 mM $C_{A,0}$ electrolyte was sampled via UV-visible spectroscopy before and after electrolysis.

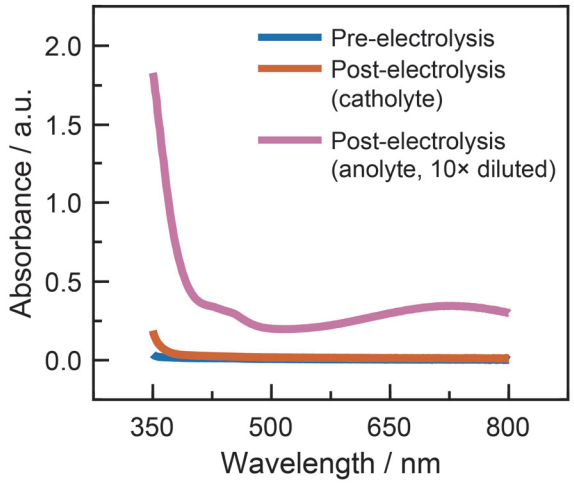

Figure S3.2. UV-visible spectra of the electrolyte before electrolysis (blue), and of the catholyte after electrolysis (orange), and anolyte (pink) after electrolysis and 10× dilution in DMSO.

Figure S3.2 shows that the absorbance features of the anodic product are not present in the catholyte following electrolysis, suggesting that crossover of the product does not occur using the Nafion separator.

3.7.2. Water is not a thermokinetically competent donor

Although operating in a non-aqueous electrolyte can enable selective proton donation by excluding water, it is infeasible to operate a reaction with a rigorously dry electrolyte,[32,33] especially for this reaction where water is a byproduct of carbon monoxide deoxygenation. Despite its presence, we postulated it would not compete with phenol as the thermokinetically relevant donor, since phenol a) is present in relative excess and b) has a substantially lower pK_a (i.e. is a much stronger acid pK_a = 18.0 in DMSO versus 31.4 of water in DMSO).[25] The concentration of water in DMSO solvent was quantified using ^{1}H NMR and tetrabutylammonium hexafluorophosphate ($TBAPF_6$) as the integration standard, which revealed an adventitious water concentration of 16 mM. These concentrations are far lower than the phenol concentrations used in the reported experiments.

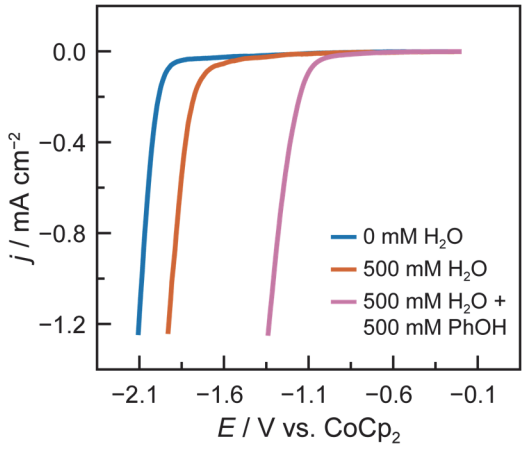

Figure S3.3. Linear sweep voltammograms of DMSO and 0.3 M $TBAPF_6$ electrolyte solutions with various molarities of added water and PhOH. Scans were measured towards negative potentials at 50 mV s^{-1} on pc-Cu flag electrode. All potentials are referenced to the cobaltocenium ($CoCp_2$) redox couple. All current densities are normalized with respect to the elec-trochemically active surface area.

Then, to determine the thermokinetically relevant donor, cathodic linear sweep voltammetry in neat solutions of DMSO and $TBAPF_6$ supporting electrolyte were conducted under Ar atmosphere to identify the onset of proton reduction with sequentially added quantities of water and phenol (**Figure S3.3**). Without any added water, the onset of reduction occurs at ca. −1.95 V vs. $CoCp_2$, confirming that the potential of the observed catalysis (ca. −1.05 vs. $CoCp_2$) occurs far positive of the solvent reduction window. Even with 500 mM of added water, this window shifts anodically by ca. 200 mV, confirming that water is not the operative donor at the measured potentials (nor any other deleterious reduction process, such as solvent reduction). Finally, when 500 mM of phenol is added to same electrolyte solution, a large current is observed at even more positive potentials near the values reported in this work, demonstrating that phenol controls the thermokinetics of proton transfer under polarization.

3.7.3. Polarization at low applied current densities is largely insensitive to transport effects

To understand whether the observed current densities sampled for Tafel analysis for ethylene formation were affected by transport effects, we performed electrolysis with and without rotation on a Cu cylinder in the lowest buffer strength electrolyte (330 mM $C_{A,0}$). The 330 mM $C_{A,0}$ is probed because it is the most likely condition to be transport limited in the reactant. We note that because polarization experiments were conducted at the same galvanostatic currents at all buffer strengths, the rate of reactant consumption is nominally similar under all conditions. To accurately compare the effects of transport on the Cu cylinder with that of the Cu foil, the rate of reactant consumption and product generation at the interface must be nominally similar. Hence, electrolysis was conducted galvanostatically using the lowest six applied current values, the first five of which were sampled for Tafel analysis on the flag electrode. Furthermore, the partial

currents for product formation were normalized to the geometric surface area, which were similar between the flag (2.865 cm^2) and the cylinder (3.205 cm^2) electrode.

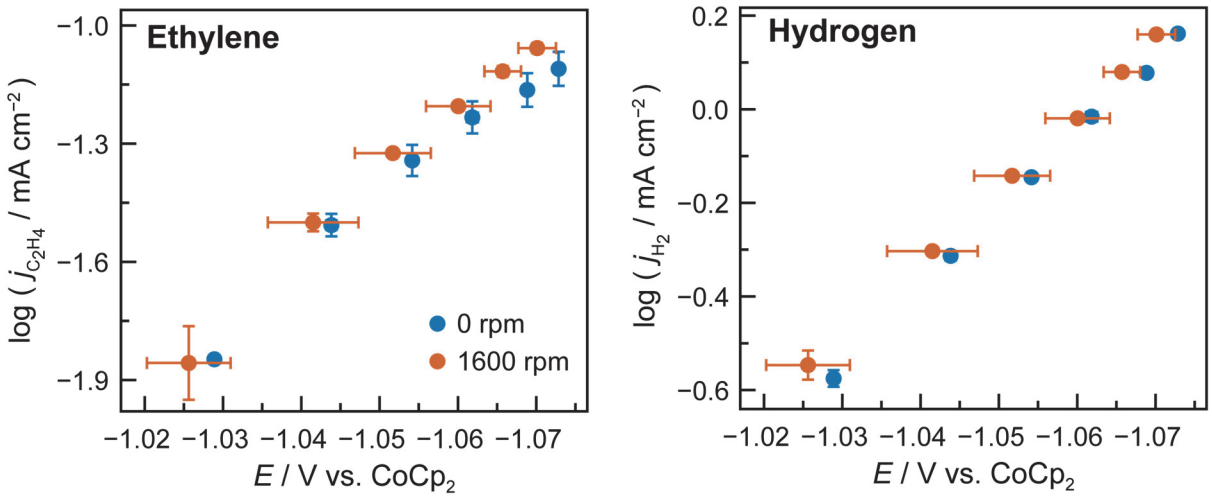

Figure S3.4. Current density vs. potential curves for ethylene (left) and hydrogen (right) formation on pc-Cu cylinder rotating electrode, without rotation (blue) and with rotation at 1600 rpm (orange). Polarization experiments were conducted from −0.26 to −2.6 mA cm^{-2} applied current. All potentials are referenced to the cobaltocenium ($CoCp_2$) redox couple. All current densities are normalized with respect to the geometric surface area.

Figure S3.4 shows the partial current density for both ethylene and hydrogen formation as a function of applied potential with and without rotation at 1600 rpm. Ethylene formation is within error of the measurement for all but the highest current density data points. The formation rate of hydrogen is invariant with rotation rate under all polarization conditions. Though the system is largely unaffected by transport in the low-current density regime, we emphasize that any existing transport convolution would only serve to increase Tafel slopes relative to their authentic values, further substantiating our observation of a low Tafel slope.

3.7.4. Estimation of the overpotential and standard redox potential for the CO-to-ethylene half reaction

Because Tafel data is only valid in the limit that the reverse reaction is negligible, we sought to estimate the reaction overpotential by determining the standard redox potential for CO-to-ethylene half reaction in DMSO. The thermodynamic potential for the CO-to-ethylene half reaction in water is 0.170 V positive of the thermodynamic potential for the H^+/H_2 half reaction.[3] The difference between the thermodynamic potentials of these two half reactions has been found to be minimally dependent on the solvent.[34] Hence, as an estimate, the potentials referenced versus RHE can be readily converted to an estimated overpotential for the ethylene formation half-reaction by adding 0.170 V to the absolute value of the labeled potential

(see **Figure 3.5**, **Figure S3.11**, and **Figure S3.12**). Across the entire study, all overpotentials are sufficiently high enough to exclude contribution of the back reaction to the observed current densities.

3.7.5. Calculation of phenol / phenoxide speciation from the homoconjugation constant

In aprotic solutions with neutral donors / anionic conjugate bases, a solution equilibrium process that arises is homoconjugation, where free donor and conjugate base equivalents spontaneously form a homodimer.[27]

$$HA + A^- \rightleftarrows HA_2^-$$

Consequently, the true concentrations of C_{HA} and C_{A-} will differ from their initial concentrations depending on the value of K_{hc}, where HA = PhOH and A^- = PhO^-, and HA_2^- = $H(PhO)_2^-$. A K_{hc} of 2291 was used in this work in accordance with literature values for phenol / phenoxide,[35] and all solutions were prepared at initial concentrations of $C_{HA,0}$ and $C_{A-,0}$ to yield buffer conditions involving varying C_{HA} and fixed C_{A-}.

Table S3.1. Phenol speciation in DMSO electrolytes after accounting for homoconjugation with K_{hc} = 2291.

#	$C_{A,0}$ (mM)	C_{HA} (mM)	C_{A-} (mM)	C_{HA2-} (mM)
1	330	200	0.15	66
2	670	400	0.15	133
3	1000	600	0.15	199
4	1330	800	0.15	265

All calculated C_{HA} and C_{A-} values presented assume that homoconjugation is the only equilibrium process, but this alone does not preclude the presence of additional equilibria which could impact the genuine activities of all solution species (as described in the main body of the text).

3.8. Supplementary Data

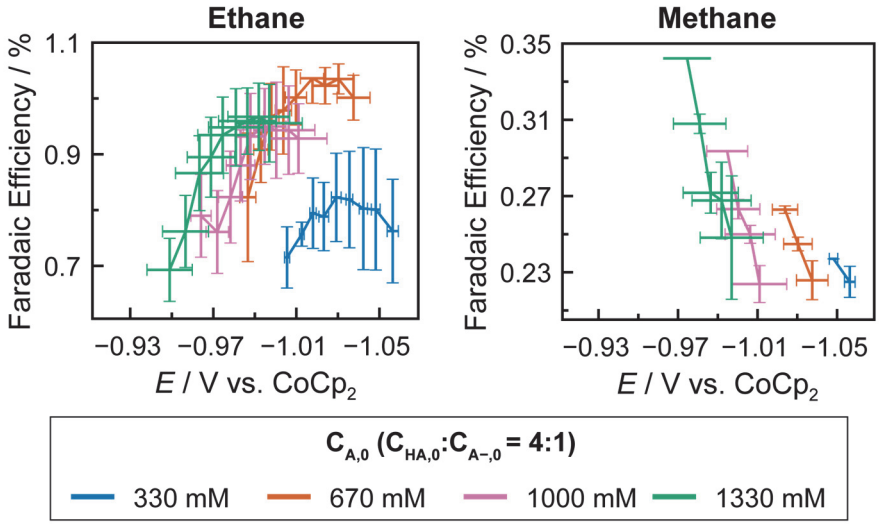

Figure S3.5. Potential-dependent Faradaic efficiency trends for ethane and methane in DMSO/TBAPF$_6$ electrolyte collected under various analytical PhOH/PhO$^-$ buffer strengths ($C_{A,0}$) with a 4:1 analytical ratio of PhOH ($C_{HA,0}$) and TBAPhO ($C_{A-,0}$). Experiments were conducted via steady-state galvanostatic polarization from −0.26 to −2.6 mA cm^{-2} applied current on pc-Cu catalyst. All potentials are referenced to the cobaltocenium ($CoCp_2$) redox couple. The data points and error bars correspond to the average and standard deviations of at least two or more independent measurements.

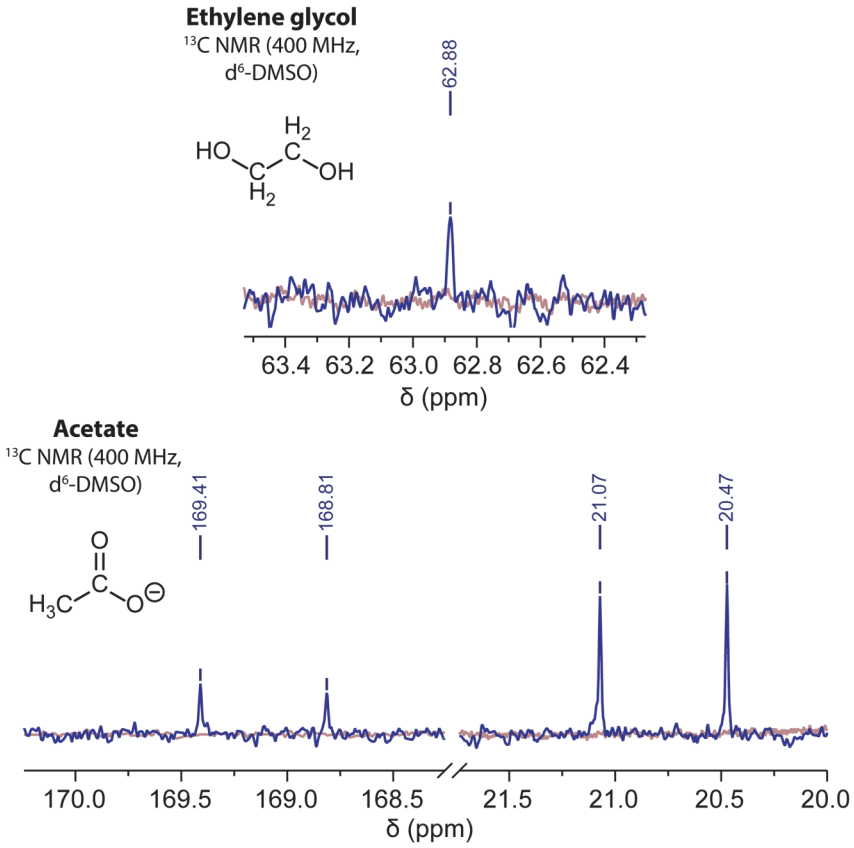

Figure S3.6. ^{13}C NMR spectra of ethylene glycol (top) and acetate (bottom) from an electrolyte sample before electrolysis (red) and after electrolysis with ^{13}C-enriched CO (blue). Electrolyte samples were prepared by addition of d^6-DMSO up to 10% volume prior to analysis.

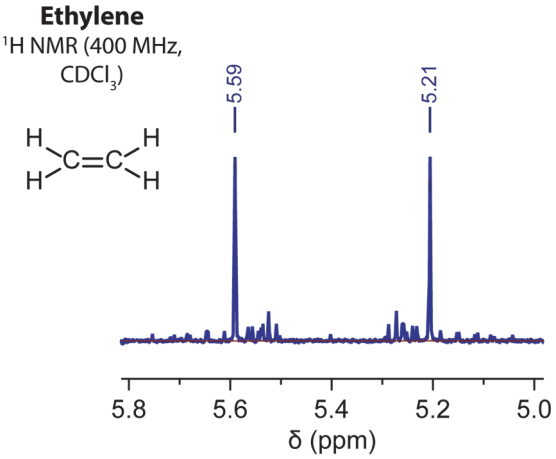

Figure S3.7. ^{1}H NMR of ethylene from an electrolyte sample before electrolysis (red) and after electrolysis with ^{13}C-enriched CO (blue). Ethylene was collected in an airtight NMR tube containing $CDCl_3$, which was bathed in liquid Ar from the effluent gas stream of the reactor.

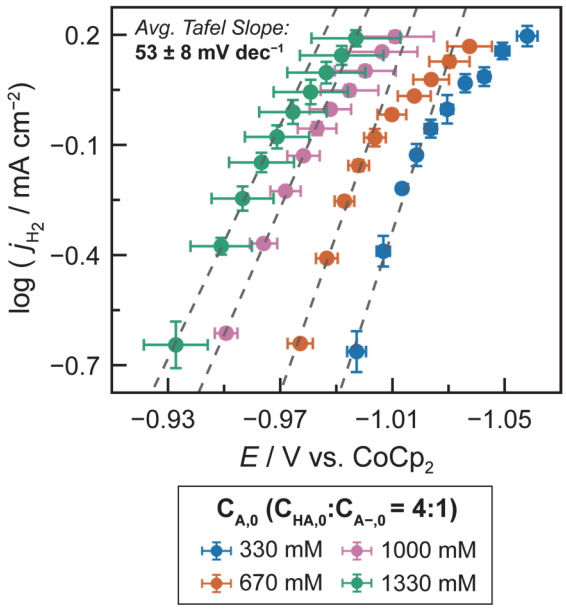

Figure S3.8. Current density vs. potential (Tafel) plots for hydrogen formation as a function of the analytical PhOH/PhO$^-$ buffer strength ($C_{A,0}$) in DMSO/TBAPF$_6$ electrolyte, with a 4:1 analytical ratio of PhOH ($C_{HA,0}$) to TBAPhO ($C_{A^-,0}$). Experiments were conducted via steady-state galvanostatic polarization from −0.26 to −2.6 mA cm^{-2} applied current on pc-Cu catalyst. All potentials are referenced to the cobaltocenium ($CoCp_2$) redox couple. All current densities are normalized with respect to the electrochemically active surface area. The Tafel slope for each condition was calculated from a linear fit to the lowest five applied currents. The data points and error bars correspond to the average of at least two independent measurements.

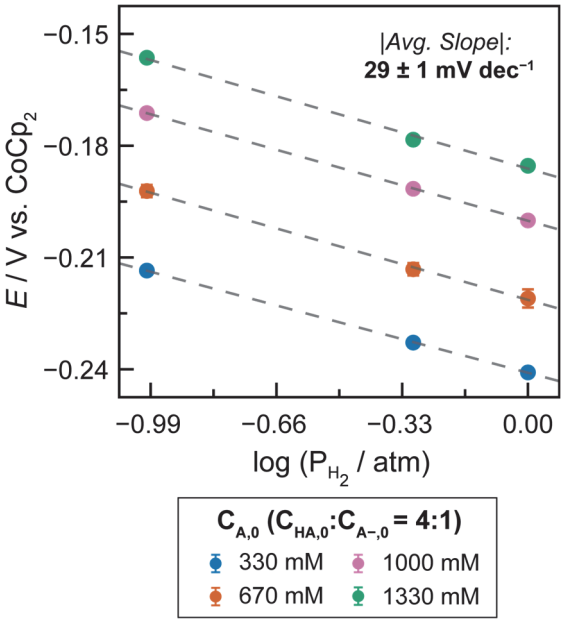

Figure S3.9. Equilibrium potential of a Pt electrode equilibrated to the H$^+$/H$_2$ reaction as a function of the partial pressure of H$_2$ (P_{H2}) in DMSO. The colors denote varying PhOH/PhO$^-$ buffer conditions. All potentials are referenced to the cobaltocenium ($CoCp_2$) redox couple. The data points and error bars correspond to the average of triplicate measurements; error bars not visible are smaller than the data points shown.

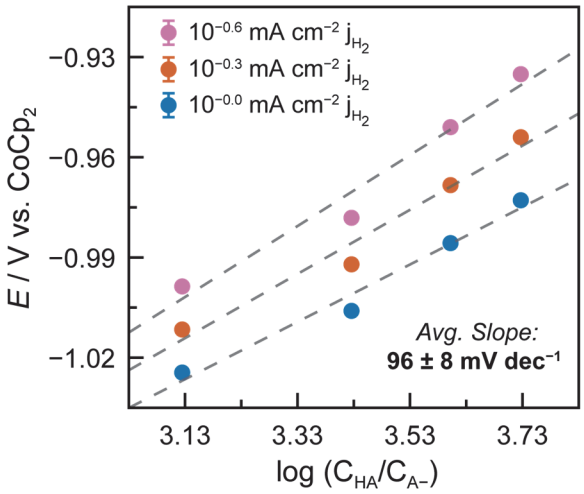

Figure S3.10. Steady state reaction potential for hydrogen formation on pc-Cu as a function of CHA/CA− ratio as calculated from the PhOH/PhO– homoconjugation constant in DMSO. The colors denote varying partial current densities for hydrogen formation. All potentials are referenced to the cobaltocenium ($CoCp_2$) redox couple. The data points and error bars correspond to the average of triplicate independent measurements; error bars are smaller than the data points shown.

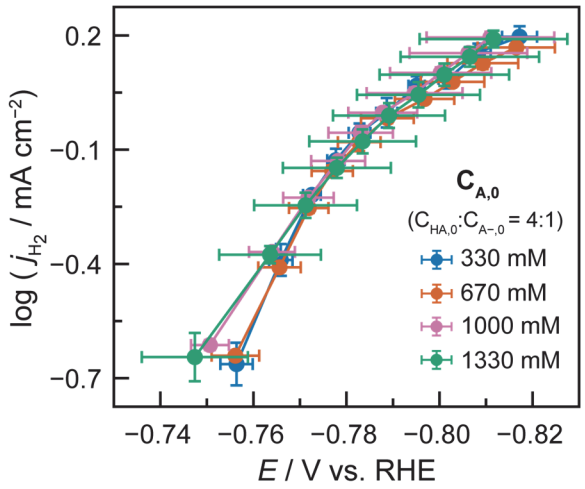

Figure S3.11. Hydrogen partial current density vs. potential (Tafel) plots on the reversible hydrogen electrode (RHE) scale. Hydrogen Tafel plots were sampled as a function of the analytical PhOH/PhO$^-$ buffer strength ($C_{A,0}$) in DMSO/$TBAPF_6$ electrolyte, with a 4:1 analytical ratio of PhOH ($C_{HA,0}$) to TBAPhO ($C_{A-,0}$). All current densities are normalized with respect to the electrochemically active surface area. The data points and error bars in this plot were calculated using the equilibrium potential of H^+/H_2 from **Figure 3.4a** and applied potential from the polarization curves from **Figure S3.8**.

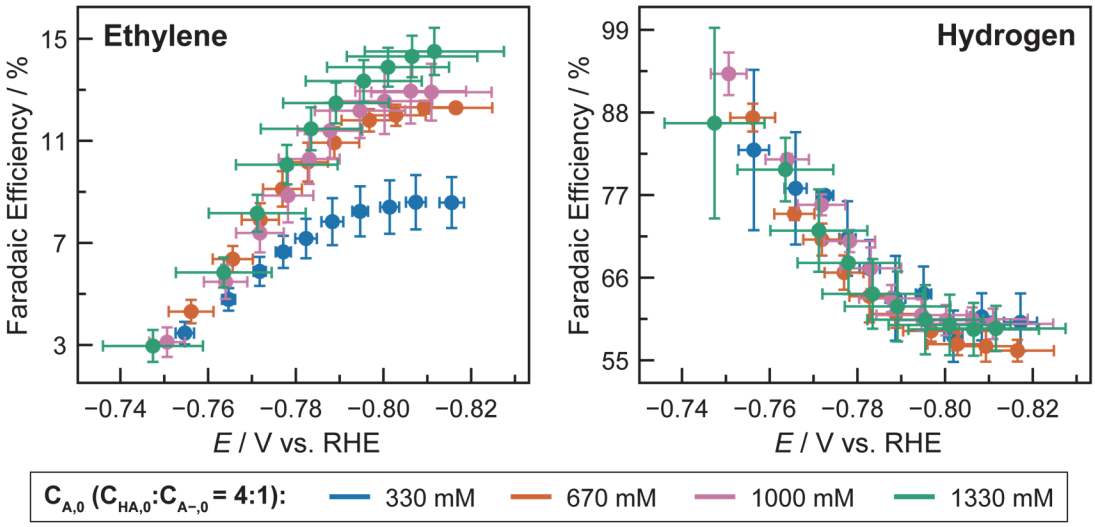

Figure S3.12. Potential-dependent faradaic efficiency trends for ethylene and hydrogen formation plotted on the RHE scale. Data compares trends as a function of the analytical PhOH/PhO$^-$ buffer strength ($C_{A,0}$) in DMSO/TBAPF$_6$ electrolyte, with a 4:1 analytical ratio of PhOH ($C_{HA,0}$) to TBAPhO ($C_{A-,0}$). The data points and error bars in this plot were calculated using the equilibrium potential of H^+/H_2 from **Figure 3.4a** and applied potential from the polarization curves from **Figure 3.2a**.

3.9. References

(1) Shih, C. F.; Zhang, T.; Li, J.; Bai, C. Powering the Future with Liquid Sunshine. *Joule* **2018**, *2* (10), 1925–1949.

(2) De Luna, P.; Hahn, C.; Higgins, D.; Jaffer, S. A.; Jaramillo, T. F.; Sargent, E. H. What Would It Take for Renewably Powered Electrosynthesis to Displace Petrochemical Processes? *Science (1979)* **2019**, *364* (6438), eaav3506.

(3) Nitopi, S.; Bertheussen, E.; Scott, S. B.; Liu, X.; Engstfeld, A. K.; Horch, S.; Seger, B.; Stephens, I. E. L.; Chan, K.; Hahn, C.; Nørskov, J. K.; Jaramillo, T. F.; Chorkendorff, I. Progress and Perspectives of Electrochemical CO_2 Reduction on Copper in Aqueous Electrolyte. *Chem Rev* **2019**, *119* (12), 7610–7672.

(4) Todorova, T. K.; Schreiber, M. W.; Fontecave, M. Mechanistic Understanding of CO_2 Reduction Reaction (CO_2RR) Toward Multicarbon Products by Heterogeneous Copper-Based Catalysts. *ACS Catal* **2020**, *10* (3), 1754–1768.

(5) Hori, Y. Electrochemical CO_2 Reduction on Metal Electrodes. In *Modern Aspects of Electrochemistry*; Springer New York: New York, NY; pp 89–189.

(6) Zhang, H.; Li, J.; Cheng, M.-J.; Lu, Q. CO Electroreduction: Current Development and Understanding of Cu-Based Catalysts. *ACS Catal* **2019**, *9* (1), 49–65.

(7) Kas, R.; Kortlever, R.; Yılmaz, H.; Koper, M. T. M.; Mul, G. Manipulating the Hydrocarbon Selectivity of Copper Nanoparticles in CO_2 Electroreduction by Process Conditions. *ChemElectroChem* **2015**, *2* (3), 354–358.

(8) Higgins, D.; Hahn, C.; Xiang, C.; Jaramillo, T. F.; Weber, A. Z. Gas-Diffusion Electrodes for Carbon Dioxide Reduction: A New Paradigm. *ACS Energy Lett* **2019**, *4* (1), 317–324.

(9) García de Arquer, F. P.; Dinh, C.-T.; Ozden, A.; Wicks, J.; McCallum, C.; Kirmani, A. R.; Nam, D.-H.; Gabardo, C.; Seifitokaldani, A.; Wang, X.; Li, Y. C.; Li, F.; Edwards, J.; Richter, L. J.; Thorpe, S. J.; Sinton, D.; Sargent, E. H. CO_2 Electrolysis to Multicarbon Products at Activities Greater than 1 A Cm^{-2}. *Science (1979)* **2020**, *367* (6478), 661–666.

(10) Ovalle, V. J.; Waegele, M. M. Influence of pH and Proton Donor/Acceptor Identity on Electrocatalysis in Aqueous Media. *The Journal of Physical Chemistry C* **2021**, *125* (34), 18567–18578.

(11) Varela, A. S.; Kroschel, M.; Reier, T.; Strasser, P. Controlling the Selectivity of CO_2 Electroreduction on Copper: The Effect of the Electrolyte Concentration and the Importance of the Local pH. *Catal Today* **2016**, *260*, 8–13.

(12) Schouten, K. J. P.; Pérez Gallent, E.; Koper, M. T. M. The Influence of pH on the Reduction of CO and CO_2 to Hydrocarbons on Cu Electrodes. *Journal of Electroanalytical Chemistry* **2014**, *716*, 53–57.

(13) Hall, A. S.; Yoon, Y.; Wuttig, A.; Surendranath, Y. Mesostructure-Induced Selectivity in CO_2 Reduction Catalysis. *J Am Chem Soc* **2015**, *137* (47), 14834–14837.

(14) Liu, X.; Schlexer, P.; Xiao, J.; Ji, Y.; Wang, L.; Sandberg, R. B.; Tang, M.; Brown, K. S.; Peng, H.; Ringe, S.; Hahn, C.; Jaramillo, T. F.; Nørskov, J. K.; Chan, K. pH Effects on the Electrochemical Reduction of $CO_{(2)}$ towards C_2 Products on Stepped Copper. *Nat Commun* **2019**, *10* (1), 32.

(15) Malkani, A. S.; Anibal, J.; Xu, B. Cation Effect on Interfacial CO_2 Concentration in the Electrochemical CO_2 Reduction Reaction. *ACS Catal* **2020**, *10* (24), 14871–14876.

(16) Pérez-Gallent, E.; Marcandalli, G.; Figueiredo, M. C.; Calle-Vallejo, F.; Koper, M. T. M. Structure- and Potential-Dependent Cation Effects on CO Reduction at Copper Single-Crystal Electrodes. *J Am Chem Soc* **2017**, *139* (45), 16412–16419.

(17) Hori, Y.; Takahashi, R.; Yoshinami, Y.; Murata, A. Electrochemical Reduction of CO at a Copper Electrode. *J Phys Chem B* **1997**, *101* (36), 7075–7081.

(18) Kastlunger, G.; Wang, L.; Govindarajan, N.; Heenen HH; Ringe S; Jaramillo, T.; Hahn, C.; Chan, K. Using pH Dependence for Understanding Mechanisms in Electrochemical CO Reduction. *ChemRxiv* **2021**.

(19) Zheng, Y.; Vasileff, A.; Zhou, X.; Jiao, Y.; Jaroniec, M.; Qiao, S.-Z. Understanding the Roadmap for Electrochemical Reduction of CO_2 to Multi-Carbon Oxygenates and Hydrocarbons on Copper-Based Catalysts. *J Am Chem Soc* **2019**, *141* (19), 7646–7659.

(20) Li, J.; Chang, X.; Zhang, H.; Malkani, A. S.; Cheng, M.; Xu, B.; Lu, Q. Electrokinetic and in Situ Spectroscopic Investigations of CO Electrochemical Reduction on Copper. *Nat Commun* **2021**, *12* (1), 3264.

(21) Schreier, M.; Yoon, Y.; Jackson, M. N.; Surendranath, Y. Competition between H and CO for Active Sites Governs Copper-Mediated Electrosynthesis of Hydrocarbon Fuels. *Angewandte Chemie International Edition* **2018**, *57* (32), 10221–10225.

(22) König, M.; Vaes, J.; Klemm, E.; Pant, D. Solvents and Supporting Electrolytes in the Electrocatalytic Reduction of CO_2. *iScience* **2019**, *19*, 135–160.

(23) Figueiredo, M. C.; Ledezma-Yanez, I.; Koper, M. T. M. In Situ Spectroscopic Study of CO_2 Electroreduction at Copper Electrodes in Acetonitrile. *ACS Catal* **2016**, *6* (4), 2382–2392.

(24) Rashid, N.; Bhat, M. A.; Ingole, P. P. Dendritic Copper Microstructured Electrodeposits for Efficient and Selective Electrochemical Reduction of Carbon Dioxide into C_1 and C_2 Hydrocarbons. *Journal of CO2 Utilization* **2020**, *38*, 385–397.

(25) Bordwell, F. G. Equilibrium Acidities in Dimethyl Sulfoxide Solution. *Acc Chem Res* **1988**, *21* (12), 456–463.

(26) Wang, L.; Nitopi, S. A.; Bertheussen, E.; Orazov, M.; Morales-Guio, C. G.; Liu, X.; Higgins, D. C.; Chan, K.; Nørskov, J. K.; Hahn, C.; Jaramillo, T. F. Electrochemical Carbon Monoxide Reduction on Polycrystalline Copper: Effects of Potential, Pressure, and pH on Selectivity toward Multicarbon and Oxygenated Products. *ACS Catal* **2018**, *8* (8), 7445–7454.

(27) Izutsu, K. *Electrochemistry in Nonaqueous Solutions*; Wiley, 2009.

(28) Bordwell, F. G.; McCallum, R. J.; Olmstead, W. N. Acidities and Hydrogen Bonding of Phenols in Dimethyl Sulfoxide. *J Org Chem* **1984**, *49* (8), 1424–1427.

(29) Roberts, J. A. S.; Bullock, R. M. Direct Determination of Equilibrium Potentials for Hydrogen Oxidation/Production by Open Circuit Potential Measurements in Acetonitrile. *Inorg Chem* **2013**, *52* (7), 3823–3835.

(30) Yoon, Y.; Yan, B.; Surendranath, Y. Suppressing Ion Transfer Enables Versatile Measurements of Electrochemical Surface Area for Intrinsic Activity Comparisons. *J Am Chem Soc* **2018**, *140* (7), 2397–2400.

(31) Altwicker, E. R. The Chemistry of Stable Phenoxy Radicals. *Chem Rev* **1967**, *67* (5), 475–531.

(32) Hui, Y.; Webster, R. D. Absorption of Water into Organic Solvents Used for Electrochemistry under Conventional Operating Conditions. *Anal Chem* **2011**, *83* (3), 976–981.

(33) Hui, Y.; Chng, E. L. K.; Chua, L. P.-L.; Liu, W. Z.; Webster, R. D. Voltammetric Method for Determining the Trace Moisture Content of Organic Solvents Based on Hydrogen-Bonding Interactions with Quinones. *Anal Chem* **2010**, *82* (5), 1928–1934.

(34) Pegis, M. L.; Roberts, J. A. S.; Wasylenko, D. J.; Mader, E. A.; Appel, A. M.; Mayer, J. M. Standard Reduction Potentials for Oxygen and Carbon Dioxide Couples in Acetonitrile and N,N-Dimethylformamide. *Inorg Chem* **2015**, *54* (24), 11883–11888.

(35) Bordwell, F. G.; McCallum, R. J.; Olmstead, W. N. Acidities and Hydrogen Bonding of Phenols in Dimethyl Sulfoxide. *The Journal of Organic Chemistry* **1984**, *49* (8), 1424–1427.

The preceding work in this chapter was supported by ExxonMobil through its membership in the MIT Energy Initiative.

Acknowledgements

Writing an acknowledgement section of a thesis is like writing the "The More You Know" for a Surendranath Lab group meeting: as tradition, mine will be a lot longer than I intended.

This thesis, and the person writing this thesis, would not be here without the contributions of many individuals over the years. While I was surrounded by many fantastic groups of people, my memories of MIT will be defined by the personalized interactions that I've had with each and every person over my career. I'm thankful for what each person said, did, or communicated to me that helped build a personal philosophy on how to go about doing research and, generally speaking, life (thus far). I am herein honored to give you my written account of the actors that made all of this possible, and how they made the journey just as good as the end result.

The Yogi Lab

Prof. Yogesh "Yogi" Surendranath

Before coming to MIT, literally everybody and their maternal grandmothers raved about Yogi. "Yogi's *incredible*" or "Yogi's research is truly one of a kind" or "Yogi is a top choice for a Ph.D. advisor". It was nearly impossible to find a single negative review of Yogi and the lab, so I have to admit that I held some skepticism when I first met with Yogi at visiting weekend to discuss his research vision, the group culture, and whether he performed ritual sacrifices to maintain his reputation.

After five years of working in his lab, I found both no evidence of ritual sacrifices and a deeply supportive advisor who was just as important to my journey as the people within the group itself. Thank you, Yogi, for giving me the chance to work and learn under your supervision. It was always uniquely refreshing to hear your perspective not just on my work and research direction, but also about your opinions on the philosophy of doing science, and about what it means to be a scientist who is constantly evolving and asking the big questions. Some of the most important lessons of graduate school I learned from the introspective, integrated wisdom you accumulated throughout your own research career. Indeed, there were plenty of small tips, tricks, and secret ingredients baked into the recipe of what made your mentorship unique. But out of everything, I appreciated your willingness and passion for being present at the most challenging intersections of the journey, as well as your continued faith in the idea that somehow, with time and effort, I would make it all work out.

The Postdoctoral Researchers

I have had the pleasure of meeting a handful of postdoctoral scholars throughout the years:

Dr. (now Prof.) Marcel Schreier. Marcel was my mentor when I first joined the lab, and I am deeply grateful for the time and effort he spent teaching me how to run experiments, interpret data, and being one of my very first interactions in the group. Marcel, thank you for your dedication towards my personal growth. I will remember the late-night conversations ranging from CO_2 electroreduction catalysis, scientific philosophies, the potential financial investment benefits of owning art, and your efforts to continue a career in academia. I am grateful to have been a part of a critical juncture of your own research career and am happy to have seen how your life has flourished since moving to Wisconsin.

Dr. Ryan Bisbey. Ryan: you're an angel. You were always there when the lab needed it, whether it was taking initiative to plan events, fix our lab's infrastructure, or to be a mentor to everybody including myself. We shared a lot of common philosophies about what it means to be a lab citizen and to continually give back to your community, regardless of whether those actions were seen. You were (and still are) an

incredible role model, and I only wish I could be nearly as cool as you. Thanks for your dedication, and it was great playing video games with you too.

Dr. Patrick Smith. You always had an opinion on everything, whether it was hot sauce, spectroscopic measurements, or your contrasting opinions on your experience living in Boston or California. It was always as fun time hearing your takes on things, and I am still in incredible debt for the insane idea to cryotrap ethylene with liquid Ar. Thank you for being someone I could reach out to whenever I wanted to hear somebody talk, also, I miss your dog.

Dr. Daniel Bregante. While your time in lab was so incredibly short, and while I wish we could have done awesome CO_2 reduction work together, the fact that you hung around Boston after and continued to keep in touch was awesome. Thank you for being inspirationally good at everything you do, for being an attentive listener when I was at my lowest (which was a lot), and your direct perspective on how to build a professional career after grad school. Your pivot from academia into industry was built of a sense of "just do it" energy that I hope to live out myself, also, I miss your dog too.

Dr. Michael Pegis. Mike, you had a unique depth of experience studying PCET and non-aqueous electrochemistry that is very rare to find anywhere else. In retrospect, and in knowing that those topic areas would become the literal bedrock of my thesis, you taught me a lot of intellectual and technical details relevant to my projects and my overall research pursuits. Thank you for taking the time to mentor me, answer my questions, and for being a part of this research journey.

Dr. Ethan Sauve. There's something unique about being told to measure the CO_2 uptake rate and capacity of rocks, and if there was anybody to be paired doing it with, I'm very happy that it was with you. I always appreciated your willingness to chat about literally whatever, and for the good times and memories we shared outside the walls of building 18. Thank you for being a positive vibration within the group, for understanding the energy of wanting to work as a manager at Best Buy, and for always being down to see an anime movie even if nobody else in the lab wanted to.

Dr. Hai-Xu "HX" Wang. HX, you are the hardest rocker in our lab. Thank you for all the insightful scientific conversations, particularly in the phosphorous reduction side project we shared, and your continued expertise at the intersection of synthetic and fundamental electrochemistry. You also had one of the best selections of group snacks and a powerful (perhaps too powerful) volleyball serve. I hope that one day we will get to sing together again at a food opera.

Dr. Max Huelsey. The Schmidt fellow himself, Maximillian, the namesake of January 21st. Thank you for being such a good listener. Every time I had a concern about science, or job searching, or whatever other existential moments I had towards the end of my Ph.D., you always had a level mindset with which to bounce ideas and perspectives. You're super cool. Please don't let anybody take that away from you.

Dr. Anton Ashuiev. If we had more time, maybe we could have made the methanol work. I have faith that you'll come to some interesting conclusions in that project space one way or another, and please, do treat the two-compartment cell I gave you well. It was my lucky one. Best wishes with everything.

Dr. Neil Razdan. Neil, your expertise as a chemical engineer and your candid humor are both worthy of great envy. Though our time together was short, you helped me out in all the small ways that mattered, from helping me make connections for my next job, to helping me get an intuitive understanding of reference energies and activities. Best of luck with your academic career moving forward as you finish your time in the lab.

Dr. Rui Zeng. Thanks for being there on Sundays. With you, I never had to worry about working alone 👍 .

The Senior Graduate Students

I've also had the pleasure of meeting many of the older graduate students, during the pre-tenure era, who were always there to let me know of the things that were to come:

Soyoung Kim (i.e. Soy Kim, but only to me). Soyoung, I still have the "I ❤️ H_2SO_4" sticker you gave me when I moved into my desk space. It remains a fixture of the time that we spent together, literally back-to-back when you were always present to give me helpful advice about science and about life. Thank you for inviting me to all the free food events you knew about, for discussing your faith, and for sharing your perspectives as the older student. I'll never forget how surprisingly good you were at the floss.

Corey Kaminsky. Corey, it is always fun to meet another middle child. As a statistically-less-probable demographic, getting to meet someone who understands that experience is a real treat, and I've particularly appreciated your lessons on how to constantly advocate for oneself. I've appreciated all the real conversations we've had about the graduate school experience, as well as your career advice when you were long gone. Perhaps, in a different universe, we could have had many more group meals at Dumpling House, but alas, I'm very thankful for the ones that we did. Thanks so much for being a positive force in the group.

Jaeyune Ryu. Jae, you're good. Like exceedingly good. Thank you for being good at what you do, to me, to other people, and to our community. Your mentorship and willingness to discuss the "big picture" experience of doing science and research was and still is greatly missed. I'm glad to hear that everything has worked out in your academic career thus far, and that the world has only seen the beginning of what you have to offer. (In another reality, I would come to South Korea to postdoc for you.)

Jonathan "Jo" Melville. Jo, you were always good at talking about emotions, which is refreshing given the cold, hard, dry experience of graduate school (or perhaps that's the Cambridge weather). I'm glad that I had the chance to not just to hear your unique perspectives on many subject matters, but also for the personal moments where you asked me how I was doing and to check in. You taught me about how to be a good listener and conversationalist, and I'm grateful to have learned some of it from you.

Travis Marshall-Roth. Though it was a brief moment in graduate school when I was chilling in the 2nd floor closet, I always appreciated how we used our time together to speak our minds. Whether it was to find some sense of mutual validation in our philosophies of science, our common personalities, or for your general wisdom as an older student, I've enjoyed how your life experiences gave rise to your unique perspectives. Thank you for expressing care, and I appreciate your willingness to share the same space.

William Howland. Will, you had the best jokes. The best one I remember was during that one group retreat at Endicott House where, in realizing that all we do is substrate protonation, that "HER is the protonation of the vacuum". It doesn't hit the same having just typed that out, but trust me, I found that really funny. Also, I liked how we both contributed to Marcel's professional website being commissioned anime art of the Pikachu evolutionary line. Thanks for all the laughs, and for ordering all the common lab supplies that came to my mind.

Onyu Jung. My other CDR half. As much as you always gave me credit for building up the non-aqueous space, you were right there with me at the start when I had questions to ask, scientific perspective to seek, and to give all the personal validation that everyone just needs a bit of. Onyu: thank you, so much, for generously sharing your time with me. It was a great pleasure working with you in the same project space, being with you when the times got rough, and for the time we spent after you left. I would like, particularly, to thank you for filling up the M&M jar at your desk pre-pandemic.

Andrew Licini. Andrew, there are very people I've met who have grown as much as you did during graduate school. You went through so many struggles, slowly overcame them, and found your way through the hardest parts. The journey's not over, but to be there as a part of that journey is truly an honor. Thank you for being such a welcoming presence in the lab, for always acting with good intentions, and for all the conversations about both the serious and nerdy stuff. The time I took you out to have phở for the first time remains a highlight of our memories together.

Thejas Wesley. Thejas, with you, it has always been real. While it took me a while to be able to discriminate when you were being serious or trying to crack a joke (of which you did a *really* good job hiding), I've admired how seamlessly you were able to pivot between the two modes. Your acumen for science is uniquely grounded in your passion for the activities you choose to commit yourself to. Thanks for all the times you asked me how I was doing, by the way. They were simple gestures but meant a lot.

The Contemporaries ("the Brillouin zone")

This section is dedicated to the three other compatriots who entered the Yogi lab in the same cohort:

Wei Lun "James" Toh. James, you'll be remembered by the many hats you wore. From the lover of musicals to the soymilk enthusiast, to the rent payer, to the undergrad mentor, to the ion transport master, to the PS5 enthusiast, to the one of many sayings: the list goes on and on. When I think of graduate school as being an opportunity to collaborate, I think back to all the early mornings and (sometimes late nights) spent talking about driving our shared projects, whether it be in the BPM space or with the rocks. And when those conversations translated into spontaneously getting food? Even better. Everything else is horses for courses. Thanks for being great to work with.

Bryan Tang. Big celebrations, sumptuous backyard BBQs, wild group retreats, and everything else considered, I think back specifically to the moments we shared walking together. Whether it was home from lab back to the dorms, or eventually to East Cambridge, or to get clothes in Back Bay: the conversations I had with you on foot taught me about how you think about happiness, and by extension, encouraged me to think about how to think about it for myself. Those conversations had a notable impact on how I ended up making decisions towards the end of graduate school. Your candid attitude and insights are what made you, you. Thanks for that, and I'm glad we got to grow together.

Noah Lewis. I don't have all of it down, but I am sure I know most of the rules of kosher by now. In fact, you always knew the most random trivia, and that's why I look back at all the memories with you as being primarily defined by fun (Vermont group retreat especially). Aside from that, you were my go-to for advice on synthetic expertise, on scheduling subgroup, and for trading advice and perspective when it came time to apply for jobs. Thank you, also, for knowing all the specific young American millennial things that people our age would know; as I learned in graduate school, I subsist on conversations like that ("*Fleens?* You're not *fleens!*").

The Junior Graduate Students

At some point in graduate school, I found myself transforming from a mentee into a mentor, whose side the following graduate students got to see:

Deiaa Harraz. One of these days, we need to bury the hatchet on this whole intuition-based science thing. But while we had our fair share of differences, we had many more similarities. To good eats around Boston (i.e. Silk Road), to being INFJs, to sharing the little things that annoyed us: thanks for always being available

to chat about everything to nothing at all. I always loved hearing your philosophies, and that you were generous with your time. It was never boring to talk with you, and I wish you only the best moving forward.

Sophia Weng. You're incredibly talented. You can do synthesis, electrochemistry, and spectroscopy (and I wish my resume looked even half as good). But beyond all that, I want to take this acknowledgement to thank you for all the work you did to maintain our group functions, whether it is volunteering the effort to get things fixed, organizing things like mentorship, as well as your general service to the department. Above all the scientific conversations we had in the CDR space, I always appreciated our shared vision of what we wanted our careers to go. It's always nice to know that there are others out there who want similar things.

Kunal Lodaya. Kunal, thank you for being a great volleyball captain. I'm mentioning this specifically because it's emblematic of your enthusiasm for building group culture, fostering a positive dynamic, and your worthwhile efforts to be a caring member of the lab. I'm glad that I was able to be your department mentor, though honestly, it became clear very quickly that you were able to find your stride in our group and its work. You quickly rose into your own being. Thanks for every ride you offered to give, gathering you hosted, and moment spent encouraging each other.

Vennela Mannava & Karl Westendorff. I have to credit you both together because you both shared this quality of laughing at things I said that I honestly did not think were that funny (but endearing to think so nonetheless). There are moments in life when you need to say ridiculous things, and the conversations I've had with both of you encapsulate some of my best interactions in lab. At the same time, you both gave me a lot of opportunities to pass down my scientific knowledge and wisdom. You both are going to do great. Vennela, the Friendly's car will go down as a momentous highlight of all group retreats. And to Karl, remember: it's always on god.

India Cox. In some ways, it really is a shame that grad school had to end. We would have tackled the non-aqueous space as a duo, opened up really cool new projects, developed interesting insights, shrugged off the haters, and entertained each other in the whole process. Unfortunately, life called, and I had to leave, but I really do appreciate all the time and effort you put into absorbing my expertise in the short time we spent together. Every mentor hopes that their mentees will have a better experience than they did. And even if you don't, you'll figure it out. You've got a good head on your shoulders and I'm looking forward to the great science you'll do.

Tolik Borisov. Okay so after writing the previous entry, I realized that I'm going to miss some of the most pivotal moments of the first years' experiences in graduate school, so I'm going to dedicate the rest of these comments to bestow all of you with my best blessings. So, Tolik: you're going to rock it, sock it, and knock (NO_x?) it. Your earnest and disciplined personality will be a core element of your success, and while graduate school naturally will be a bumpy road, I've appreciated in our few conversations how naturally optimistic and excited you are for the things that will come. You'll be able to handle it in style.

Joel Gardner. I'm happy to know that you're going to be continuing the tradition of teaching Adobe Illustrator. While your graphic from the bootcamp was…interesting, to say the least, I have a prediction that the creative side of your personality will also be representative of the creativity of your own science. While jokes are good when they are delivered with good timing, so is encouragement, which is a timing you're well suited for. Keep on making it happen.

Hye Won Chung. Your hard work speaks for itself.

The Undergraduate Students

Given that I taught high school for a bit before attending graduate school, I have a special place in my soul for talking to ~~kids~~ undergraduates, of which there are a few from our lab I'd like to highlight:

Sasha Alabugin. Not that there is a prototypical definition of an MIT undergraduate, but Sasha, your nocturnal existence in lab, deep intimate knowledge of science, love of Soylent, continued references to IRC chatboards, obscure memes, and zoomer lingo lives on in my memory. Thanks for being fun to take Karthish's class with, for connecting after you graduated, and for giving me your most inspiring quotes.

Hieu Dinh. So Hieu was my (and then eventually shared with James') undergrad. After teaching him 5.03 in his freshman year, he decided only *after* 3 years to join the Surendranath Lab under my tutelage, realizing the horrible mistake he made of joining any other lab.

Okay but jokes aside (and the fact that the reason for this was because the pandemic happened in the middle of his college experience): Hieu, I want to seriously commend you for all the hard work you put in lab. Yes, it's true that your success came out of your emboldened desire to go to graduate school. But our lab and the whole electrochemistry community benefitted from the knowledge you developed in the BPM space in conjunction with James. As a mentor, I honestly didn't have too much to teach you, but I'm very glad to have seen you run far with the things I did. You have your own evolving vision of success and am looking forward to seeing you develop your own brand of work at Harvard.

Andy Fong. Your straightforward and honest nature is your biggest trait. While the end of graduate school can make one tired and worn at times, it was always refreshing to hear the perspective of someone who simply wants to pursue the things that are interesting to them without worrying too much about the big things. I know others will disagree, but I also want to take this paragraph to say that I liked your choice of music to play in the lab. It was great. Best of luck with the rest of your time at MIT.

MIT Chemistry & Greater Community

In addition to all the folks from the lab, I want to take the moment to run through acknowledgements of some of the community of MIT Chemistry, MIT the school, and affiliates:

Professors: First, I'd like to thank my thesis committee: **Prof. Alison Wendlandt** and **Prof. Daniel Suess**. Alison: thank you for being my chair, for having great conversations about life as a researcher, and for providing constructive and encouraging feedback after both of my orals processes. For Dan: in addition to being my other member, thank you for being a wonderful 5.03 lecturer and making it a great class to TA for. I would also like to specifically highlight **Prof. Alex Radosevich** here which seems unwarranted, given that I've only had one interaction with him in my time at MIT outside of orals. However, the following story needs to be told:

> *MIT chemistry's visiting weekend was awkward for me because I didn't get accepted into any other schools, and I didn't know how to respond when other prospective students asked me where else I visited since most students got in everywhere they applied. It got really awkward when Alex, who I had no business talking to, asked me the same thing at the standing reception at the MIT Museum. At that point I was feeling a little left out about it and said:*
>
> *"Oh, uh, unfortunately I didn't get accepted anywhere else, so this is my only visiting weekend..."*
>
> *To which he responded: "Well, it sounds like we made the right choice."*
>
> *That was easily the coolest thing anybody had ever said to me ever.*

As is customary, I would like the entire and rest of the MIT inorganic faculty (**Prof. Mircea Dinca**, **Prof. Christopher "Kit" Cummins**) for making sure my orals experience wasn't *too* easy, and for teaching the classes that defined much of the first year of graduate school. That also includes **Prof. Karthish Manthiram** for teaching a fantastic electrochemistry course in the chemical engineering department and for his support in my general career.

MIT Administration and Staff: I'd like to thank **John Grimes** and **Bruce Adams** for both of their expertise and assistance down in the NMR room; **Dowey Tran**, **Jennifer Weisman**, and the rest of the chemistry education office for coordinating seminar, class, and graduation logistics (also Dowey for buying me bánh mì one time 😊); **Sibora Cjapi** and **Christopher Krisofske** for helping me when Buy2Pay and stray purchase orders were giving me a headache; **Joanne Baldini** for being an awesome lab admin; and both **John Dolhun** and **Amanda Trainor** for their guidance and support for running the lab TA'ing experience.

Ed "The Glassblower" Mitchell: A scientific glassblower is a very special human being, as most labs would crumble if they didn't exist. Though you would think this endows them with tyrannical amounts of leverage, Ed was one of the most generous, wisest professionals I've met during my time at MIT. His acumen is built from years of experience working and networking with the academics in the greater Boston area, as well as his own work in industry prior. Ed, I'm glad that we are able to call each other friends. From making some of the most innovative glass cells (which I always ordered in pairs, you know why), to getting pizza, to sharing your opinions of life: I learned so much from you.

Cohort Friends: In addition to the Brillouin zone, I'd like to highlight other members of the 2018 chemistry cohort who I enjoyed the company of throughout the years: **Trever Bostelaar** for our dynamic as the 5.03 teaching duo, **Ruomeng Wan** as my kindest cheerleader, **Griffen Desroches**, **Alex Seim**, and **Xin Gu** as people I'd always see when there was pizza around, and my two other department mentees, **Bowen Tan** and **Gear Khuichad**. From that, I'd like to thank **Jet Lem** and **Jinyi Yang** for hosting some great dinners, and Jinyi in particular for being my Teamfight Tactics duo, to whom I introduced the game to after beating me in all the board games at the department holiday party (you are very, very good at games).

Other Undergrads: Though not members of the Yogi lab, there are a couple of other MIT undergraduates who I basically consider my mentees in all other aspects. That would include **Michelle Lee** and **Junyu Yang**, both of whom I kept in touch with after helping them apply to graduate school, and always had great, deep, meaningful conversations. There's also a unique shoutout I'd like to give to **Rachel Cheng** and **Diane Li**. When I taught very (very) briefly at Princeton High School for a semester after college, I never in a million years would have expected for two of my former students to come to MIT at the same time as me, much less desire to keep in touch. But I'm so incredibly grateful for your willingness and enthusiasm to hang out, share what was going on in your minds, graduate, and land fantastic jobs, all within the span of my time as a Ph.D. student. I said this to both of you already, but I wish I was half as cool or genuine as either of you were when I was your age. Please keep slaying.

Other People: To round off this miscellaneous category, I'd like to thank **Dr. Ruperto "Rain" Mariano**, who I enjoyed having conversations about electrochemistry, and for sharing your enthusiasm for taking your research skills into building real technologies. I'd also like to thank **Sophie Liu**, the chief supervisor for the Exxon Mobil related projects I worked on, for providing timely support and communication, and generally for being fun to stay in contact with through my MIT career.

<u>Princeton Chemistry Community</u>

While MIT will remain a fixture of my research career, it was in college at Princeton University where I met the people who inspired me to embark on this path.

Princeton University: The whole CO_2 reduction thing really started when I worked in the lab of **Prof. Andrew B. Bocarsly**. While I deeply enjoyed the research, the community, and the camaraderie in his lab, I had seen research more like working a job rather than as a career passion. It wasn't until Prof. Bocarsly sat me down in his office and told me that I should seriously consider graduate school, that I actually seriously thought about going to graduate school. (Well, the conversation wasn't nearly as simple as I'm putting it, and there were certainly some debates…) But it highlighted how much of an impact a little encouragement from a great mentor can have, and eventually led me to an experience at MIT that I am incredibly thankful for. The fact that I ended up in the Surendranath Lab specifically also can be directly attributed to the endorsement of the wonderful graduate students and staff who I worked with in the Bocarsly Lab, which includes **Dr. Sonja Francis** (who also helped supervise my senior thesis), **James "Jim" White**, **James Pander**, **James Park** (and yes, that's *three* Jameses), **Aubrey Paris**, and **Hsinya Kuo**. Speaking of other forms of departmental support, I'd like to thank **Prof. Stanislav "Stas" Shvartsman**, **Prof. Martin Semmelhack**, and **Prof. Erik Sorensen** for all writing recommendation letters in one form or another. And while we're here, **Dr. Robert "RPL" L'esperance** and **Kirsten Arentzen** for always being happy to entertain my conversations about the future while I was still an undergraduate.

Princeton High School. Teaching high school full time, as a student teacher, was serendipitously one of the most important experiences that prepared me for graduate school. It was when I really started to understand what science is at its heart. And it's why I'd like to acknowledge some key folks for making that a wonderful experience here in my thesis. First, I'd like to thank the **Princeton Teacher Prep** program for teaching the relevant seminars and for organizing the curriculum and experience. And second, I'd like to acknowledge my host teacher, **Ms. Janine Giammanco**, who besides being a generally fantastic human being, always supported my life journey regardless of wherever I went or felt like was the right place to go. Janine, thanks for the time we spent meeting up every college reunion and for sharing your life experiences. I'm glad that the humor we shared while in the classroom continued in our lives thereafter.

Friendships at Large

Bostonians: For this category, I'd like to thank **Daniel Yang**, **Conor O'Brien**, **Teresa Tang**, **Crystal Qian**, **Laura Smitherman**, **Jonathan Lin**, **Uri Tayvah**, and James Pander for the time we spent hanging out getting meals, coffee, beer, or whatever platform it was that allowed us to chat and catch up on life since we all left college. In addition, I'd like to thank my former college and Boston roommate **Peter Du** with whom we share a very specific humor niche. And speaking of roommates: **Donovan Neo**, the fourth roommate of our tenure in East Cambridge, for all the candid conversations at our place.

Virtual Groups: While I've made a lot of new friendships in graduate school, I'm deeply grateful for the opportunities I had to continue video gaming with my college friends and acquaintances from the Princeton eSports club. Although there are many individuals and groups in this network, I want to shoutout the ones who made the late nights and hours spent outside of lab memorable (especially during the pandemic): the Monster Hunters of "Free Deeps" (**Lucy Jing**, **Joseph Crapse**), the couch co-op crew of the "Sun Haven Addicts" (**Alec Leng**, **Betty Liu**), the old guard of "Dank of the Strim" (**Tony Leng**, old **Kevin Lin**, **Daisuke Katsumata**, **Jason McSheene**, all the Dota people (**Himawan Winarto**, **Matthew Li**, etc.), and the Teamfight Tactics prodigy (young **Kevin Lin**) for helping me get engrossed in the only game I'm okay at. Other shoutouts in this category include **Heling Zhao**, **Thomas Gilgenast**, **Michael Ye**, and of course, the rest of the community I saw in person or virtually throughout the years. I have had a lot of fun hanging out with you all, and here's to many more years to come.

Amherst, MA: And finally, a few more people from my hometown. The first being **family**, for reminding me of the importance of Vietnamese food. The second being my high school chemistry teacher, **Dr. Sharon Palmer**, for whom I am indebted to the introduction of chemistry in high school (and also more subtly, although I didn't realize it at the time, what it means to think like a "Dr."). And the third being my family

friend and life mentor **Dr. Nhiem "Lucy" Nguyen** for helping me realize my full self, and whose own journey through a life of scholarship as a was an inspiration for my own.

Superlatives

- Best food spot: Pho Pasteur
- Best vending machine: the one underneath Stata
- Best lucky break of my Ph.D.: when the 100th vended snack from the machine was free
- Best electrochemical technique: chronopotentiometry
- Best potentiostat: Gamry Instruments Ref 600
- Best place to get bananas: the Banana Lounge
- Best volleyball team: Never Surender
- Best studying spot: Hayden Library
- Best inorganic seminar: Harry Gray's Alan Davison Lecture
- Best place of take advantage of free seminar dinner: Sumiao Hunan Kitchen
- Best group snack: Cape Cod Potato Chips
- Best email that I'm not going to miss: Security alert from surendranathlab(at)******(dot)***
- Best thing to have wished didn't happen during the Ph.D.: global pandemic
- Best class to have TA'd: 5.03 (don't forget the torus!)
- Best "The More You Know" that I've given:
  1st: *Why are most American Nail Manicurists Vietnamese?*
  2nd: *The Real and Unreal of Professional Wrestling*
  3rd: *Not all Pokémon Are Created Equal (and the Implications for Competitive Pokémon Battles)*